Characterization of Paper Heterogeneity

by

John M Considine

A dissertation submitted in partial fulfillment of
the requirements for the degree of

Doctor of Philosophy
(Materials Science Program)

at the

UNIVERSITY OF WISCONSIN - MADISON
2013

Date of final oral examination: 08/19/13

The dissertation is approved by the following members of the Final Oral Committee:

Kevin Turner, Associate Professor, Mechanical Engineering
Wendy Crone, Professor, Engineering Physics
Roderic Lakes, Professor, Engineering Physics
Robert Rowlands, Professor, Mechanical Engineering
Fabrice Pierron, Professor, Solid Mechanics, University of Southampton
David Vahey, Retired Scientist, Forest Products Laboratory

"The single biggest problem in communication is the illusion that it has taken place."

George Bernard Shaw 1856-1950

UNIVERSITY OF WISCONSIN - MADISON

Abstract

Materials Science Program

Doctor of Philosophy

by John M Considine

Paper and paperboard are the most widely-used green materials in the world because they are renewable, recyclable, reusable, and compostable. Continued and expanded use of these materials and their potential use in new products requires a comprehensive understanding of the variability of their mechanical properties.

This work develops new methods to characterize the mechanical properties of heterogeneous materials through a combination of techniques in experimental mechanics, materials science and numerical analysis. Current methods to analyze heterogeneous materials focus on crystalline materials or polymer-crystalline composites, where material boundaries are usually distinct. This work creates a methodology to analyze small, continuously-varying stiffness gradients in 100% polymer systems and is especially relevant to paper materials where factors influencing heterogeneity include local mass, fiber orientation, individual pulp fiber properties, local density, and drying restraint.

A unique approach was used to understand the effect of heterogeneity on paper tensile strength. Additional variation was intentionally introduced, in the form of different size holes, and their effect on strength was measured. By modifying two strength criteria, an estimate of strength in the absence of heterogeneity was determined.

In order to characterize stiffness heterogeneity, a novel load fixture was developed to excite full-field normal and shear strains for anisotropic stiffness determination. Surface strains were measured with digital image correlation and were analyzed with the VFM (Virtual Fields Method). This approach led to VFM-identified stiffnesses that were similar to values determined by conventional tests.

The load fixture and VFM analyses were used to measure local stiffness and local stiffness variation on heterogeneous anisotropic materials. The approach was validated on simulated heterogeneous materials and was applied experimentally to three different paperboards. The analyses were used to create upper and lower stiffness bounds; the scale of the bounds were related to the coefficient of variations of stiffness and grammage variations.

This work contributes to understanding of heterogeneous material behavior by characterizing strength loss due to variability and determining stiffness bounds in materials in which heterogeneity varies gradually and is complicated by several, interrelated physical properties.

Acknowledgements

I doubt many advisors have ever taken the burden that Professor Turner did when accepting me as a graduate student. He has faithfully supported this work even when avenues of success weren't apparent. He put up with my fumbling attempts and false starts. He was patient beyond forbearance. I selfishly hope that our collaboration will continue.

Dr. Alan Rudie, my project leader at Forest Products Laboratory, deserves special thanks for agreeing to fund my thesis work. Especially noteworthy is that he is an inorganic chemist, which means that he will never use this work in his research. And yet he graciously funded this work without hesitation.

Sage advice from farmers: when you are about to embark on a new farming enterprise, whether it be a new crop or species of livestock, find a farmer you admire who is successful in the same enterprise and follow their example and advice. Unfortunately I didn't follow this advice when attempting to use inverse methods. Fortunately, Professor Pierron took me to lunch during a Society for Experimental Mechanics meeting in 2008 to explain that my methodology would not work. Over the course of the next hour, or so, he suggested an experimental plan which formed the basis for Chapters 3-5. When I asked him to serve on my committee he quickly accepted and has been ever faithful in responding to emails and actively participating in the ongoing work of the project. I can't express how grateful I am that I was, for once, able to keep my mouth shut and ears open when Professor Pierron developed a strategy during that fateful lunch. Beyond that, Professor Pierron diligently guided me through the seemingly treacherous waters whose borders were full-field measurement and parameter identification. He patiently pointed out errors in thought and word. The remaining errors are mine alone.

Dr. Vahey has an office that is lamentably close to mine, in fact right next to mine. As co-workers on many projects and a terrific sounding-board, I have wasted more of his time trying to explain problems and successes than anyone else's. When he asks how I'm doing he actually listens and provides feedback. As a kind, gentle and knowledgeable co-worker and thesis committee member Dr Vahey consistently provided daily encouragement which provided a type of fuel for me that I didn't even know existed.

Professor Rowlands and I have shared academic adventures which seemed professionally damaging at the time. I am grateful for his support and assistance during those

times and since. His recommendation to a Forest Products Laboratory scientist, Dennis Gunderson, began a career in paper physics that I enjoy each and every day.

Professor Crone agreed to become my thesis advisor when Professor Turner moved to the University of Pennsylvania. During our initial meeting she reminded me that I was not her oldest graduate student and I had to remind her that I hadn't graduated yet. I believe that my slow research speed was at least sufficient to remain second on the illustrious list. Professor Crone's willingness to serve as advisor without tangible professional benefits is remarkably sacrificial.

I took every course Professor Lovell taught on plates, shells, beams, mechanics of materials and energy methods. In each course he devoted large sections to solutions using energy methods. His strong endorsement of energy-based methodology seemed unusual with the rapid development of numerical modeling and other methods. Now I wish I had taken better notes.

My wife, Laurie, is a phenomenal person. Her singular mistake, in a semi-lucid moment, in agreeing to marry me, at 18 years old, is one that I've never allowed her to correct. This work is as much hers as mine. Her support of my endeavors, however far-fetched and there have been some crazy ones, is still exceptional to me. I suspect that the greatest gift I can give her is to actually finish school.

Our children, Jennifer, Thomas, and Stephen, are constant sources of inspiration to me. Their zest, energy and enthusiasm has encouraged me more than they will ever know. Because I discuss my work infrequently they have become convinced that I am a secret agent whose work is only known at the highest government levels. This thesis will put that idea to rest, finally.

I thank God for this wonderful adventure. What a ride!

Contents

List of Figures

List of Tables

Abbreviations

ASC	**A**verage **S**tress **C**riteria
CCD	**C**harge-**C**oupled **D**evice
CD	**C**ross-machine **D**irecton
COV	**C**efficient **O**f **V**ariation
DIC	**D**igital **I**mage **C**orrelation
EG	**E**quilibrium **G**ap
FEM	**F**inite **E**lement **M**ethod
FFT	**F**ast **F**ourier **T**ransform
FWC	**F**inite **W**idth **C**orrection factor
GV	**G**ray **V**alue
LED	**L**ight **E**mitting **D**iode
MD	**M**achine **D**irecton
MRI	**M**agnetic **R**esonance **I**maging
NIR	**N**ear **I**nfrared **R**adiation
PSC	**P**oint **S**tress **C**riteria
PSF	**P**oint-**S**pread **F**unction
PVW	**P**rinciple of **V**irtual **W**ork
VFM	**V**irtual **F**ields **M**ethod

Symbols

a_{ij}	Orthotropic compliances, where $i, j = 1, 2, 6$	Pa^{-1}
C^p	Compliance of inclusion, p	Pa^{-1}
$\overline{C}$	Mean compliance	Pa^{-1}
E_{ij}	Modulus where $i, j = 1, 2$	Pa
F_i	Components of external applied force, $\overline{T}$	N
f	Area fraction of all inclusions	
f_p	Area fraction of inclusion p	
$\mathbf{G}$	Noise optimization matrix	m/m
G_{12}	Shear stiffness	Pa
I_1, I_2	Anisotropic stiffness invariants	km^2/s^2
K_T	Stress concentration factor for finite-width specimen	
K_T^∞	Stress concentration factor for infinite width specimen	
L_f	Line over which external forces are applied	
L	Specimen length	m
n	Number of discrete measurements on specimen	
Q_{ij}	Stiffness, where $i, j = 1, 2, 6$	km^2/s^2 or Pa
Q^p	Stiffness of inclusion, p	Pa
$\overline{Q}$	Mean stiffness	Pa
R	Radius of introduced hole	m
Re	Real portion of complex number	
R_{eff}	Inherent Defect Size	m
S	Region of 2-D object	
$\overline{T}$	Vector of external forces applied on L_f	N

t	Specimen thickness	m
$\overline{u}^*$	Vector of virtual in-plane displacements	m
W	Specimen width	m
$\mathbf{V}(\mathbf{Q})$	Variance of $\mathbf{Q}$, stiffness	N^2
α_{ij}^{mn}	Coefficients of polynomial representation of Q_{ij}	
γ	Amplitude of strain noise	m/m
ε_c	Normalized, composite strain	m/m
ε_i	in-plane strain, where $i = 1, 2, 6$, contracted notation	m/m
ε_i^*	virtual strains associated with $\overline{u}^*$	m/m
η_{ij}/Q_{ij}	$\mathrm{COV}(Q_{ij})$	m^3
μ_i	Complex roots of equation, where $i = 1, 2, 3, 4$	
ν_{ij}	Poisson's Ratio, where $i, j = 1, 2, i \neq j$	
σ_i	In-plane stress, where $i = 1, 2, 6$, contracted notation	Pa
σ_H	Tensile stress of specimen with hole	kN/m
σ_M	Mean Unnotched Tensile Strength	kN/m
σ_U	Unnotched Tensile Strength	kN/m
σ_u	Maximum Potential Tensile Strength	kN/m
$\overline{\sigma}_y$	Far-field applied tensile stress	kN/m
ϕ	Angle between 1- and 2-principal material directions	degrees

Chapter 1

Introduction

Paper is ubiquitous. It would be an extremely unusual day if one's eyes did not read printed paper material or hands touch a paper-based product.

This is a good thing, because paper is one of the original green materials. It is made from 100% renewable material, cellulose fiber the most common polymer in the world. It is recyclable; recycling starts in the paper mill where web breaks are repulped and fed back into the feedstock stream. Recycling continues locally where sorting by paper type and color helps determine value to the papermaker. Eventually paper enters the refuse stream, where it is sold to east Asian papermakers and is recycled as packaging for products made there. Finally, when the recycled fiber becomes very short and hornified, the fiber becomes fuel in a steam-generating facility. Paper is reusable; I can't count the number of times I heard 'back of the envelope' calculation during engineering classes. Good books are reread many times over many years. Lastly, paper is compostable; trendy gardeners use paper as a weed barrier that they replace annually.

Because paper and paperboard, i.e. heavy-weight paper, are green materials they are attractive materials for use in many structures. Primary examples include corrugated containers, by far the most common packaging material in the world, wound cores, used to transport other materials such as carpet, plastic, fabric and yarn, and sack paper. Continued and expanded use in these applications and the potential use in new products requires a comprehensive understanding of its mechanical properties and their variability.

Manufacture of this amazing material requires comprehensive, multidisciplinary technologies. From biology, so that the proper trees can be grown and harvested, to chemistry, which is essential in the separation of cellulose fibers and the production of beneficial additives, to engineering, for production and converting processes, papermaking requires the synergy of many different processes.

Modern papermaking is often dated from the development of the Fourdrinier paper machine in 1801. Two hundred years have been sufficient to create a mature industry and paper has become a commodity product. A greenfield, kraft paperboard mill costs more the $1B US; estimates for paper machine down time ranges from $10K-$100K per hour depending on machine and grade of paper produced. We've reached the point that changes in paper production need to be incremental and made by those motivated to create product differentiation.

An example comes from a Scandinavian paper company which produces medium, the paperboard which forms the wavy section in a corrugated structure. They found that by reducing property variability they could reduce grammage[1] by 10% and improve corrugated strength. As fiber costs are the largest costs in papermaking, this created tremendous savings. Naturally, those producing corrugated board were suspicious, but the company tested their material against others and demonstrated superior performance. The company was eventually able to charge a premium for their medium. It's an infrequent occurrence that a producer of a commodity is able to reduce material costs and increase sales and profit margin.

Another example comes from a project I personally administered. A US company needed help to determine cause(s) of failure of corrugated containers used to protect and provide point-of-purchase displays for a product made in east Asia. While I never learned the costs associated with product damage, the cost of repackaging undamaged products that arrived in the US in damaged containers unsuitable for display were $1M annually. The packaging failures were attributed to lack of a stiffness specification and lack of variability specification. The company only specified component, i.e. linerboard and medium, grammage and relied on a 'correlation' between grammage and stiffness. Eventually the company made no changes because the stiffness and variability specifications would increase costs. They did tell me that if losses increased to $1.5M annually they would revisit the specifications.

---

[1] weight/area

So understanding of paper variability is important. Material scientists and engineers may differentiate between variability and heterogeneity, but the terms will be used interchangeably here. Lord Kelvin famously said ”If you cannot measure it, you can not improve it.” To date, evaluation of paper heterogeneity has been largely confined to measurements of local mass variation. While this is an important component of heterogeneity, local fiber orientation and residual stresses created during restraint drying also contribute to heterogeneity of mechanical properties.

The objectives of this work are to characterize paper heterogeneity in terms of tensile strength and anisotropic stiffness. While different aspects of strength variation have been investigated this new approach develops a relationship between potential strength improvement and reduction of variability. Characterization of stiffness variation is accomplished by development of a novel load fixture, use of digital image correlation to measure local deformation and strain in the load fixture, and use of the VFM (Virtual Fields Method) for stiffness identification.

State of the art of the VFM has been recently given in a book by Pierron and Grédiac [1]. Important for this work was their work demonstrating that VFM is a generalized inverse method and that other inverse methods, e.g. finite element model - updating and constitutive gap, are particular formulations of VFM. With the introduction of special, optimized virtual fields, explained here in Chapter 3, VFM has been applied to many materials with different constitutive behaviors under numerous loading geometries. Its use in this work was an obvious choice, some may say the only choice, as the tool for analyzing full-field displacement and strain data. One illustration from this work: in Chapter 4 100 simulations each were performed on three different materials. Each of the 100 simulations took about 10 hours in my desktop computer using VFM; the same work using finite element model - updating would have taken over 500 hours.

Chapter 2 describes a characterization of strength heterogeneity which provides two important parameters. First, an inherent defect size is estimated; second, amount of strength increase with defect size reduction and/or elimination is determined. The characterization differs from other work incorporating defect analysis because the inherent defect is created by the confluence of all factors causing heterogeneity. This chapter stands apart as no additional aspects of strength heterogeneity were examined.

Chapter 3 creates a critical foundation for Chapters 4 and 5. The objective of the work in Chapter 3 was to develop a load fixture and analysis tools to measure anisotropy of thin, web materials like paper and paperboard. The load fixture is unique in that it is capable of producing a complex strain field, while keeping the material unwrinkled and in its linear elastic regime, all of which are necessary for anisotropic stiffness identification. The VFM was used for identification. Stiffnesses determined with this fixture and identification procedure agreed with those determined by ultrasonic and tensile tests. Because heterogeneity could be caused by changes in local anisotropy, it was critical that a full anisotropic stiffness identification could be performed.

Chapter 4 examines local stiffness identification of three simulated materials. VFM was expanded from Chapter 3 to include heterogeneous stiffness identification. Displacement fields were created for simulated materials created using finite element modeling (FEM) and were used to evaluate the VFM analyses. Benefits and use of each VFM analysis are described.

Chapter 5 combines the efforts of Chapters 3 and 4 to characterize the heterogeneous stiffnesses of three paperboards. The characterization provides upper and lower bounds of local stiffness and variation of stiffness. The characterization agreed with observed visual differences between materials; the bounds contained stiffnesses determined with assumption of homogeneity.

Just like papermaking requires a multidisciplinary approach, this work required use of basic tensile tests, the development of a new multiaxial test fixture, use of optical measurements (digital image correlation) and NIR (near infra-red) imaging and use of old concepts (Principle of Virtual Work) modernized for today's needs. If heterogeneity is important for your work, regardless of whether you work with paper or another material, I hope this work will give you new ideas for the difficult task of characterizing the heterogeneity of your material.

Chapter 2

Evaluation of strength-controlling defects in paper by stress concentration analyses[1]

2.1 Introduction

Paper materials are three-dimensional (3D) networks of cellulose fibers. Primary variables that contribute to a well-made paper sheet are pulp fiber properties, grammage (mass/unit area), density, drying restraint, and fiber orientation. However, each of these variables has microscopic spatial gradients that contribute to local and global behaviors. The ability to relate these variables and their gradients to the mechanical behavior of paper may offer opportunities to improve its mechanical performance and therefore increase the use of paper as a structural material.

Deterministic and probabilistic models become unduly complicated when trying to evaluate parameters contributing to the mechanical behavior of cellulosic webs. Examples of these types of models are given in references [3–5].

Figures 2.1 and 2.2 show an example of fiber configuration and alignment within a linerboard sample. It is not feasible to determine from such figures a single critical defect (i.e., a defect that controls web strength). Fibers in these figures have a range of lengths and widths but tend to lie within planes. The 3D nature of paper materials seen

---

[1] This chapter was previously published as [2] with minor format changes.

in the cross-sectional view of Figure 2.2 illustrates how defects may be present within the material but not visible in planar views.

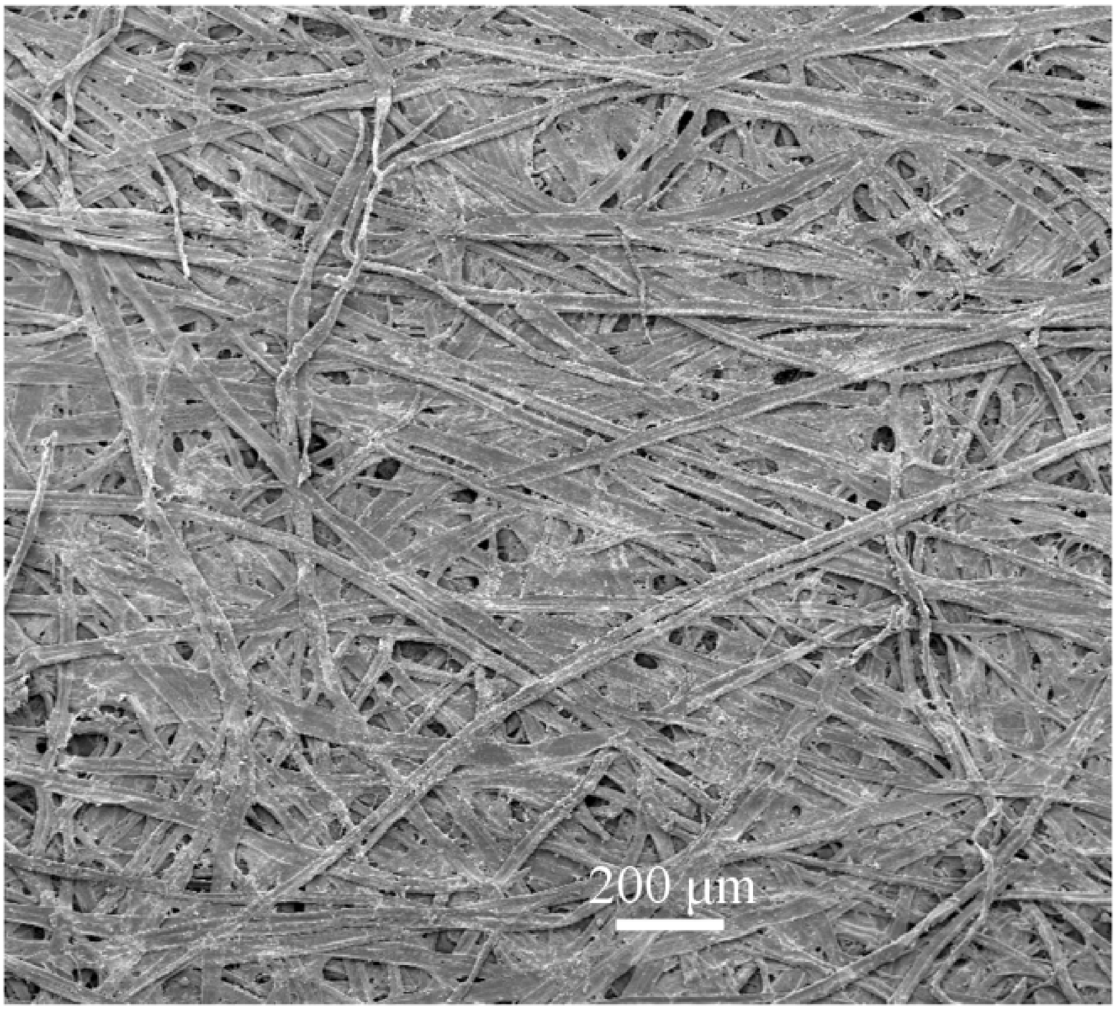

Figure 2.1: SEM image of linerboard surface

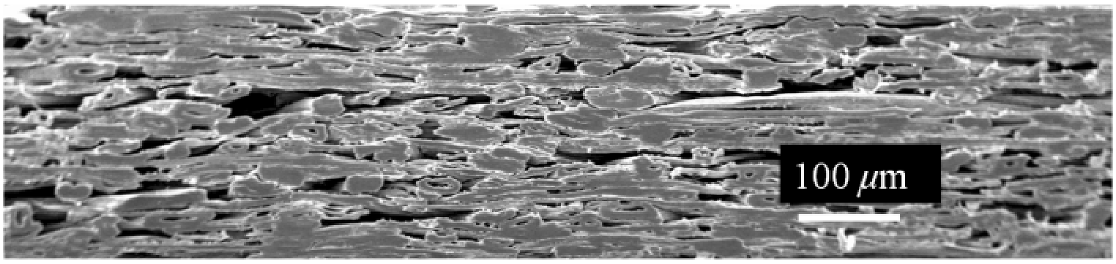

Figure 2.2: SEM image of linerboard cross-section

It is proposed that cellulose webs behave as a conglomeration of defects, interconnected with fibers, which themselves contain defects. Physical identification of size and location of a single strength controlling defect is not possible; however, these materials behave as though their failure is associated with an effective defect of a particular size. This can occur even if no defects of that physical size exist within the structure. Such an entity will be called an ‘inherent defect.’ Moreover, the tensile strength of a material with a size ‘0’ inherent defect will be defined as the ‘maximum potential tensile strength’ and denoted by σ_u.

Researchers have previously tried to relate measured tensile strength, a macroscopic property, to local mass variation, or formation, but no clear picture has emerged. Table 2.1, containing references [6–12] summarizes many of these more significant contributions. Regardless of pulping method, fiber type, or forming method, researchers have found a variety of relationships.

Table 2.1: Summary of previous work relating tensile strength to formation

Reference	Pulp-Fiber	Sheet forming	Finding
Norman [6]	Chemical - hardwood and softwood	Handsheet (isotropic)	Direct relationship between tensile strength loss and large variation of local mass
Moffatt et al. [7]	Mechanical - hardwood	Machine (orthotropic)	Failure zone passes through regions of low grammage
Nazhad et al. [8, 9]	Mechanical - softwood and Chemical - hardwood	Handsheet	Direct relationship between tensile-strength loss and formation
Mohlin [10]	Hardwood and softwood	Machine	No relationship
Nordström [11]	Chemical - softwood	Machine	Depends on grammage and fiber bonding
Wathén and Niskanen [12]	Mechanical and chemical - hardwood	Machine	Weak correlation

Using laboratory handsheets, I’Anson and Sampson [13] found a relationship between fiber dimensions, sheet grammage, and specific tensile strength, such that a maximum specific tensile strength occurred near a grammage of 50 g/m^2, which is less than that of most printing and writing papers. In terms of the present models, fiber dimensions, bonding, and material thickness might coalesce at this grammage level to produce a smaller inherent defect size than at either larger or smaller grammages, thereby increasing strength. The models are comparable to the use of the critical flaw size in statistical fracture mechanics to describe the transition between a disorder-dominated size-dependent material and one that can be described by linear elastic fracture mechanics [14].

Natural defects in poorly formed sheets increase strain disorder [15] and cause separate regions that exhibit elastic and plastic response to occur simultaneously under uniform global stress. A continuum model developed by Korteoja et al. [16] indicates that large strain variations within a sheet reduce tensile strength. Researchers have mapped full-field displacements of tensile-loaded paper and paperboard using digital image correlation (DIC) to characterize variations in strain [17–20]. These mappings showed large strain variations even in papers with apparently good formation, suggesting the existence of stress concentrators. DIC demonstrated large strains near low-grammage regions or holes. In particular, Wong et al. [19] found that local grammage and local tensile strain are inversely proportional to each other. Considine et al. [20] observed compressive strain near low-grammage regions of tensile specimens and attributed those strains to low-modulus inclusions.

Scale of measurement is an important aspect of evaluating behavior of materials composed of cellulose fibers. Hristopulos and Uesaka [21] examined the strength distribution in newsprint and suggested that the critical cluster was on the order of a millimeter, where the critical cluster is defined as the strength-controlling size in weak-link modeling. Other researchers [22] have suggested a larger value based on floc size. Flocs are small regions of higher grammage than the sheet average and are balanced by corresponding low-grammage regions. Floc size, grammage variation, and local fiber orientation each contribute to strength behavior [23].

The present research is similar to that of Rhee et al.[24], who introduced multiple holes in a tensile specimen in order to examine changes in strength caused by defects and stress interaction. Stress distributions associated with individual neighboring holes in a tensile specimen tended to interact with each other and modify the stress concentration factor for any single hole. The present investigation assumes that an introduced defect will interact with physical defects created during manufacturing. Two paper sheets with poor formation in the form of low-modulus inclusions in a high-modulus matrix can have widely differing strengths, suggesting that formation alone is not a strength-determining factor. Recognizing this, the present investigation extends the work of Um and Perkins [18] and Perkins and Um [25], who measured strains in the vicinity of a single hole in a tensile paper strip, calculated associated stresses, and compared their measurements with finite element analysis to show hole boundary stresses greater than the materials tensile strength. Using a quasi-isotropic point stress criterion (PSC), researchers have predicted tensile strengths of paper specimens with a single hole [25, 26].

The present approach is designed to evaluate macroscopic differences in papers due to widespread, mesoscopic defects. The presence of flaws, defined as onetime or occasional defects, is not addressed. Additionally, this approach is based on stress concentration analysis as opposed to stress intensity analysis used in fracture mechanics models. Failure is assumed to be caused by inherent defects that are larger than a critical defect.

2.2 Materials and methods

Defect analyses are investigated here on seven commercially available cellulosic materials whose physical and mechanical properties are listed in Table 2.2. Sheet thickness was measured with a Mitutoyo® (Kawasaki, Japan) 543-396B Digital Indicator equipped with a ball tip of diameter 4 mm. Elastic moduli and Poisson's ratios were obtained ultrasonically with a Nomura Shoji Corporation (Tokyo, Japan) Sonic Sheet Tester (SST). The SST is equipped with one sensor pair, which operates at 25 kHz; measurements were taken at 5° intervals by rotating the sample on a turntable.

Material C is a commercial copy paper containing about 8% ash. Material E is a commercial bond envelope paper and likely contains cotton fibers. Material F is a commercial filter paper manufactured by Whatman® International (Maidstone, Kent, UK), identified as Chromotography Paper, Model 3MM CHR, and was chosen because it is 100% cellulose from cotton linters. Material L1 is a commercial linerboard whose fiber content likely contains both virgin and recycled fibers. Material L2, made on a different machine than L1, is an unbleached, kraft single-ply linerboard, and like L1, a material commonly used in structural paperboard products such as corrugated containers. Materials S1 and S2 are cylinder boards made on the same cylinder machine but with a proprietary processing change between materials.

The material properties in Table 2.2 represent a broad spectrum of paper and paperboards. The density range indicated is fairly typical. Recognizing that the density of native cellulose is approximately 1500 kg/m^3 indicates these papers have a large amount of void space. The orthotropy ratio, E_{11}/E_{22}, may be as high as 5:1 for specially manufactured paperboards, but low ratios, about 2:1, are typical for structural paperboards. All mechanical properties were measured with an OPUS 3-D ultrasonic system (Sonisys, Atlanta, GA, USA).

Table 2.2: Physical and mechanical properties of materials examined

Property	C	E	F	L1	L2	S1	S2
Grammage (g/m^2)	76	92	187	268	209	261	258
Thickness (mm)	0.11	0.13	0.31	0.38	0.30	0.40	0.40
Density (kg/m^3)	721	734	603	717	688	648	643
E_{11} (GPa)	7.82	7.38	4.52	7.80	7.75	9.40	8.20
E_{22} (GPa)	2.56	3.40	2.12	3.71	3.73	2.22	2.02
G_{12} (GPa)	1.63	1.85	1.27	2.10	2.15	0.71	0.70
ν_{12}	0.17	0.23	0.18	0.20	0.23	0.18	0.19
E_{11}/E_{22}	3.05	2.20	2.13	2.10	2.08	4.27	4.06

Note: all properties determined at 50% RH
Material references: C, copy; E, envelope; F, filter;
L1, linerboard1; L2, linerboard2;
S1, cylinder board1; and S2, cylinder board2.

2.2.1 Tensile testing

Tensile tests were performed on an Instron® (Norwood, Massachusetts) Model 5865 test machine equipped with line-clamp pneumatic grips. Gage length, which was determined by available material sizes, was 200 mm for materials S1 and S2 and 125 mm for all other materials. Width was 25 mm. The test sequence started with a pre-load to 1N at 12 N/min, followed by displacement at a constant speed of 1.5 mm/min that continued to specimen failure. Load and grip displacement data were collected at 10 Hz. All tests were performed in a controlled environment at 50% relative humidity (RH) and 23°C.

Some samples were susceptible to tensile buckling; curvature would occur across the specimen width. This was avoided and test similarity insured by transversely restraining all specimens with glass plates. This was accomplished by positioning the specimens between two 100 mm long restraining glass plates separated by a gap of twice the sample thickness and placed at the vertical center of the tensile specimen. These plates were held independent of the test machine and were stationary during tensile testing.

2.2.2 Specimen preparation

Figure 2.3 shows the basic specimen geometry. Each specimen contained a single hole prepared with specially designed tool steel machined punches that have an inner cutting taper to prevent densification of the material near the hole boundary. Holes were located with alignment fixtures that consisted of a different specific fixture for each specimen

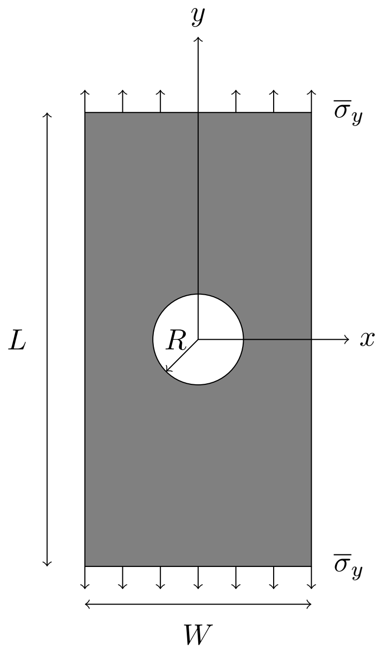

FIGURE 2.3: Schematic of specimen, $L = 125$ or 200 mm, $W = 25$ mm, and $R = 0.25$, 1.25, 1.88, 2.5 or 5.0 mm.

geometry. The alignment fixtures insured hole location along the longitudinal centerline and held the specimen firmly to a backing plate during the cutting process. Individual specimens each had a single hole of radius 0.25, 1.25, 1.88, 2.5, or 5.0 mm, and five tensile test replications for each sample were performed.

2.3 Evaluation of inherent defect size and potential strength

All cellulosic webs contain inherent defects, whether due to poor formation, fiber damage, or non-uniform fiber bonding. The goal of this research was to determine an inherent defect size and a maximum potential tensile strength, σ_u, for paper materials. Maximum potential tensile strength is the tensile strength of defect-free material, but made with the same fibers, processing, bonding, and orthotropic properties as the web under inspection. Inherent defect size, R_{eff}, is determined by comparing the behavior of the sample material to that of models that estimate the effect of defect size.

2.3.1 Model development

Awerbuch and Madhukar [27] reviewed many semi-empirical strength models and concluded that each model could adequately represent the data so long as the empirical parameters were accurately determined. The PSC and average stress criterion (ASC), both created by Whitney and Nuismer [28], are modified here and applied to measured strength data of seven paper materials in Table 2.2. Modification of these models includes correction for finite-width specimens, assumption that defect-free tensile strength is unknown, and use of unnotched tensile strength to determine inherent defect size. The development of the modified PSC and ASC models follows.

For an infinite uniaxially loaded, linear elastic, orthotropic sheet containing a central circular hole of radius R (Figure 2.3), the tensile stress along the y-axis, beginning at the edge of the hole, $\sigma_y^{\infty}(x,0)$, $x \geq R$, is given by Lekhnitskii [29] as

$$\begin{aligned}\sigma_y^{\infty}(x,0) = \overline{\sigma}_y + \overline{\sigma}_y Re\Bigg\{ \frac{1}{\mu_1 - \mu_2} \Bigg[& \frac{-\mu_2(1 - i\mu_1)}{\sqrt{\gamma^2 - 1 - \mu_1^2}\left(\gamma + \sqrt{\gamma^2 - 1 - \mu_1^2}\right)} + \cdots \\ & \cdots + \frac{\mu_1(1 - i\mu_2)}{\sqrt{\gamma^2 - 1 - \mu_2^2}\left(\gamma + \sqrt{\gamma^2 - 1 - \mu_2^2}\right)} \Bigg] \Bigg\}\end{aligned} \tag{2.1}$$

where Re denotes the real part of the expression in the brackets, $\overline{\sigma}_y$ the far-field applied stress ($y \to \pm\infty$), $\gamma = x/R$, and μ_1 and μ_2 the two solutions of the following equation (μ_3 and μ_4 are complex conjugates of μ_1 and μ_2):

$$a_{22}\mu^4 - 2a_{26}\mu^3 + (2a_{12} + a_{66})\mu^2 - 2a_{16}\mu + a_{11} = 0 \tag{2.2}$$

In Equation 2.2, a_{ij}, $i, j = 1, 2, 6$, are compliances of the orthotropic material. In the present case, $a_{16} = a_{26} = 0$, and

$$\begin{bmatrix} a_{11} & a_{12} & a_{16} \\ \cdot & a_{22} & a_{26} \\ \cdot & \cdot & a_{66} \end{bmatrix} = \begin{bmatrix} \frac{1}{E_{11}} & -\frac{\nu_{12}}{E_{11}} & 0 \\ \cdot & \frac{1}{E_{22}} & 0 \\ \cdot & \cdot & \frac{1}{G_{12}} \end{bmatrix} \tag{2.3}$$

Complex material properties μ_i depend on E_{11}, E_{22}, ν_{12}, and G_{12}, where the 1 (MD, machine direction) and 2 (CD, cross-machine direction) directions are the orientations of material symmetry. Procedures for determining μ_i of Equation 2.2 are readily available [30] and must be determined for each material under consideration.

Using a similar approach to that of Khashaba [31], Tan's [32] finite-width specimen correction factor, FWC, is incorporated to adjust the stress distribution given as

$$FWC = \frac{K_T}{K_T^{\infty}} \quad \text{and} \quad \frac{K_T}{K_T^{\infty}} \sigma_y^{\infty}(x,0) = \sigma_y(x,0) \tag{2.4}$$

where K_T and K_T^{∞} are the tensile stress concentration factors at $(x,y) = (R,0)$ for a finite-width and infinite specimens, respectively, of the same material.

Enforcing y-direction equilibrium, for both the infinite width and finite-width specimens, is accomplished by integrating Equation 2.4, i.e.

$$\frac{RK_T}{K_T^{\infty}} \int_1^{W/2R} \sigma_y^{\infty}(x,0)\, d\gamma = \overline{\sigma}_y \cdot W/2 \tag{2.5}$$

This force equilibrium causes the FWC to uniformly increase the stress magnitude; Equation 2.4 assumes the same general stress profile along the x-axis from the hole for both an infinite- and finite-width geometries. Combining Equations 2.1 and 2.4 at $x = R$ gives

$$\begin{aligned} \frac{1}{FWC} = \frac{K_T^{\infty}}{K_T} = 1 - \frac{2R}{W} + Re \\ \left\{ \frac{1}{\mu_1 - \mu_2} \left[\frac{\mu_2}{1 + i\mu_1} \left(1 - \frac{2R}{W} - i\mu_1 \left(\frac{2R}{W} \right) - \cdots \right.\right.\right. \\ \cdots - \left. \sqrt{1 - \left(1 + \mu_1^2\right)\left(\frac{2R}{W}\right)^2} \right) - \cdots \\ \cdots - \frac{\mu_1}{1 + i\mu_2} \left(1 - \frac{2R}{W} - i\mu_2 \left(\frac{2R}{W} \right) - \cdots \right. \\ \cdots - \left.\left.\left. \sqrt{1 - \left(1 + \mu_2^2\right)\left(\frac{2R}{W}\right)^2} \right) \right] \right\} \end{aligned} \tag{2.6}$$

where W is the specimen width.

The PSC states that a tensile sheet containing a central circular hole of radius R fails when the longitudinal stress σ_y at a characteristic distance d_0 from the edge of the hole achieves the unnotched tensile strength of the material in the y-direction σ_U, i.e. failure occurs when $\sigma_y(R + d_0, 0) = \sigma_U$. Alternatively stated, failure occurs when the longitudinal stress throughout the distance adjacent to the edge of the hole d_0 exceeds the unnotched tensile strength σ_U.

In the foregoing discussion, the unnotched tensile strength σ_U is the strength of the material as determined by a conventional tensile test. σ_u (note lowercase subscript) is considered an unknown parameter. It is associated with processing defects and is to be determined via nonlinear least squares regression of the equation that results when σ_u is set equal to the product of Equation 2.1 and the reciprocal of Equation 2.6. Moreover, $\gamma_0 = (R + d_0)/R$, and μ_1 and μ_2 are the principal roots of Equation 2.2. To denote this change, the subscripts are changed such that $\sigma_U \rightarrow \sigma_u$. The resulting PSC as modified for a hole in a finite-width orthotropic plate is

$$
\begin{aligned}
&\sigma_u = FWC \cdot \sigma_H \cdot \Bigg\{ 1 + \cdots \\
&\cdots + Re \Bigg\{ \frac{1}{\mu_1 - \mu_2} \Bigg[\frac{-\mu_2(1 - i\mu_1)}{\sqrt{\gamma_0^2 - 1 - \mu_1^2(\gamma_0 + \sqrt{\gamma_0^2 - 1 - \mu_1^2})}} + \cdots \\
&\cdots + \frac{-\mu_1(1 - i\mu_2)}{\sqrt{\gamma_0^2 - 1 - \mu_2^2(\gamma_0 + \sqrt{\gamma_0^2 - 1 - \mu_2^2})}} \Bigg] \Bigg\} \Bigg\}
\end{aligned}
\tag{2.7}
$$

where σ_H is the experimentally measured tensile strength of the notched specimens and σ_u and γ_0 (i.e., d_0) are unknowns.

A related criterion to the PSC, using the same geometry, is the ASC, which assumes failure will occur when the average longitudinal stress over a distance, a_0, reaches the unnotched tensile strength of the material in the y-direction, σ_U (i.e., failure occurs when $\sigma_U = (1/a_0) \int_R^{R+a_0} \sigma_y(x, 0) dx$ [28]. The ASC, as modified for the present finite-width specimens, can be formally written as

$$
\begin{aligned}
\sigma_u = \frac{FWC \cdot \sigma_H}{a_0} \int_R^{R+a_0} \Bigg\{ 1 + \cdots \\
\cdots + Re \Bigg\{ \frac{1}{\mu_1 - \mu_2} \Bigg[\frac{-\mu_2(1 - i\mu_1)}{\sqrt{\gamma_0^2 - 1 - \mu_1^2(\gamma_0 + \sqrt{\gamma_0^2 - 1 - \mu_1^2})}} + \cdots \\
\cdots + \frac{-\mu_1(1 - i\mu_2)}{\sqrt{\gamma_0^2 - 1 - \mu_2^2(\gamma_0 + \sqrt{\gamma_0^2 - 1 - \mu_2^2})}} \Bigg] \Bigg\} \Bigg\} dx
\end{aligned}
\qquad (2.8)
$$

The strictly linear elastic PSC solution has been applied to nonlinear materials by many researchers including Kortschot and Trakas [26] and Perkins and Um [25], who both applied a quasi-isotropic PSC to paper; by Khashaba [31], who applied a modified PSC to a glass fiber reinforced polyester material; and by McNulty et al. [33], who applied PSC to Nicalon-reinforced ceramic composites. Significantly more applications have been made of the PSC than of the computationally more difficult ASC.

2.3.2 Numerical analysis

Unknown parameters σ_u and d_0 for Equation 2.7 and σ_u and a_0 for Equation 2.8 were determined by nonlinear least squares regression analysis within Matlab® via the built-in *nlinfit* function. Equation 2.7 was sensitive to initial estimates for the unknowns due to multiple local minima for these data. For the modified PSC of Equation 2.7, parameter convergence was realized when a ±10% change in the initial estimates converged to the same values. Equation 2.8 was insensitive to initial estimates and converged rapidly. Integration of Equation 2.8 was performed by trapezoidal rule. During nonlinear regression, $\sigma_u \geq \sigma_M$ was a condition, where σ_M is the mean unnotched tensile strength.

2.4 Results and discussion

The modified PSC (Equation 2.7) and modified ASC (Equation 2.8) were used to model the tensile behavior of specimens containing a single hole and for specimens that failed at the hole. Some combinations of material, orthotropic direction, and hole size did not fail at the prepared hole. These specimens were not included in the analysis and will be discussed separately. Inherent defect size was determined by reverse correlation as the intersection of σ_M with the modified PSC or ASC curves.

Figures 2.4-2.10 show the results of fitting the modified PSC and ASC curves to single hole tensile data. For the models, the modified PSC is represented by the dark line and the modified ASC by the gray line. Solid squares and circles each represent the measured tensile strength of a specimen when failure occurred away from the introduced hole. Open squares and circles each represent the measured tensile strength of a specimen when failure occurred at the introduced hole. The upper (squares) and lower (circles) sets of data for each graph are for testing in the one- and two-directions, respectively. Papermakers define the 1-direction as the machine direction (denoted by MD) and the 2-direction as the cross-machine direction (denoted by CD). For specimens loaded in each of the 1- and 2-directions, horizontal dashed lines are drawn at the mean measured unnotched tensile strength σ_M and intersect the model at an abscissa R_{eff}, the inherent defect size. Specimens with holes larger than the inherent defect size are expected to fail at the hole. Specimens with holes smaller than the inherent defect size are expected to fail elsewhere. Exceptions do occur, and these are likely explained by the concept of defect interaction [24]: The presence of the hole may increase local stresses elsewhere in the sheet causing failure away from the hole, even though the hole is larger than R_{eff}. Alternatively, stress variations away from the hole can increase stresses at the hole, producing failure at holes smaller than R_{eff}. The models provide an approach for averaging the test data to produce the best indication of R_{eff} regardless of exceptions.

In 9 of 14 cases in Figures 2.4-2.10 (seven materials and two directions), the calculated R_{eff} is characterized by tensile failures that avoid holes smaller than R_{eff} and select holes larger than R_{eff}. This is consistent with expectations. For example, Material E, 2-direction in Figure 2.5, no specimens having the 0.25 mm radius hole failed at the hole, whereas all five specimens with the 1.25 mm radius hole failed at the hole. The calculated R_{eff} (modified ASC) was the intermediate value 0.99 mm. Examining all nine similar cases indicates that the rule followed by Material E, 2-direction, was followed in 78 of the 90 tests of Figures 2.4-2.10. The 12 exceptions were likely caused by defect interactions.

In 2 of the 14 cases, Material E for 1-direction (Figure 2.5) and Material L1 for 2-direction (Figure 2.7), the calculated R_{eff} is bracketed by hole radii in specimens that failed at the hole. In Material E, 2 of 5 tests failed at 0.25 mm hole, perhaps because of stress enhancement by nearby natural defects. In Material L1, 5 of 5 failures occurred at 1.25 mm holes, when the R_{eff} value (modified ASC) was 1.49 mm. Because the failure

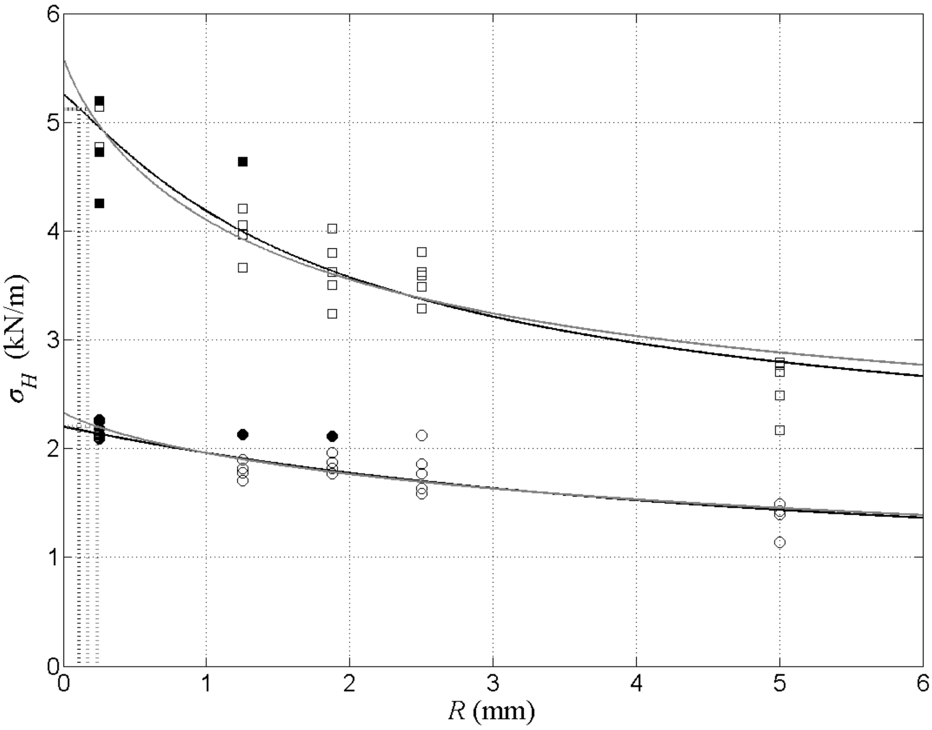

Figure 2.4: Modified PSC (dark line) and modified ASC (gray line) applied to Material C (copy paper) tensile data.

percentage of specimens with the smaller hole is 100%, it seems reasonable that strength is likely influenced by cumulative stress interactions among defects along the x-axis such that the introduced hole created a larger than expected defect.

For the remaining 3 of 14 cases shown in Figures 2.4-2.10, R_{eff} is less than 0.25 mm; that is, R_{eff} is less than the radius of the smallest hole used in this study. These cases are Material C in both 1- and 2-directions (Figure 2.4) and Material L1 in the 1-direction (Figure 2.7). For these cases, failure should have occurred at 0.25 mm hole. This happened for only 4 of 15 tests. In 11 tests, failure did not occur at the hole, perhaps because of stress shielding by nearby natural defects. This interpretation may be more likely in view of the small size of both the defect and the prepared hole.

Considering all 14 cases in this study, there is the question of defect interaction in 30 of 125 bracketing tests, or 24%. These 30 tests are all limited to specimens where the hole radius was close to R_{eff}. The average absolute discrepancy between R_{eff} and the hole radius is 0.22 mm for R_{eff} evaluated by the PSC model and 0.15 mm for R_{eff} evaluated by the ASC model. These values are influenced by statistical uncertainties in

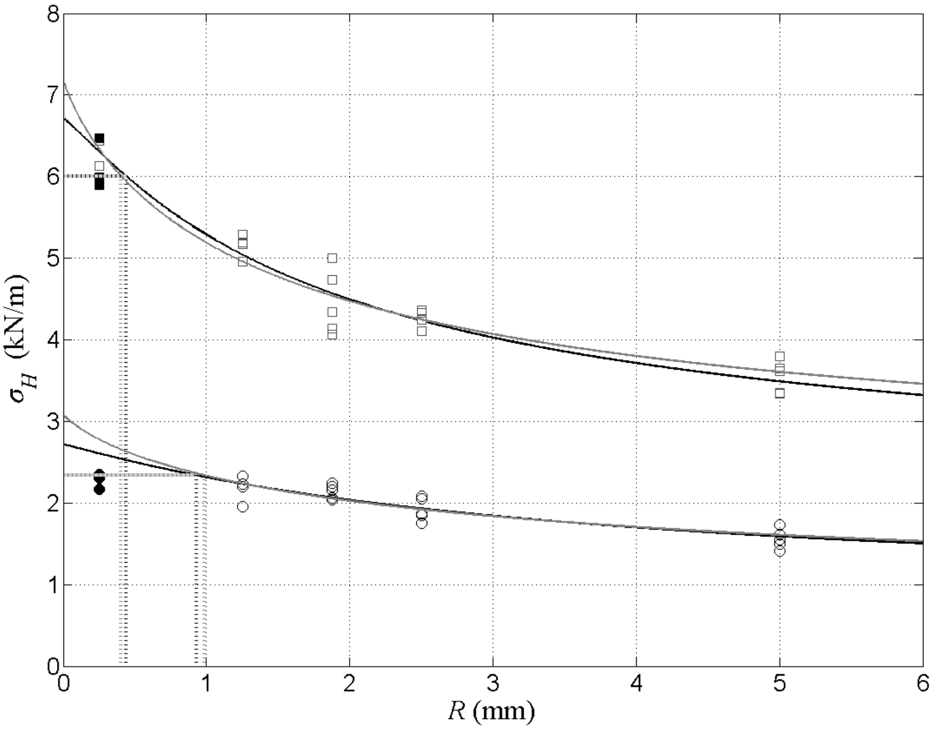

Figure 2.5: Modified PSC (dark line) and modified ASC (gray line) applied to Material E (envelope) tensile data.

the measurement of σ_M for the various specimens. Because the same values of σ_M are applied to both the PSC and ASC determination of R_{eff}, the two values are indicative of the relative accuracies of the two models. If, for purposes of discussion, these values are interpreted as absolute accuracies of the two models, the need to go outside the models to explain outliers is greatly reduced. For the ASC model, 17 of the 30 bracketing tests mentioned above are included within the ± 0.15 mm error bars of R_{eff}. Only 13 of 125 bracketing tests remain to defend in terms of defect interactions or otherwise, and 5 of these 13 were limited to material L1 discussed above. For the PSC model, 11 of 30 outlying tests are included within the ± 0.22 mm error bars of R_{eff}, leaving 19 of 125 bracketing tests to defend. Even with smaller error bars (inviting more outliers), the ASC model results in fewer outliers and provides a superior fit to the data. This suggests that the ASC picture of the influence of a hole on tensile strength may capture the physics of failure better than the PSC does, at least in paper samples.

The advantage of the ASC model is further demonstrated by results for Material C, 2-direction (Figure 2.4). For this sample, the regression limits established give $\sigma_u = \sigma_M$ and $R_{\text{eff}} = 0$ mm for the PSC model. However, according to Table 3, the same cases

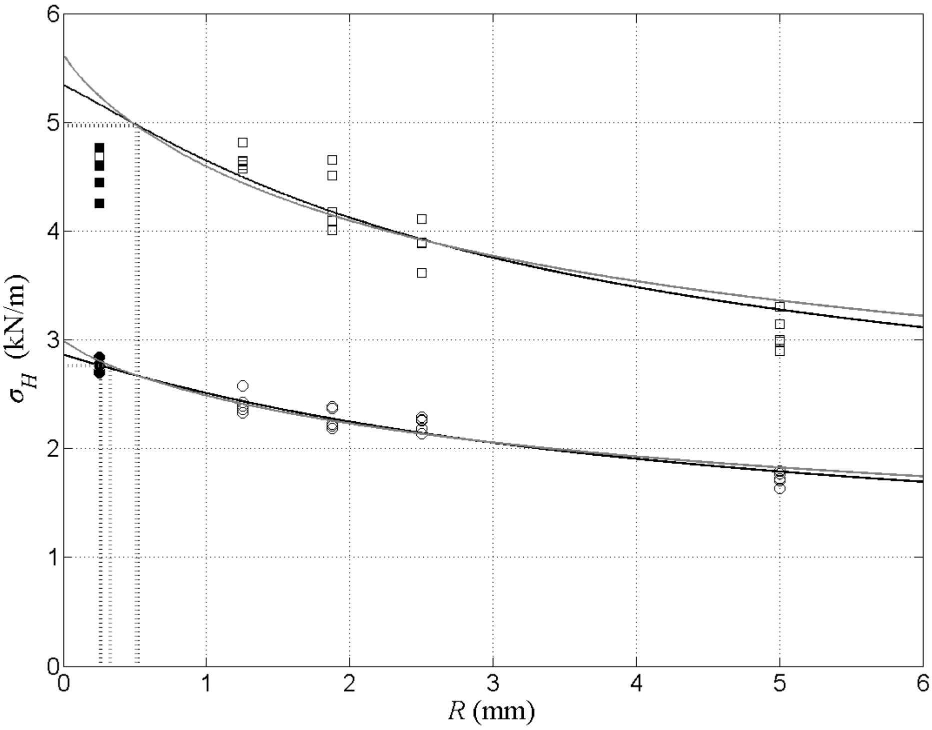

FIGURE 2.6: Modified PSC (dark line) and modified ASC (gray line) applied to Material F (filter paper) tensile data.

calculated $\sigma_u > \sigma_M$ and $R_{\text{eff}} > 0$ mm for modified ASC. This suggests that the ASC model may represent a more precise, as well as more accurate, measure of performance.

Both PSC and ASC models are able to differentiate between similar materials in ways that could ultimately prove very useful; for example, consider how the models treat similar, high grammage materials: linerboards L1 and L2, and cylinder boards S1 and S2. The exact compositions of materials L1 and L2 are unknown, and they were produced on different paper machines. Nevertheless, Table 2 shows that their densities and ultrasonic mechanical properties are very similar. Only in applying the models are differences made apparent. With R_{eff} close to 0 mm and $\sigma_u \sim \sigma_M$ in the 1-direction, sample L1 (Figure 2.7) is close to achieving its maximum potential. Though similar in many properties, Sample L2 (Figure 2.8) has considerable room for improvement in the 1-direction. In the 2-direction, L1 and L2 samples perform somewhat similarly. Both of these cases have room for improvement.

Materials S1 and S2 were manufactured on a cylinder machine, which typically produces a material with discrete layers, very similar to plies in laminated fiber-matrix composites.

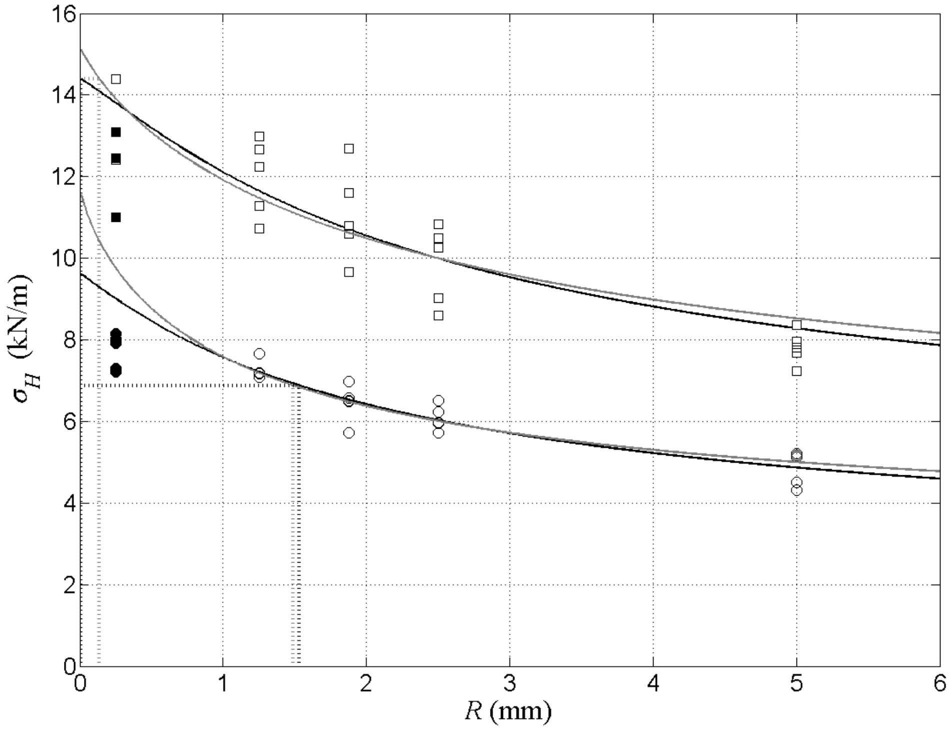

FIGURE 2.7: Modified PSC (dark line) and modified ASC (gray line) applied to Material L1 (linerboard 1) tensile data.

Additionally, uniform mass distribution is difficult to attain in the cylinder process. As such, these materials add a defect configuration to those present in conventional linerboard papermaking, namely defects between plies.

Figure 2.9 shows the analysis of Material S1 tensile behavior and illustrates its unique defect configurations. For the 1-direction, all specimens having either a 1.25 or 1.88 mm radius hole failed at these holes, but one of the specimens, which had a 2.5 mm radius hole, failed away from the hole. No other material demonstrated such behavior. The Material S1 in the 2-direction also exhibits some unique behavior in that one specimen of each of those whose hole radius was 1.25, 1.88, or 2.50 mm failed away from the hole. Characterization of an inherent defect size in cylinder-machine papers may not be as important as the demonstration that the material has many defect sizes present.

The supplier of Materials S1 and S2 explained that both materials were made on the same machine but that a proprietary processing change was made to enhance the converting performance of Material S2. Figure 2.10 shows an application of the models to Material S2 tensile behavior and indicates a more uniform defect configuration than

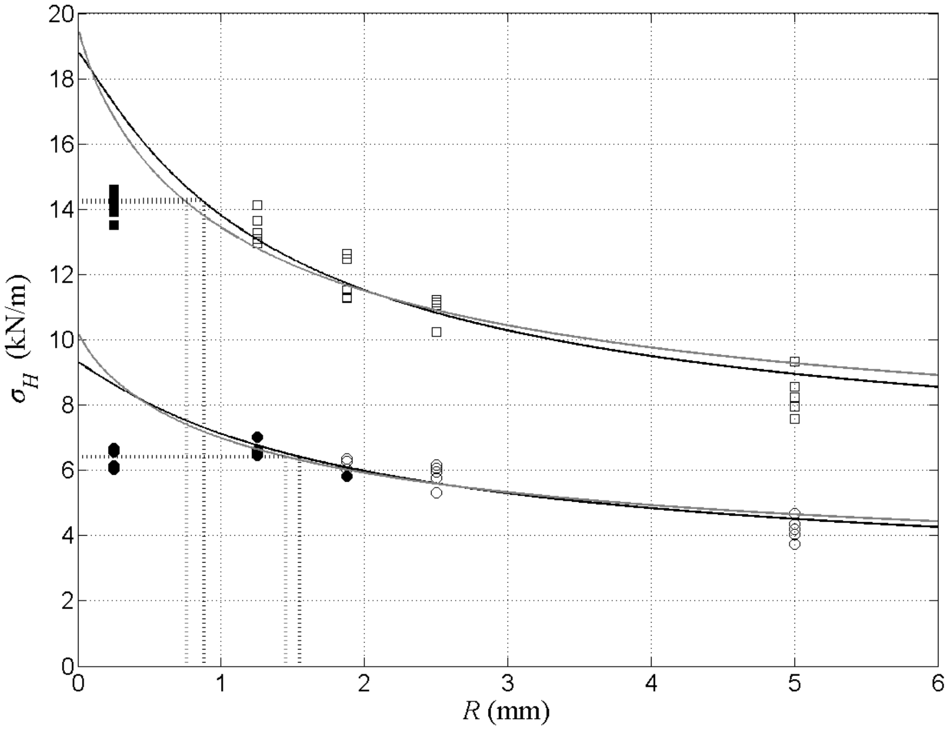

FIGURE 2.8: Modified PSC (dark line) and modified ASC (gray line) applied to Material L2 (linerboard 2) tensile data.

that of Material S1. In the 1-direction of Material S2, only 1 of 15 specimens having a hole of radius larger than R_{eff} failed away from the hole. In the 2-direction of the S2 Material (Figure 2.10), only one specimen failed at its 1.25 mm hole (close to R_{eff}) and all specimens having holes larger than R_{eff} failed at the holes. Distributions of inherent defect sizes in this material would seem to be narrower than that of Material S1, perhaps indicating improved ply bonding.

Table 2.3 summarizes results of the analysis. The calculated unnotched strength σ_u is considered to be the maximum potential tensile strength in a defect-free material made with the same fibers and corresponding fiber-to-fiber bonding. R_{eff} is calculated as the hole radius where the models produce the mean measured unnotched tensile strength σ_M. As such, R_{eff} is considered to be the size of the inherent defect in the material. Using a fracture mechanics approach, Donner [34] determined the defects in two newsprint samples (a short-fiber material) to range from 0.5 to 0.9 mm in the 1-direction and 1.2 to 1.7 mm in the 2-direction. These ranges are about twice the ranges observed for R_{eff} in Table 2.3 for papers that are made, for the most part, from long-fiber material.

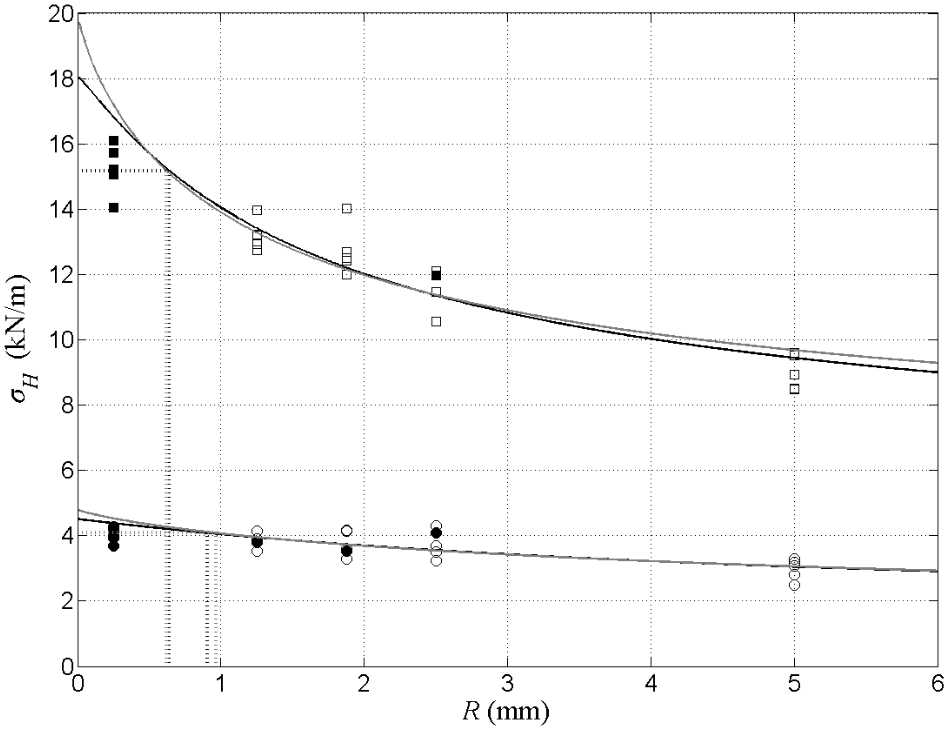

FIGURE 2.9: Modified PSC (dark line) and modified ASC (gray line) applied to Material S1 (cylinder board 1) tensile data.

TABLE 2.3: Calculated model parameters

			Point stress			Average stress		
Material	Direction	Measured unnotched strength σ_M (kN/m)	Calculated unnotched strength σ_u (kN/m)	σ_M/σ_u x100%	R_{eff} (mm)	Calculated unnotched strength σ_u (kN/m)	σ_M/σ_u x100%	R_{eff} (mm)
C	1	5.12	5.25	97.4	0.11	5.61	91.3	0.17
	2	2.20	2.20	100.0	0.00	2.33	94.3	0.24
E	1	6.00	6.72	89.4	0.44	7.20	83.3	0.40
	2	2.34	2.72	85.9	0.93	3.09	75.7	0.99
F	1	4.96	5.34	92.9	0.53	5.63	88.2	0.51
	2	2.76	2.86	96.5	0.26	3.00	92.1	0.33
L1	1	14.39	14.41	99.8	0.01	15.20	94.6	0.14
	2	6.88	9.63	71.4	1.53	11.72	58.7	1.49
L2	1	14.20	18.84	75.4	0.88	19.64	72.3	0.76
	2	6.41	9.32	68.8	1.55	10.28	62.4	1.45
S1	1	15.17	18.08	83.9	0.64	19.95	76.1	0.62
	2	4.08	4.51	90.5	0.91	4.80	85.0	0.97
S2	1	13.87	18.30	75.8	0.74	18.97	73.1	0.64
	2	3.94	4.77	82.7	1.15	5.33	74.0	1.20

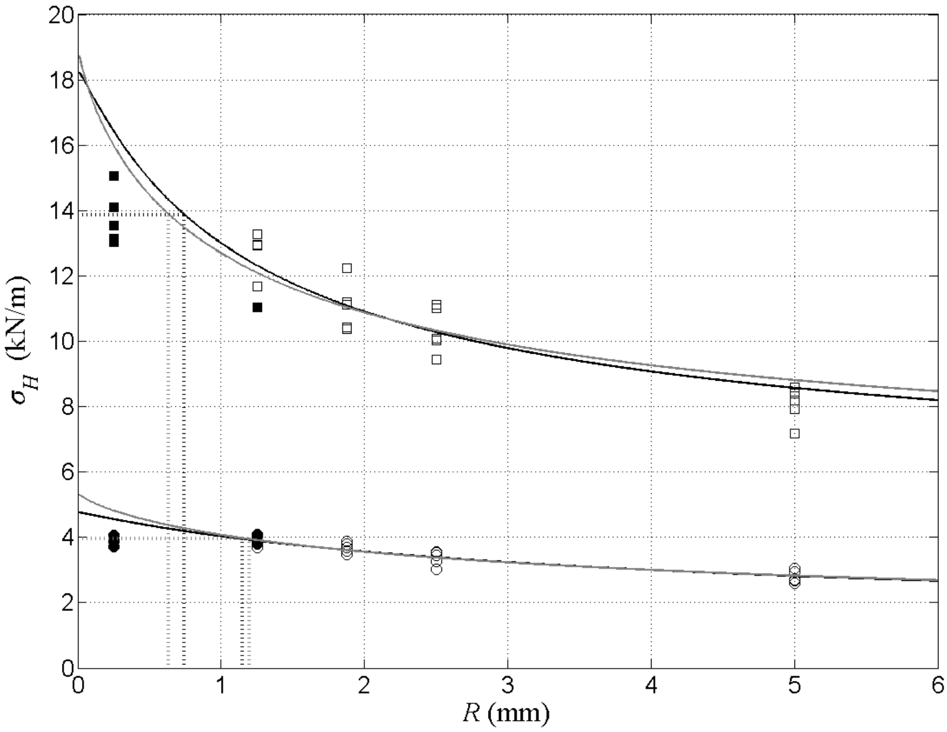

FIGURE 2.10: Modified PSC (dark line) and modified ASC (gray line) applied to Material S2 (cylinder board 2) tensile data.

The physical presence of a defect with a radius R_{eff} is unlikely. Rather, the inherent defect size accounts for innate interactions in the material during testing. Defects tend to interact with each other, producing lower or higher stresses than would be experienced independently. The combination of size and location of defects has not been thoroughly investigated except in special cases [35].

TABLE 2.4: Adjusted valued for R_{eff} based on binomial statistical hypothesis test

		Point stress		Average stress	
Material	Direction	R_{eff} (mm)	Adjusted R_{eff} (mm)	R_{eff} (mm)	Adjusted R_{eff} (mm)
E	2	0.93	0.88	0.99	0.95
L1	2	1.53	1.63	1.49	1.60
L2	1	0.88	0.87	0.76	0.75
	2	1.55	1.56	1.45	1.46
S1	1	0.64	0.66	0.62	0.63
	2	0.91	0.82	0.97	0.89
S2	1	0.74	0.73	0.64	0.63
	2	1.15	1.10	1.20	1.16

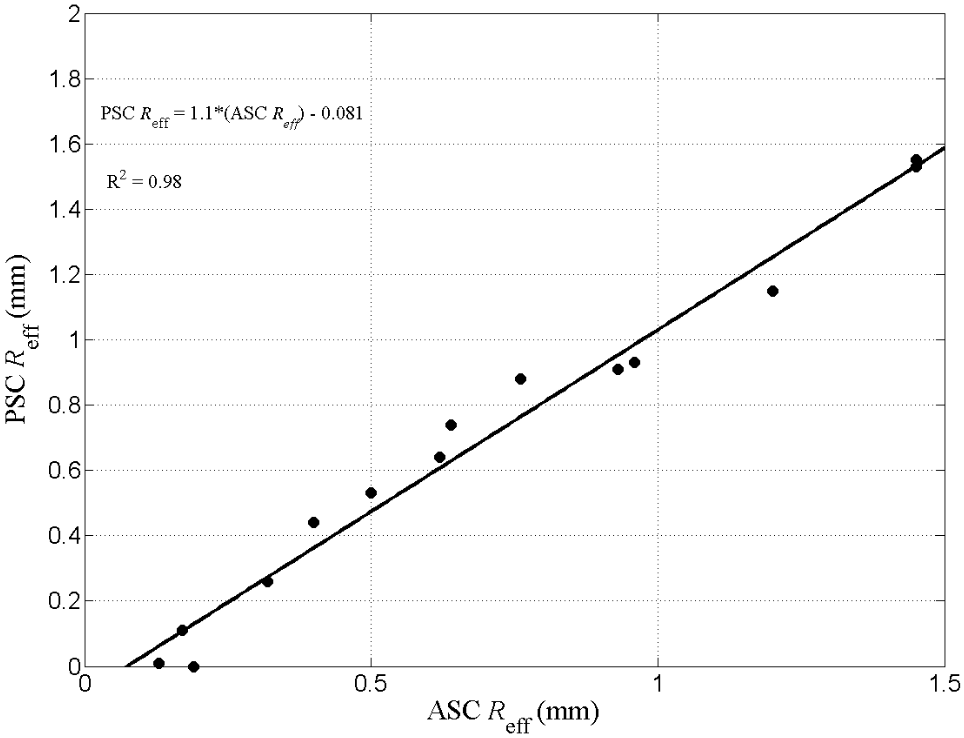

FIGURE 2.11: Relationship between ASC and PSC defect calculations.

Because both models, PSC and ASC, are based on the same stress distribution near the hole, Equation 2.1, the calculated defect sizes for each model are related to each other. Figure 2.11 shows the linear relationship between the R_{eff} values for PSC and ASC. For $R_{\mathrm{eff}} < 0.81$ mm, PSC predicts a smaller R_{eff} than does ASC. The modified ASC is more reliable during regression, is less sensitive to initial parameter estimates, and calculates a finite-sized inherent defect, even as $R_{\mathrm{eff}} \rightarrow 0$.

Figures 2.4-2.10 demonstrate the difficulty in application of Equations 2.7 and 2.8 to experimental strength data of materials with unknown defects, namely that by introducing a defect similar in size to the inherent defect, some failures will occur away from the introduced defect. Results of those tests were not included in the regression, thereby effectively adding statistical weight to results of the large hole strength data and reducing the effect of results near the region of interest (i.e., the smaller defects). To improve accuracy near the region of interest, for situations when the entire group of specimens failed away from the introduced defect, the standard binomial statistical-hypothesis test was used to test the hypothesis: *tensile specimens fail at the largest inherent defect.*

As stated earlier, the strength-controlling defect may be introduced, such as by hole punching, or it may be inherently part of the material. The standard binomial statistical-hypothesis test was used to determine the likelihood that the experimental strength would be above or equal to the model (either PSC or ASC). For the five replicates used in this study, only when all five specimens with the same introduced defect had strengths below the predicted (PSC or ASC) model would the one-sided alternative be significant at the 5% level, according to the two-sided table in Snedecor and Cochrane [36]. Such a result would violate the statistical rules of chance. For this study, the binomial hypothesis test indicated that the following materials failed at inherent defects that were larger than the smallest (0.25 mm) defect: E (2-direction), L1 (2-direction), L2 (both directions), S1 (both directions), and S2 (both directions).

For these eight cases, the strength data at 0.25 mm introduced defect can be moved to the R_{eff} for the particular sample and maintain variability of the model. These additional data were used to determine an adjusted R_{eff}. Table 2.4 gives the adjusted R_{eff} for samples in those eight cases. Adjusted R_{eff} was greater than original R_{eff} for Materials L1 (2-direction), L2 (2-direction), and S1 (1-direction) because the mean tensile strength of specimens with 0.25 mm defect was greater than for the unnotched specimen. All other adjusted R_{eff} values were less than original R_{eff}. Application of the binomial statistical hypothesis test changed R_{eff} in a manner expected from graphical observation.

2.5 Conclusion

The classical PSC and ASC have been modified to determine inherent defect size R_{eff} and maximum potential tensile strength σ_u for seven cellulose fiber materials. Calculated defect sizes were well related to observations during tensile testing relating to location of failure in that failure away from the introduced defect indicated an inherent defect larger than the introduced hole. As expected, printing and writing grade papers exhibit the smallest size defects. The models are effective for a wide range of material weights and two manufacturing methods. The modified ASC model had more rapid parameter convergence than the modified PSC model and calculated a finite-sized defect for all materials. Data were well characterized by the modified PSC and modified ASC even though these theories are strictly valid only for orthotropic linear elastic materials.

The binomial hypothesis test was used to determine cases where the inherent defect size analysis could be adjusted. The adjustment produced changes in accordance with observed data trends.

Because defect-free samples are the exception, the present approach extends the PSC and ASC in a manner beneficial for real-world situations. For the materials studied here, 30 tensile tests were sufficient for defect size and maximum potential tensile strength determination in one of the directions of orthotropy. Papermakers may use this approach to determine the favorable effect on strength of improving formation for cost-benefit analysis.

Chapter 3

General anisotropy identification of paperboard with the Virtual Fields Method

3.1 Introduction

Paper, paperboard and other cellulose fiber composites have received significant attention for use in materials and structures where biocompatibility is an important consideration because cellulose fiber composites are renewable, recyclable and compostable. However, even though single-sheet papermaking is more than 4000 years old and modern papermaking is 200 years old, analysis of paper's engineering properties remains a significant research area.

Production of paper and paperboard includes the separation of cellulose fibers, which are themselves anisotropic [37], from wood through a pulping process, which may be mechanical, as in newsprint, or chemical, as in sack paper. Resulting fiber flexibility and inter-fiber bonding are improved through additional mechanical action called beating. Absent requirements for fiber bleaching, the fibers are dispersed at low concentrations, usually less than 1% fiber/water, prior to being sprayed on a moving screen. Travel direction of the screen is called the machine direction (MD) while the in-plane direction perpendicular to the travel direction is called the cross-machine direction (CD). A combination of the spraying action and screen travel tend to orient the fibers in the MD which usually corresponds with the 1-direction of material properties. Depending on the type of paper produced papermachines can operate at speeds of 1500 m/min or higher. While ratios vary, the typical ratio for E_{11}/E_{22} is near 2. Offline stiffness measurement is used in process control [38]. Paper and paperboard are frequently sold on a strength/weight or stiffness/weight basis and so reduction of property variability and mechanical property improvement are persistent goals of papermakers, even though costs associated with variability are rarely acknowledged [39].

The objective of this work was to develop a load fixture and analysis method to identify the anisotropic stiffnesses of paper, paperboard and other thin materials. While the paper industry considers paper to be an orthotropic material, general anisotropy is developed if the MD is not aligned with the 1-direction and is called 'rotated orthotropy.' The assumption of orthotropy requires confirmation as the papermaking process has many variables affecting sheet mechanical properties including fiber properties, fiber orientation [40], fiber length distributions, sheet density, and drying restraint [41, 42]. Finally, identification of Q_{ij}, the in-plane stiffnesses, is important for process control [43] and for structures made from paper and paperboard, e.g. corrugated fiberboard [44], wound cores [45] and paper/foil composites [46]. Additionally, anisotropic Q_{ij} identification is important for other thin materials, including surgical meshes [47], biological tissues [48], textiles [49], rubber [50], among many others.

Identification of a fully-populated Q_{ij} matrix requires a specimen and load configuration in which heterogeneous strain fields of each ε_1, ε_2, and ε_6, are developed. Several methods have been proposed for creating those heterogeneous fields, such as uniaxial tensile coupons cut in different orientations [51], uniaxial tensile coupons with a central hole [52], cruciform [53], bulge tests [54], thin-walled cylindrical tubes [55]. Each of these specimens and load configurations had some aspect which made them unsuitable for the current work. For example, identification using uniaxial tensile specimens would require many specimens to develop statistical certainty of identification; other configurations would cause specimen wrinkling. Some specimens, such as cruciform specimens with and without central holes have stress concentrations at corners and/or holes where nonlinear constitutive behavior may be present. Small aspect-ratio tensile and bulge tests are incapable of producing different principal stress ratios. Tube configurations are complicated by a joining seam and the difficulty of full-field examination.

Most of the these geometries require some type of full-field measurement of displacements in order to determine strains and DIC (digital image correlation) [56] is the most common choice, and is used here, given its general ease of use and extensive development of analysis algorithms. In some cases greater measurement resolution is required and so holography [57], moiré [51], speckle interferometry [58] and grid methods [59] have been used. Techniques with less spatial resolution than DIC include grip displacement [60] and marker tracking [61**?**].

Parameter identification from full-field heterogeneous strains is accomplished by the use of an inverse method. VFM [1] was chosen for this work because it is general, flexible and faster than other methods which include FEM-Updating [62, 63], energy-based [64] and equilibrium gap [65] methods. VFM requires no additional programs, such as an FEM-solver, and analysis scripts can be easily written in Matlab®.

Ultrasonic techniques have also been used to determine the Q_{ij} of paper [66, 67]. Work by Habeger [67] appears to be the first attempt to determine Q_{16} and Q_{26} in paper materials. Three difficulties are associated with ultrasonic examination. First, significant wave attenuation occurs that requires sophisticated analysis to determine time-of-flight. Second, transmitted waves combine effects of all Q_{ij} and so relative scale of individual Q_{ij} makes it difficult to identify smaller parameters, such as Q_{16} and Q_{26}. Finally, in rate-dependent materials ultrasonic properties depend on excitation frequency.

In the current chapter, two cellulose-fiber webs were examined: a filter paper and a paperboard, a packaging grade known in the industry as linerboard. Details of the load fixture and analysis method, along with quantification of parameter identification accuracy are provided. The VFM analysis was extended to include identification of Q_{16} and Q_{26}, along with associated methods to reduce effect of strain measurement noise. While the analysis assumes that the materials are linear elastic and homogeneous, extension of the analysis to more general behavior is straight-forward. Comparison of Q_{ij} identification from VFM, ultrasonic and tensile coupons is included.

3.2 Material

Two materials were examined. The first material was Whatman® Chromatography Paper 3MM CHR and will be referred to as filter paper. It had nominal physical properties: grammage 180 g/m^2, thickness 0.28 mm and density 635 kg/m^3. Filter papers are used in a variety of household, commercial and scientific applications to capture particulate matter. The material was 100% cellulose as it is entirely comprised of cotton linters, a cellulose fiber that is typically 5-10 mm long.

The second material was a commercial unbleached, kraft single-ply linerboard which had nominal physical properties: grammage 209 g/m^2, thickness 0.30 mm and density 688 kg/m^3. Fiber composition of this material is unknown, but likely contains both virgin and recycled fibers. This material is commonly used in structural products such as corrugated fiberboard containers. Even as non-traditional packaging is being developed more than 3.5B m^2 [68] corrugated sheet stock were produced in 2011.

The materials will be referred to as Filter and Linerboard, but such designation is not meant to indicate these materials are general representatives of filter papers and linerboards. Each of these materials can be manufactured with an almost endless variety of fiber furnish, drying, pressing and additives.

3.3 Load Fixture

A schematic of the specially designed load fixture is shown in Figure 3.1; the actual fixture is shown in Figure 3.2. Forces are applied by four moveable grips on the top half of the fixture and measured with Sensotec (Honeywell International, Inc., Columbus, Ohio) Model 31BR load cells (range ±444 N) attached to Sensotec Model GM signal conditioners. The four grips located on the bottom half of the specimen are stationary. An additional fixture, not shown, was used as a template to cut the specimen and properly locate and punch holes for each grip. Prior to placing the specimen within the fixture, an alignment jig was used to adjust the top four grips to a precise starting location such that the specimen would experience no forces upon initial placement in the fixture. The aluminum knobs attached to the movable grips are rotated to generate radial tensile forces. A load configuration consisted of a unique force vector containing actual values for $F_1 - F_4$. Each specimen was subjected to multiple load configurations which created a series of different full-field strains for Q_{ij} evaluation. For each load configuration, individual forces were kept constant or increased, with respect to the previous load configuration, so that relaxation stiffnesses were avoided. As both materials were hygroscopic all tests were performed on the adsorption isotherm at 50%RH, 23°C.

The 24.5-cm-diameter specimen was gripped at eight locations 45° apart. Grips consisted of two small brass plates approximately 12 mm square. One plate had a threaded hole; the other a through-hole. Holes were punched at grip locations in the specimen, which was then clamped between plates with a small bolt. A torque wrench was used to ensure uniform clamping pressure for each grip. Special care was taken to prevent the top brass gripping plate from twisting and introducing undesirable stresses on the specimen. Without special care the initial stress state around the grips would have compressive stresses on one side and tensile stresses on the other side.

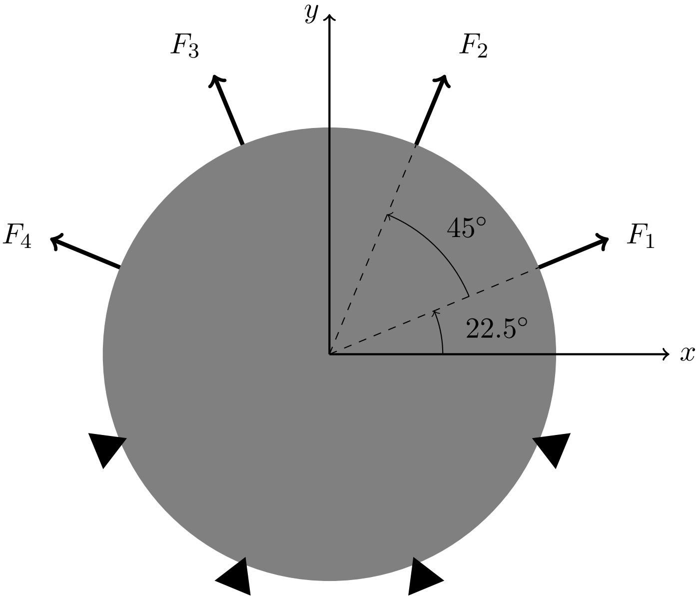

FIGURE 3.1: Schematic of load fixture.

3.4 Digital Image Correlation

The paperboard surface was examined with a Dantec® (Dantec Dynamics, Inc., Holtsville, New York) stereo DIC system whose details are listed in Table 3.1. The dot pattern was produced on the specimens using Sharp® (Sharp Electronics Corp., Mahwah, New Jersey) MX-3100N copier. Static specimen images were captured by waiting 5 min after load configuration adjustment. A single reference image was used for each test. For each specimen, the initial load configuration had forces approximately 15 N greater, at each load grip, than forces for the reference image. Initial forces on the specimen were used to ensure that the specimen was planar and grips were fully engaged.

3.5 The Virtual Fields Method

An abbreviated introduction to VFM is presented in order to introduce extension of VFM to identify a fully-populated Q_{ij} matrix; the recent book [1] provides full development

Figure 3.2: Actual load fixture.

Table 3.1: DIC system components and parameters

Camera	Allied Vision Technologies (Stadtroda, Germany) Stingray Model F504B
Lens	Computar (Commack, NY) M1614-MP2, 16 mm, f1.4
Lighting	Red LED, 4x3 array, wavelength 610-640 nm
Resolution	2452 x 2056
Facet Size	21 pixels, approx 3.3 mm x 3.3 mm
Software	Istra (Dantec) 4-D v2.1.5
Strain Smoothing	7x7 cubic spline

of VFM. For a plane stress problem, the Principle of Virtual Work can be written as

$$\int_S (\sigma_1 \varepsilon_1^* + \sigma_2 \varepsilon_2^* + \sigma_6 \varepsilon_6^*)\, dS = \int_{L_f} \bar{T}_i u_i^* dl, \tag{3.1}$$

where S is the area of 2-D domain, σ_i are stresses within S, u_i^* are kinematically admissible virtual displacements, ε_i^* are virtual strains associated with u_i^*, $\bar{T}_i$ are tractions applied on boundary of S, and L_f is the portion of S over which $\bar{T}_i$ are applied.

Assuming a linear elastic anisotropic material, the constitutive equation, using contracted index notation, is given by

$$\begin{Bmatrix} \sigma_1 \\ \sigma_2 \\ \sigma_6 \end{Bmatrix} = \begin{bmatrix} Q_{11} & Q_{12} & Q_{16} \\ Q_{12} & Q_{22} & Q_{23} \\ Q_{16} & Q_{26} & Q_{66} \end{bmatrix} \begin{Bmatrix} \varepsilon_1 \\ \varepsilon_2 \\ \varepsilon_6 \end{Bmatrix} \tag{3.2}$$

If the material is homogeneous, then each Q_{ij} is a constant and can be placed outside the integrals in Equation 3.1. Substituting Equation 3.2 into Equation 3.1 gives

$$\begin{aligned} Q_{11}\int_S \varepsilon_1\varepsilon_1^* dS + Q_{22}\int_S \varepsilon_2\varepsilon_2^* dS + Q_{12}\int_S \left(\varepsilon_1\varepsilon_2^* + \varepsilon_2\varepsilon_1^*\right) dS + \cdots \\ \cdots + Q_{16}\int_S \left(\varepsilon_1\varepsilon_6^* + \varepsilon_6\varepsilon_1^*\right) dS + Q_{26}\int_S \left(\varepsilon_2\varepsilon_6^* + \varepsilon_6\varepsilon_2^*\right) dS + Q_{66}\int_S \varepsilon_6\varepsilon_6^* dS = \int_{L_f} \bar{T}_i u_i^* dl \end{aligned} \tag{3.3}$$

In practice, six different u_i^* are used in Equation 3.3, one to identify each Q_{ij}. Special virtual fields simplify identification by choosing six different u_i^* so that only one integral term, one for each Q_{ij}, exists on the left side of Equation 3.3. By approximating the integrals in Equation 3.3 as discrete summations, a system of linear equations is developed whose solution requires minimal computation. As described earlier, DIC provides information on each ε_i throughout specimen surface and load cells provide values for each $\bar{T}_i$.

An important part of VFM analysis is to characterize the sensitivity of the identified parameters to strain noise. This work extends VFM to reduce the sensitivity to noise on parameter identification of Q_{16} and Q_{26} using the same procedure given by Avril et al. [69] for orthotropic Q_{ij}. They showed that variance of each Q_{ij}, $\mathbf{V}(\mathbf{Q})$, due to noise in strain measurements was given by:

$$\mathbf{V}(\mathbf{Q}) = \gamma^2 \left(\frac{S}{n}\right)^2 \mathbf{Q}^{\mathbf{app}} \cdot \mathbf{G} \cdot \mathbf{Q}^{\mathbf{app}}, \tag{3.4}$$

where γ is the amplitude of the strain noise represented by a zero-mean Gaussian distribution, S is the area of the specimen, n is the number of discrete measurements within S, $\mathbf{Q}^{\mathbf{app}}$ is the approximate Q_{ij} assuming noise is present but not accounted for and $\mathbf{G}$ is given by:

$$\mathbf{G}^{(ij)} = \begin{bmatrix} \sum_{i=1}^{n}\left(\varepsilon_{1,k}^{*(ij)}\right)^2 & 0 & \sum_{i=1}^{n}\varepsilon_{1,k}^{*(ij)}\varepsilon_{2,k}^{*(ij)} & 0 & \sum_{i=1}^{n}\varepsilon_{1,k}^{*(ij)}\varepsilon_{6,k}^{*(ij)} & 0 \\ 0 & \sum_{i=1}^{n}\left(\varepsilon_{2,k}^{*(ij)}\right)^2 & \sum_{i=1}^{n}\varepsilon_{1,k}^{*(ij)}\varepsilon_{2,k}^{*(ij)} & 0 & 0 & \sum_{i=1}^{n}\varepsilon_{2,k}^{*(ij)}\varepsilon_{6,k}^{*(ij)} \\ \sum_{i=1}^{n}\varepsilon_{1,k}^{*(ij)}\varepsilon_{2,k}^{*(ij)} & \sum_{i=1}^{n}\varepsilon_{1,k}^{*(ij)}\varepsilon_{2,k}^{*(ij)} & \sum_{i=1}^{n}\left(\varepsilon_{1,k}^{*(ij)}\right)^2+\sum_{i=1}^{n}\left(\varepsilon_{2,k}^{*(ij)}\right)^2 & 0 & \sum_{i=1}^{n}\varepsilon_{2,k}^{*(ij)}\varepsilon_{6,k}^{*(ij)} & \sum_{i=1}^{n}\varepsilon_{1,k}^{*(ij)}\varepsilon_{6,k}^{*(ij)} \\ 0 & 0 & 0 & \sum_{i=1}^{n}\left(\varepsilon_{6,6}^{*(ij)}\right)^2 & \sum_{i=1}^{n}\varepsilon_{1,k}^{*(ij)}\varepsilon_{6,k}^{*(ij)} & \sum_{i=1}^{n}\varepsilon_{2,k}^{*(ij)}\varepsilon_{6,k}^{*(ij)} \\ \sum_{i=1}^{n}\varepsilon_{1,k}^{*(ij)}\varepsilon_{6,k}^{*(ij)} & 0 & \sum_{i=1}^{n}\varepsilon_{2,k}^{*(ij)}\varepsilon_{6,k}^{*(ij)} & \sum_{i=1}^{n}\varepsilon_{1,k}^{*(ij)}\varepsilon_{6,k}^{*(ij)} & \sum_{i=1}^{n}\left(\varepsilon_{1,k}^{*(ij)}\right)^2+\sum_{i=1}^{n}\left(\varepsilon_{6,k}^{*(ij)}\right)^2 & \sum_{i=1}^{n}\varepsilon_{1,k}^{*(ij)}\varepsilon_{2,k}^{*(ij)} \\ 0 & \sum_{i=1}^{n}\varepsilon_{2,k}^{*(ij)}\varepsilon_{6,k}^{*(ij)} & \sum_{i=1}^{n}\varepsilon_{1,k}^{*(ij)}\varepsilon_{6,k}^{*(ij)} & \sum_{i=1}^{n}\varepsilon_{2,k}^{*(ij)}\varepsilon_{6,k}^{*(ij)} & \sum_{i=1}^{n}\varepsilon_{1,k}^{*(ij)}\varepsilon_{2,k}^{*(ij)} & \sum_{i=1}^{n}\left(\varepsilon_{2,k}^{*(ij)}\right)^2+\sum_{i=1}^{n}\left(\varepsilon_{6,k}^{*(ij)}\right)^2 \end{bmatrix} \tag{3.5}$$

where $\varepsilon^{*(ij)}_{m,k}$ is the special virtual strain ($m = 1, 2$ or 6) for the discrete region, k, associated with identification of a particular stiffness Q_{ij}.

Defining

$$\mathbf{V}(\mathbf{Q}) = \gamma^2\eta^2 \tag{3.6}$$

the standard deviations of Q_{ij} are given by η_{ij}. Due to the great differences in magnitude of Q_{ij} the coefficients of variation, η_{ij}/Q_{ij}, are commonly used to compare sensitivity of identified Q_{ij} to strain noise.

The remainder of the description regarding the use of **G** to minimize the effect of measurement noise on the identification of Q_{ij} corresponds to that given by Pierron and Grédiac [1], except that some scaling was used to reduce effects of great differences in magnitude of Q_{ij}. The larger **G** (6x6 for anisotropy vs 4x4 for orthotropy) given in Equation 3.5 slightly increases the number of iterations used for identification. In this work six iterations were typically sufficient for identification.

3.6 Selection of VFM Mesh

Most VFM applications use a virtual mesh of 4-node quadrilateral isoparametric elements, similar to a FEM mesh, to create kinematically admissible virtual fields. However, VFM mesh density analysis has no analogy to FEM mesh convergence studies, but balances competing influences of sufficient degrees of freedom for accurate parameter identification with the knowledge that increased mesh density amplifies the effects of strain noise and decreases accuracy of identification. Figures 3.3-3.5 show example VFM meshes at three mesh densities.

Choice of VFM mesh density for subsequent parameter identification was based on mesh's capacity to identify Q_{12} as the smallest Q_{ij} that was sure to exist; both Q_{16} and Q_{26} may be zero. Effect of mesh density on Q_{12} identification is shown in Figure 3.6; units are $\mathrm{km^2/s^2}$, or specific stiffness units, and are equivalent to $\mathrm{MN \cdot m/kg}$.

The criteria for mesh density was to choose the coarsest mesh that had sufficient degrees of freedom to identify all Q_{ij} and was appropriate for both materials. The difficulty for a 25 element mesh to identify small Q_{12} is not surprising as the mesh contains only four interior, unconstrained nodes, and therefore eight degrees of freedom, to identify six Q_{ij}. Above 225 elements the ability to detect small Q_{12} tends to decrease. The 36 element mesh appeared to have difficulty discerning the Poisson effect, probably due to interior

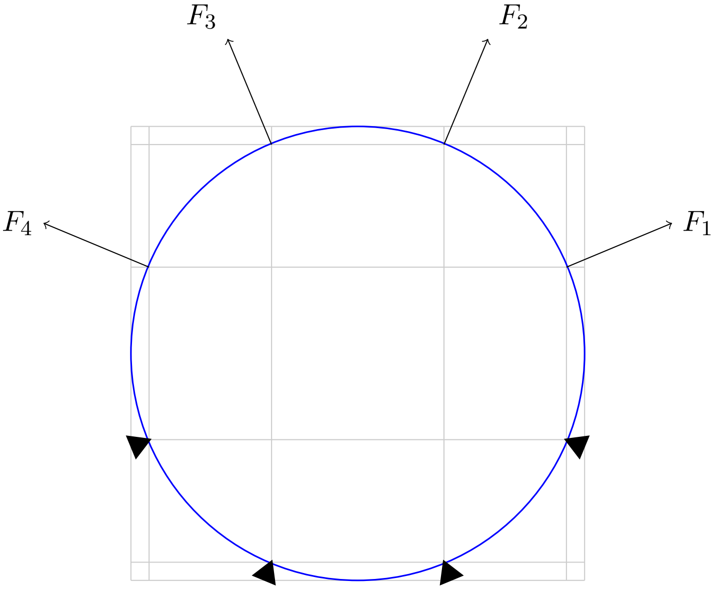

FIGURE 3.3: Example of 25 element virtual mesh for Figure 3.1.

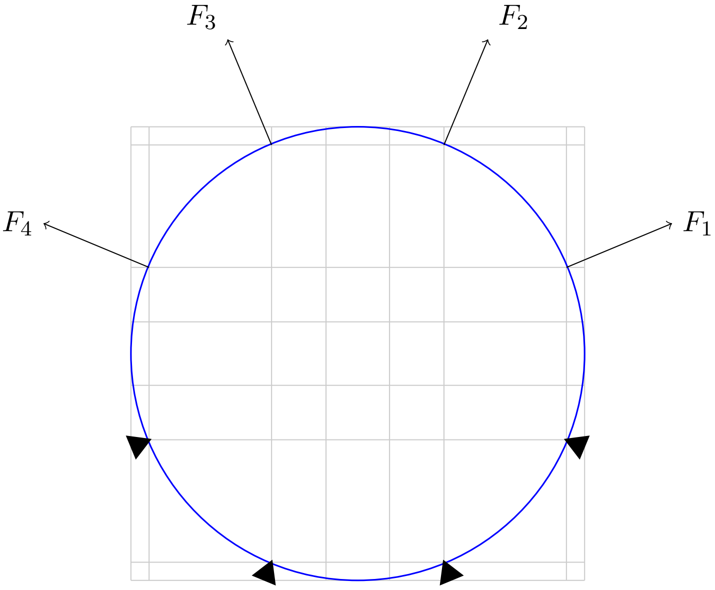

FIGURE 3.4: Example of 49 element virtual mesh for Figure 3.1.

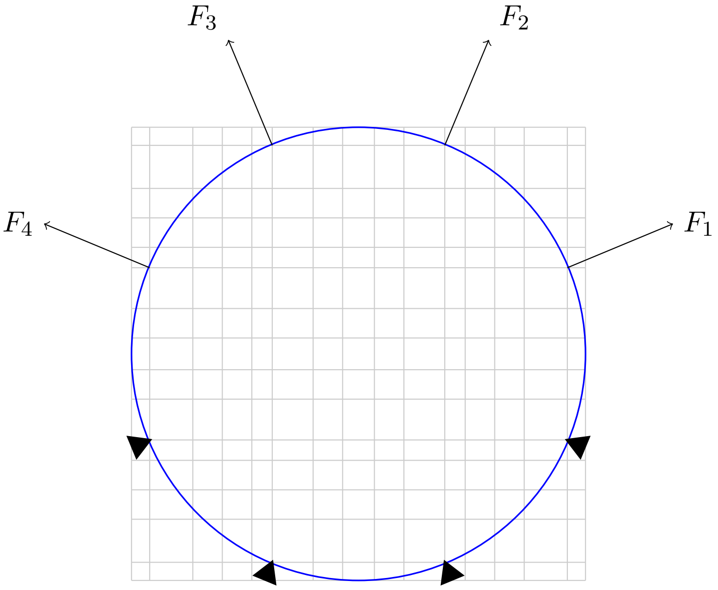

FIGURE 3.5: Example of 225 element virtual mesh for Figure 3.1.

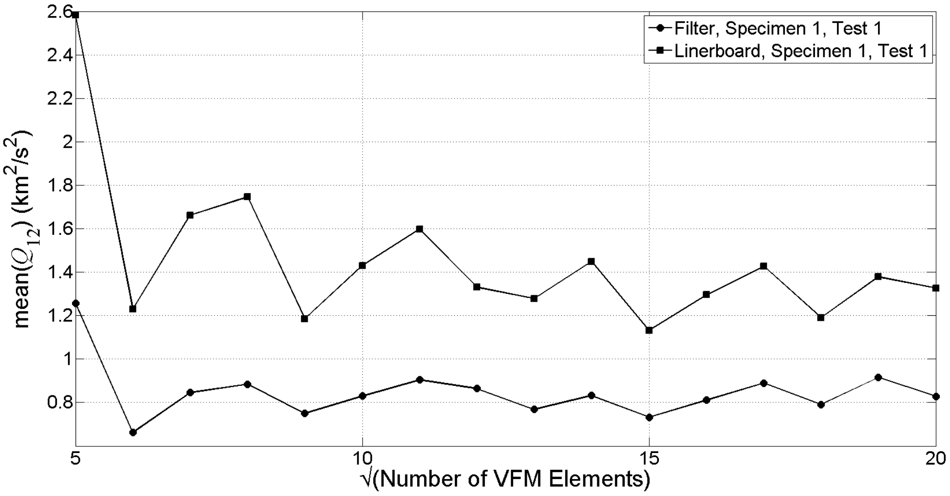

FIGURE 3.6: Q_{12} identification for different VFM mesh densities.

node locations that experienced very low strains. The 49 element mesh, Figure 3.4, contains 24 interior, unconstrained nodes and appeared to be the coarsest mesh, to reduce the effects of strain noise, for good identification and was used for all subsequent analyses. Differences in Q_{12} identification between the 49 and 64 element meshes were small and so the coarser mesh was selected.

In order to have a kinematically admissible virtual field, grip nodes are virtually fixed in both u and v displacement because they correspond to stationary grips in Figure 3.1.

Additionally, radially-oriented forces are prescribed at the load grips corresponding to forces F_4, F_3, F_2, and F_1. VFM meshes are not required to conform to specimen boundaries. Some VFM elements lie completely outside the specimen area, S, while other elements straddle the external boundary of S. Only terms in Equation 3.3 with nonzero, experimentally-measured ε_i have a contribution to stiffness evaluation.

3.7 Supporting Tests

Ultrasonic tests on individual specimens were performed with a Nomura Shoji® SST-250 paper tester. Transmission probe oscillated at 25 kHz. A central circular region, with 15 cm diameter, was examined for each specimen. Ultrasonic velocity was measured from 0° to 175° in 5° increments. Q_{66} was determined by measuring shear wave velocity transmitted along the 2-principal material direction using a second, modified SST instrument. The Musgrave Transformation [70, 71] was used to convert from wave velocity to phase velocity. Phase velocity was used to determine remaining stiffnesses, as Q_{66} was determined directly, according to the procedure described by Habeger [67].

Three tensile coupons were cut from each circular specimen after DIC and ultrasonic evaluations. Coupons were cut at 0°, 45°, 90° from 1-principal material direction. Coupons were 25 mm wide and each had a nominal gage length of 175 mm. Specimens were tested in an Instron® Model 5865 load frame with a grip displacement rate of 0.5 mm/min. DIC images were captured at 1 Hz and used to determine longitudinal and transverse strains. Longitudinal strains were used to determine E_{11} and E_{22} and transverse strains were used to determine ν_{12} and ν_{21} using the 0° and 90° coupons, respectively. Q_{66} was determined using data from all three coupons by stiffness transformation (Equation 3.7), as described in several sources, e.g. Jones [72].

$$Q_{66} = \frac{1}{\left(\frac{4}{E_{45}} - \frac{1}{E_{11}} - \frac{1}{E_{22}} + \frac{2\nu_{12}}{E_{11}}\right)} \tag{3.7}$$

Each test, VFM, ultrasonic and tensile, identifies a different Q_{ij}; VFM identifies secant tensile stiffness, ultrasonic identifies compression stiffness at very low strain levels and tensile identifies tangent tensile stiffness. For a linear elastic material all these different types of stiffness are the same. For nonlinear, viscoelastic materials ultrasonic Q_{ij} will be greater than the VFM secant Q_{ij}, that will, in turn, be greater than tensile Q_{ij}.

The rationale for choosing tangent stiffness as opposed to secant stiffness for tensile data was made because selection of the appropriate applied force to compare with this new geometry is not possible and tangent stiffness is used throughout the paper industry. The choice to use secant stiffness as opposed to tangent stiffness for this new geometry was based on the difficulty to measure strains between two adjacent load increments; importance of developing sufficient strains for Q_{ij} identification will be discussed in the next section. Example Linerboard tensile tests for MD and CD are shown in Figure 3.7.

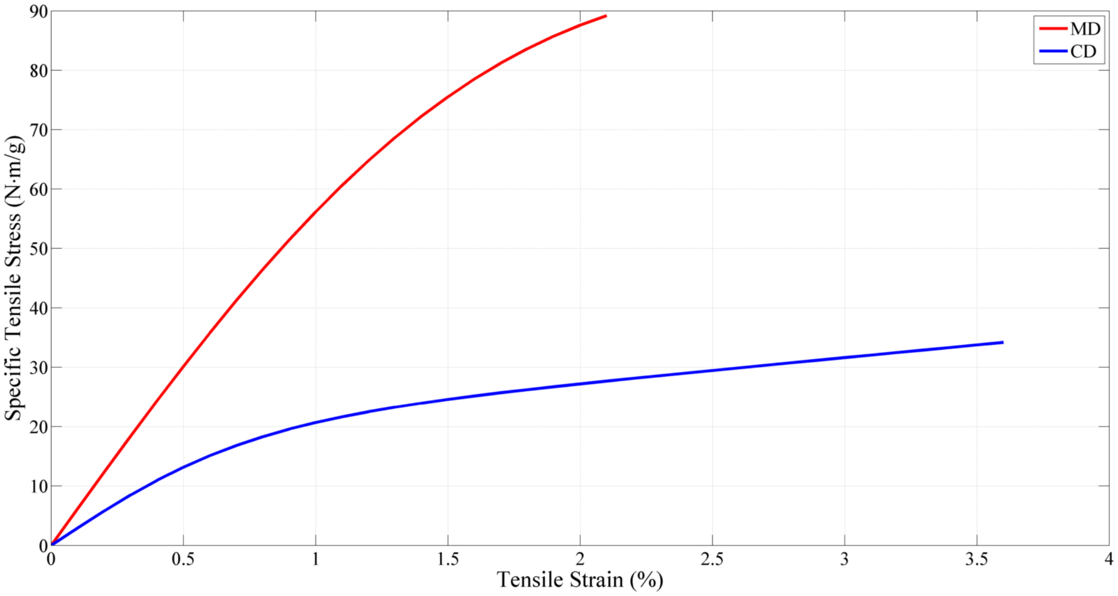

FIGURE 3.7: Example tensile tests for Linerboard.

3.8 Analysis

Three different specimens for each material, filter and linerboard, were tested with a minimum of ten load configurations; after the initial test, specimens were removed from load fixture, reinserted and retested.

As both materials were known to have nonlinear behavior it was assumed that only a range of load configurations could be used for linear elastic parameter identification. Determination of material nonlinear behavior is not straightforward for this load fixture. As the geometry was intentionally designed to produce sufficient strains, ε_i, for evaluation of all six Q_{ij}, it is not possible to directly determine onset of material nonlinear behavior. Furthermore, nonlinear behavior is unlikely to occur simultaneously for each Q_{ij}. An example pair of tests for each material is shown in Figure 3.8 which examines the manner in which forces induced strain in these tests, where norm refers to 2-norm, ε_c is given by Equation 3.8 and n is the number of strain measurements on the specimen surface. This figure suggests that the specimens behaved elastically for each load configuration and for each test. Elastic behavior is illustrated by the relative coincidence of points for each test of each material.

$$\varepsilon_c = \frac{1}{3n}\sqrt{\sum_{i=1}^{n}\left[(\varepsilon_{1,i})^2 + (\varepsilon_{2,i})^2 + (\varepsilon_{6,i})^2\right]} \tag{3.8}$$

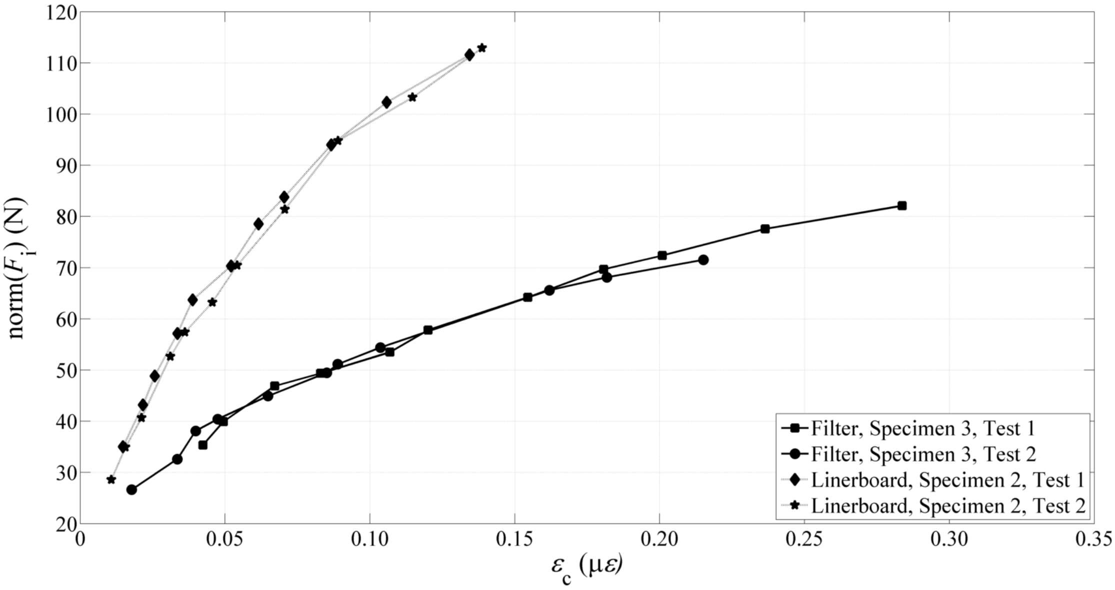

FIGURE 3.8: Examination of applied forces and induced strain for Filter, Specimen 3 and Linerboard, Specimen 2, where ε_c is given by Equation 3.8.

Figure 3.8 indicates nonlinear behavior occurred for both materials, but does not indicate non-linearity occurred for all ε_i and at all locations within the specimen. Nonlinear behavior was more likely to occur near the eight grips. Based on similar behavior for repeated tests, parameter identification was limited to load configurations where norm(F_i) was less than 65 N for Filter and 80 N for Linerboard.

An additional tool to determine quality of parameter identification is the comparison of η_{ij}/Q_{ij} for each load configuration, as seen in Figures 3.9 and 3.10 ; η_{16}/Q_{16} and η_{26}/Q_{26} are not shown to reduce vertical scale. Strains used for identification were determined from a single reference image, one for each material. Applied forces were the difference between those in the analyzed image and the reference image. Horizontal axes in these figures corresponds to vertical axis in Figure 3.8. An incremental analysis, where two consecutive loadings are compared, was not used because strain differences between two consecutive loadings were too small for identification. As expected, η_{12}/Q_{12} was higher than other η_{ij}/Q_{ij} because Q_{12} is generally smaller than Q_{11}, Q_{22}, and Q_{66} and is more difficult to identify as demonstrated by the non-monotonic behavior of η_{12}/Q_{12} with increasing norm(F_i). The other η_{ij}/Q_{ij} behaved consistently with improved identification, i.e. lower η_{ij}/Q_{ij}, with increasing forces and strains. Figures 3.9 and 3.10 were representative of identifications for each material. Based on this analysis, load configurations with any of η_{11}/Q_{11}, η_{22}/Q_{22}, or η_{66}/Q_{66} above 100 for Filter and above 200 for Linerboard were not used for identification.

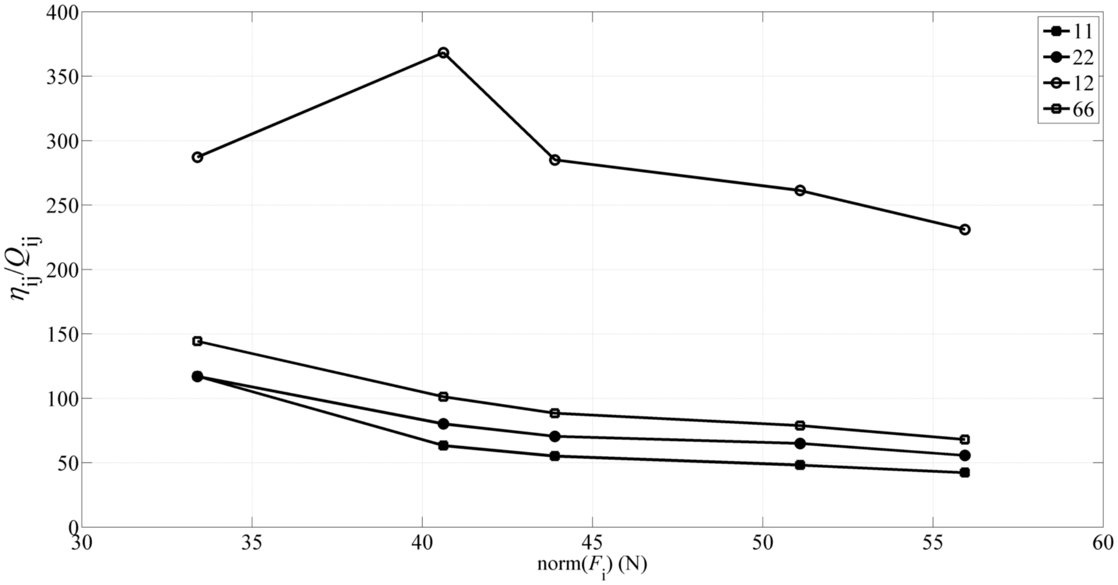

FIGURE 3.9: COV for Filter, Specimen 2, Test 2.

High η_{ij}/Q_{ij} for load configurations where norm(F_i) is less than 40 N, for either material, was expected given resolution of DIC strains. Figure 3.11 shows DIC strain for three scenarios, 3.11(a)-3.11(c), that had no change in forces between reference and analyzed image so norm(F_i) = 0 N, 3.11(d)-3.11(f) Linerboard, Specimen 1, Test 1, Load Configuration 1, where norm(F_i) = 34 N and, 3.11(g)-3.11(i) Linerboard, Specimen 1, Test 1, Load Configuration 5, where norm(F_i) = 62 N. Strain contours for 3.11(a) through 3.11(f) have few obvious differences while strain gradients for 3.11(g)-3.11(i) are more apparent. Furthermore, differences between the Q_{11}, Q_{22}, Q_{12}, and Q_{66} comparing 3.11(d)-3.11(f) to 3.11(g)-3.11(i) were only 13.8%, -5.9%, -13.3% and -6.2% respectively and validate the performance of VFM. The standard deviation of strains for the no load and Load Configuration 1 were very similar, showing that Load Configuration 1 had strain only slightly above the strain noise. The scale used in Figure 3.11 is quite small, hence the difficulty with identification. So, while parameter identification seemed

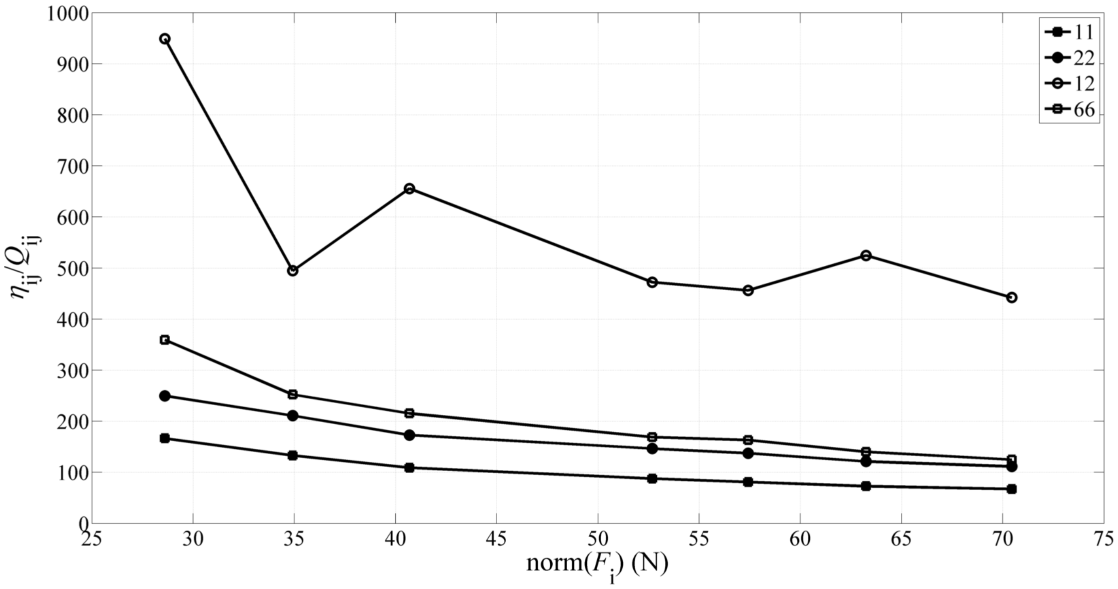

Figure 3.10: COV for Linerboard, Specimen 2, Test 2.

reasonable for small norm(F_i), those individual load configurations with high η_{ij}/Q_{ij}, as discussed earlier, were not used in the final analyses.

Load configurations for each material and test are given in Tables 3.2 -3.3. The last column identifies those configurations used in identification.

3.9 Results and Discussion

After selection of load configurations for each test those load configurations were superimposed to create a single, superposition load condition where ε_1, ε_2 and, ε_6 were created by the addition of the ε_i from each load condition and the F_i were created by the addition of forces from each load condition. A minimum of three load conditions were combined for each superposition identification.

Table 3.4 lists those results along with Q_{ij} determined from ultrasonic and tensile tests. Columns for I_1 and I_2 represent anisotropic stiffness invariants [73] and are given in Equation 3.9. The last column, ϕ, represents the difference from orthotropy as determined from Equation 3.10 from [67] where $\phi = 0°$ would be a perfectly orthotropic material and $\phi = 10°$ would denote an anisotropic material whose 1- and 2-principal material directions, where 1- and 2-direction correspond directions of maximum Q_{11} and Q_{22} respectively, are oriented 80° to each other.

Table 3.2: Load configurations for Filter, units (N)

Specimen	VFM Test	Load Configuration	F_1	F_2	F_3	F_4	norm(F_i)	Used for identification
1	1	1	16.90	17.35	18.99	17.79	35.55	
		2	18.24	21.35	27.49	19.13	43.70	
		3	19.13	22.69	27.62	20.91	45.61	*
		4	21.80	26.69	29.49	22.24	50.52	*
		5	24.02	30.69	32.69	25.35	56.84	*
		6	25.80	35.59	38.48	30.69	65.99	
		7	28.47	37.37	39.06	32.03	68.98	
		8	29.80	38.25	40.03	33.36	71.19	
		9	33.36	42.26	45.33	37.37	79.68	
		10	35.14	44.04	47.51	40.03	83.87	
	2	1	17.79	16.01	17.88	15.57	33.69	
		2	17.35	20.02	21.31	14.68	37.03	
		3	18.24	22.69	24.29	17.35	41.69	
		4	20.46	26.69	27.76	20.02	47.98	*
		5	23.13	28.91	29.71	21.80	52.24	*
		6	25.35	30.69	31.36	21.80	55.17	*
		7	26.69	34.70	35.81	23.58	61.27	*
		8	29.36	36.48	37.90	25.35	65.36	
		9	32.03	38.25	41.46	28.47	70.84	
		10	36.92	44.04	44.30	33.81	80.05	
2	1	1	14.23	16.90	21.97	12.01	33.40	
		2	16.01	21.35	25.53	16.90	40.62	
		3	17.79	21.35	28.38	18.68	43.90	
		4	23.58	25.35	30.29	22.24	51.10	*
		5	25.80	29.36	31.67	24.47	55.94	*
		6	28.47	32.47	34.70	26.24	61.30	*
		7	30.25	33.36	36.43	27.58	64.15	*
		8	32.47	35.14	40.17	29.80	69.22	
		9	33.81	36.92	40.92	30.69	71.57	
		10	33.81	40.03	43.33	33.81	75.93	
		11	34.70	44.04	45.55	37.81	81.53	
	2	1	12.90	21.35	19.53	17.35	36.12	
		2	15.12	24.02	23.00	20.02	41.66	
		3	16.46	25.35	25.93	24.02	46.51	
		4	17.79	27.13	27.85	27.13	50.64	*
		5	19.57	29.36	30.25	28.47	54.50	*
		6	20.91	32.47	33.14	31.14	59.66	*
		7	23.13	34.70	35.50	32.47	63.67	*
		8	24.47	36.48	37.01	34.25	66.87	
		9	28.02	38.25	38.61	36.03	70.98	
		10	29.36	38.70	40.83	38.70	74.33	
		11	32.47	42.70	47.91	40.03	82.32	
3	1	1	16.90	20.02	17.13	16.46	35.36	
		2	18.24	22.24	21.57	17.35	39.92	
		3	21.80	26.24	24.78	20.46	46.87	
		4	22.69	28.02	25.71	21.80	49.36	
		5	24.02	30.25	28.16	24.02	53.50	*
		6	24.91	32.92	30.43	26.69	57.81	*
		7	26.69	34.70	37.01	28.91	64.20	*
		8	29.80	37.37	39.32	32.03	69.69	
		9	31.14	38.70	41.06	32.92	72.36	
		10	33.81	41.37	43.55	35.59	77.57	
		11	36.92	44.04	44.04	38.70	82.09	
	2	1	15.57	12.01	14.10	11.12	26.63	
		2	16.90	17.79	16.81	13.34	32.61	
		3	20.02	20.02	17.39	18.68	38.12	
		4	21.35	20.91	19.79	18.68	40.42	
		5	22.69	22.69	22.24	22.24	44.93	
		6	24.02	27.13	23.62	24.02	49.48	*
		7	24.47	27.58	26.47	23.58	51.14	*
		8	27.58	30.25	27.00	23.58	54.41	*
		9	32.92	33.36	33.72	31.14	65.60	
		10	32.92	36.48	33.36	33.36	68.12	
		11	35.59	36.92	35.85	34.70	71.54	

Table 3.3: Load configurations for Linerboard, units (N)

Specimen	VFM Test	Load Configuration	F_1	F_2	F_3	F_4	norm(F_i)	Used for identification
1	1	1	16.90	18.24	15.88	16.46	33.78	
		2	20.02	23.13	20.73	19.57	41.81	
		3	21.80	27.13	23.44	22.69	47.70	*
		4	23.13	30.25	26.20	24.47	52.30	*
		5	27.13	35.14	33.45	27.58	62.05	*
		6	31.58	39.59	36.74	32.92	70.70	*
		7	34.70	43.59	40.70	35.14	77.43	*
		8	38.25	47.60	44.75	37.37	84.42	
		9	38.70	52.93	48.26	40.03	90.73	
		10	45.37	58.27	55.07	42.26	101.35	
		11	48.49	60.94	57.56	44.93	106.75	
	2	1	19.57	23.58	25.18	20.91	44.83	
		2	21.80	26.24	31.14	20.91	50.70	*
		3	25.80	32.92	37.68	24.91	61.56	*
		4	28.91	38.25	43.28	28.02	70.41	*
		5	31.14	41.37	43.95	29.80	74.17	*
		6	35.59	44.93	48.53	33.81	82.36	
		7	39.14	50.26	49.69	38.25	89.39	
		8	43.15	52.04	54.58	40.92	96.04	
		9	44.93	56.05	58.00	41.37	101.17	
		10	50.26	62.28	66.59	47.60	114.47	
		11	58.27	70.28	73.17	55.16	129.35	
2	1	1	22.69	22.69	20.95	23.58	44.99	
		2	28.91	30.69	26.64	26.69	56.57	
		3	28.91	31.14	29.58	27.13	58.45	*
		4	28.02	31.58	31.67	29.80	60.61	*
		5	29.80	35.59	35.94	33.81	67.74	*
		6	29.80	40.48	39.54	36.92	73.85	*
		7	35.59	42.70	41.15	38.70	79.25	*
		8	36.03	46.26	46.17	41.81	85.55	
		9	40.48	48.04	49.11	44.48	91.31	
		10	45.37	51.60	51.64	48.04	98.47	
		11	48.04	60.94	55.91	52.04	108.89	
	2	1	13.34	16.01	13.52	11.57	27.41	
		2	17.35	21.35	18.68	15.57	36.72	
		3	21.80	27.13	22.73	17.79	45.22	
		4	23.13	31.14	25.58	20.46	50.77	*
		5	27.58	34.70	29.67	23.13	58.14	*
		6	29.36	37.37	30.87	28.02	63.22	*
		7	32.47	40.48	33.32	30.25	68.69	*
		8	34.70	43.59	38.97	32.92	75.54	*
		9	35.59	50.26	42.57	36.48	83.28	
		10	39.59	53.82	49.38	40.03	92.22	
		11	42.26	57.83	51.02	43.15	97.95	
3	1	1	18.68	17.35	16.59	17.35	35.02	
		2	21.35	21.35	20.95	22.69	43.19	
		3	24.47	26.24	24.60	22.24	48.86	*
		4	27.58	30.69	29.18	26.69	57.15	*
		5	29.36	32.47	31.63	33.81	63.71	*
		6	32.92	35.14	36.92	35.59	70.34	*
		7	35.14	40.48	39.81	41.37	78.55	*
		8	40.03	42.26	41.64	43.59	83.80	
		9	44.93	47.60	47.37	48.04	94.00	
		10	49.82	50.71	52.04	52.04	102.33	
		11	53.38	58.27	56.67	54.71	111.58	
	2	1	16.01	13.79	15.75	11.12	28.60	
		2	19.13	18.24	19.13	12.46	34.92	
		3	21.35	21.80	22.55	14.68	40.68	
		4	28.91	29.36	27.58	17.79	52.68	
		5	30.69	31.14	31.09	20.46	57.42	*
		6	32.47	33.81	35.32	23.58	63.25	*
		7	35.59	38.25	39.59	25.80	70.45	*
		8	40.03	43.15	46.22	32.03	81.40	
		9	48.04	51.15	51.96	36.92	94.80	
		10	50.71	56.49	56.14	41.81	103.26	
		11	54.27	61.83	60.99	47.60	112.93	

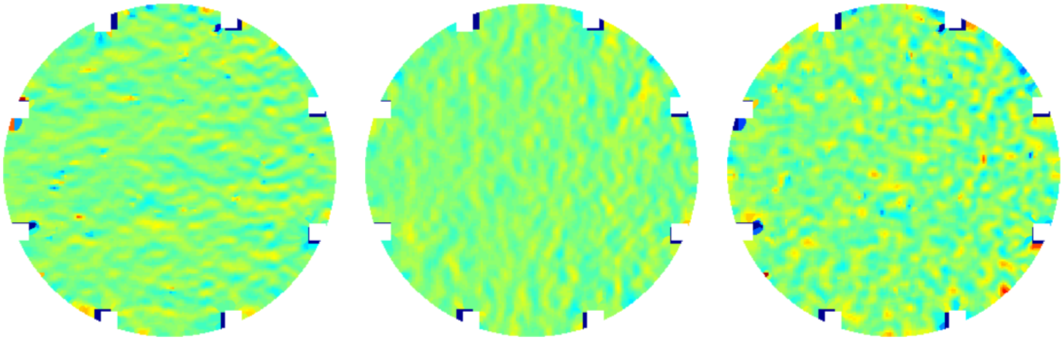

(a) ε_1 with no forces applied, standard deviation = 0.02 mm/m.

(b) ε_2 with no forces applied, standard deviation = 0.03 mm/m.

(c) ε_6 with no forces applied, standard deviation = 0.06 mm/m.

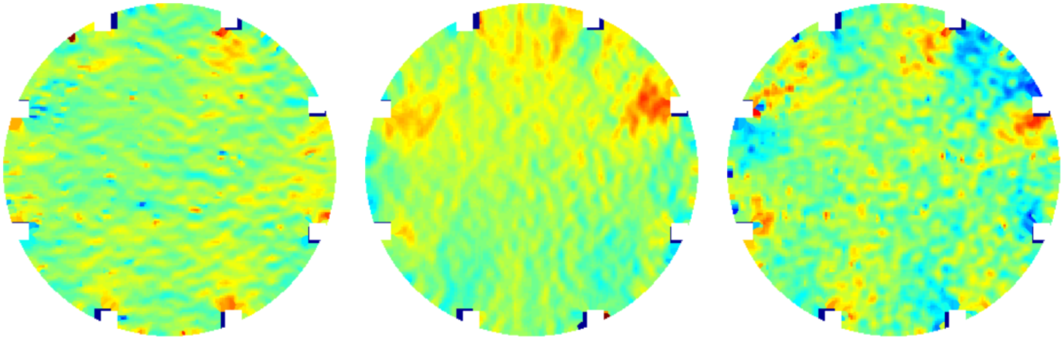

(d) ε_1 with Load Condition 1, standard deviation = 0.07 mm/m.

(e) ε_2 with Load Condition 1, standard deviation = 0.03 mm/m.

(f) ε_6 with Load Condition 1, standard deviation = 0.06 mm/m.

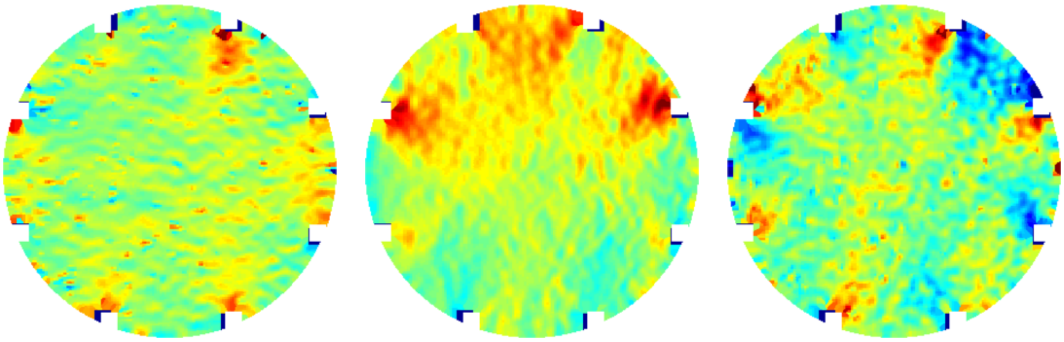

(g) ε_1 with Load Condition 5, standard deviation = 0.05 mm/m.

(h) ε_2 with Load Condition 5, standard deviation = 0.05 mm/m.

(i) ε_6 with Load Condition 5, standard deviation = 0.13 mm/m.

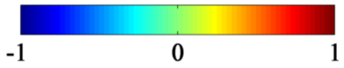

FIGURE 3.11: DIC strains for (a)-(c) no applied forces, (d)-(f) Linerboard, Specimen 1, Test 1, Load Configuration 1 (g)-(i) Linerboard, Specimen 1, Test 1, Load Configuration 5; units for scale (mm/m). Specimen diameter = 24.5 cm.

$$
\begin{aligned}
I_1 &= Q_{11} + Q_{22} + 2Q_{12} \\
I_2 &= Q_{66} - Q_{12}
\end{aligned}
\tag{3.9}
$$

$$\phi = -\frac{Q_{16}}{Q_{11} - Q_{12} - 2Q_{66}} - \frac{Q_{26}}{Q_{22} - Q_{12} - 2Q_{66}} \tag{3.10}$$

The 1-principal direction was nearly vertical (y-axis in Figure 3.1) for all tests so $Q_{22} > Q_{11}$; this specimen orientation was intentionally used to develop more strain in the stiffest direction because the y-axis is bracketed by load grips while the x-axis is bracketed by a load and stationary grip.

VFM identified Q_{11} and Q_{22} were generally larger than those determined by tensile tests and smaller than those identified ultrasonically and suggests that some nonlinear behavior was present. Ultrasonic identification of Q_{12} is difficult and the values given in Table 3.4 are larger than expected, especially when Poisson's Ratios are compared. Important considerations for ultrasonic measurements are that Q_{66} and Q_{12} are coupled and so errors in Q_{66} are propagated to Q_{12} and that Q_{12} has a smaller contribution to the phase velocity than Q_{11} and Q_{22}. Comparison of the invariants, I_1 and I_2, shows good agreement between VFM and tensile values while individual specimen ultrasonic values were higher for I_1 and lower for I_2.

Filter had general agreement with Q_{11} and Q_{22} among the tests, while Q_{12} and Q_{66} were lower for VFM identification than for ultrasonic or tensile tests. For an orthotropic material Q_{12} is the most difficult to identify using inverse methods [1]. However the consistently lower values for Q_{12} and the general agreement of the invariants suggest that the secant Q_{12} may be lower than Q_{12} identified with other methods. Differences between identification methods were more apparent for Linerboard. Q_{11} and Q_{22} were comparable for VFM and ultrasonic tests and were higher than for tensile tests. Those results agree with differences between secant and tangent modulus for nonlinear materials. As with Filter, the invariants of VFM and tensile were more similar than for ultrasonic tests. In general, the pattern of differences between Q_{ij} from each identification method were expected given that both materials have nonlinear behavior and sufficient strain is required to provide reasonable identification.

The combination of Q_{16}, Q_{26} and ϕ values near zero suggest that both materials were orthotropic. Linerboard, Specimen 3, Test 2 demonstrates rotated orthotropy because it had non-zero shear-coupled stiffnesses but near zero ϕ value. This particular test indicated the specimen was rotated 7.4° within the load fixture. Using stiffness transformation, the values for Q_{22}, Q_{11}, Q_{12}, and Q_{66} are 11.32, 5.61, 0.95, and 2.97 respectively, and have better agreement with Q_{ij} associated with Test 1 of that specimen.

Table 3.4: Comparison of different methods for evaluating Q_{ij}; units for Q_{ij}, I_1 and I_2 are km^2/s^2; units for ϕ are degrees

Material	Specimen	Test	Q_{11}	Q_{22}	Q_{12}	Q_{66}	Q_{16}	Q_{26}	I_1	I_2	ϕ
Filter	1	VFM-Test1	2.59	6.16	0.92	1.34	-0.12	-0.21	10.6	0.4	-0.04
		VFM-Test2	2.74	6.24	0.77	1.53	-0.08	0.16	10.5	0.8	-0.14
		Ultrasonic	3.29	6.91	2.21	1.68	-0.30	-0.05[a]	14.6	-0.5	-0.09
		Tensile	3.09	5.13	1.31	1.47	N/A	N/A	10.8	0.2	N/A
	2	VFM-Test1	2.85	6.10	0.79	1.17	-0.07	-0.38	10.5	0.4	-0.12
		VFM-Test2	2.59	7.46	1.07	1.39	-0.09	-1.10	12.2	0.3	0.23
		Ultrasonic	3.28	7.05	2.08	1.68	-0.18	-0.04[a]	14.5	-0.4	-0.06
		Tensile	2.98	5.70	1.35	1.53	N/A	N/A	11.4	0.3	N/A
	3	VFM-Test1	2.90	8.41	1.07	1.38	-0.05	-0.42	13.5	0.3	0.04
		VFM-Test2	3.45	6.40	1.10	1.08	0.03	-0.33	12.1	0.0	-0.05
		Ultrasonic	3.24	6.94	2.34	1.68	-0.14	0.03[a]	14.9	-0.7	-0.08
		Tensile	3.06	5.63	1.28	2.78	N/A	N/A	11.3	1.5	N/A
Linerboard	1	VFM-Test1	4.38	12.32	1.77	2.57	-0.14	0.42	20.2	0.8	-0.13
		VFM-Test2	3.82	11.86	1.43	2.75	-0.26	-0.05	18.5	1.3	-0.07
		Ultrasonic	5.16	12.42	4.63	2.51	-0.11	-0.22	26.8	-2.1	0.05
		Tensile	3.81	8.80	1.40	3.56	N/A	N/A	15.4	2.2	N/A
	2	VFM-Test1	6.07	13.82	2.16	3.21	-0.48	0.17	24.2	1.1	-0.22
		VFM-Test2	5.16	13.66	1.91	2.71	0.16	-0.04	22.6	0.8	0.08
		Ultrasonic	5.13	12.87	4.16	2.50	-0.17	-0.10	26.3	-1.7	-0.02
		Tensile	3.83	9.45	1.49	3.09	N/A	N/A	16.3	1.6	N/A
	3	VFM-Test1	5.46	11.16	1.41	2.10	0.02	-0.72	19.4	0.7	0.26
		VFM-Test2	4.65	11.19	1.49	3.51	-0.46	1.67	18.8	2.0	-0.74
		Ultrasonic	5.05	13.13	4.68	2.51	0.04[a]	-0.07[a]	27.5	-2.2	0.03
		Tensile	5.67	8.20	1.91	2.18	N/A	N/A	17.7	0.3	N/A

---

[a] Not statistically different from 0 at 95% confidence interval

Test repetition was used to demonstrate repeatability of results. As shown in Figure 3.8, applied forces produced similar strains for the first and second tests of each specimen. Table 3.4 show good repeatability of Q_{ij} for each replication. Differences can be justified by a small specimen rotation disagreement between tests, as discussed previously, or by some specimen damage caused by unintentional plastic deformation. Specifically, damage seems to have occurred during tests of Linerboard, Specimens 1 and 2 because Q_{ij} for Test 1 were higher than for Test 2.

Parameter identification by inverse methods is improved by using the experimentally measured data to determine the fewest possible parameters. Since our identification results indicate both materials were orthotropic it is appropriate to examine the possibility that the materials were 'special' orthotropic in which Q_{66} is independent of orientation angle, as most recently discussed by Ostoja-Starzewski and Stahl [74] and predicted for other composite materials by Vannucci [75]. For materials of this type the normal four orthotropic constitutive parameters are reduced to three according to Equation 3.11, where E_{11}, E_{22}, ν_{12}, and ν_{21} can be expressed in terms of Q_{11}, Q_{22}, and Q_{12}. Figure 3.12 compares the identified Q_{66} with Q_{66}^s as determined by Equation 3.11, where those parameters were determined by rotating the VFM-identified Q_{ij} to their principal directions. Figure 3.12 suggests that Filter and Liner may be special orthotropic, but additional testing would be required for more definitive affirmation.

$$\frac{1}{Q_{66}^s} = \frac{1+\nu_{12}}{E_{11}} + \frac{1+\nu_{21}}{E_{22}} \tag{3.11}$$

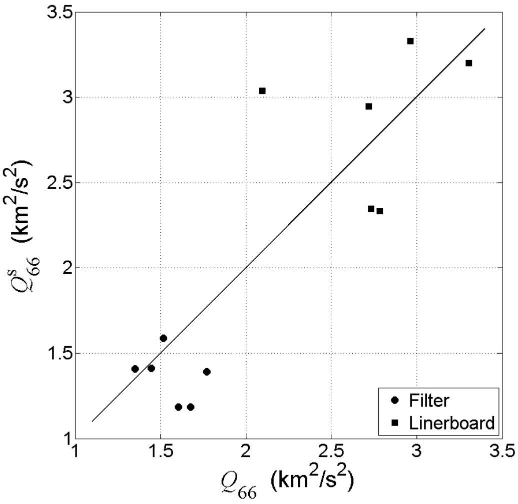

FIGURE 3.12: Examination of angular independence of Q_{66}; line denotes $Q_{66} = Q_{66}^s$ and is not a fit to the data.

3.10 Conclusion

A new load fixture and VFM parameter identification process applicable to general anisotropic sheet materials have been created. This process improves parameter identification in cases where material principal directions are not known a priori or specimen fabrication is not aligned with material principal directions.

An overview was presented of the manner in which this new load fixture can be used for parameter identification. Future use of this fixture will quantify the effect of specimen orientation and load configuration on identified parameters, similar to that performed by Pierron et al. [76] and Rossi and Pierron [77] on the unnotched Iosipescu specimen geometry. Some combination of orientation and load configuration may provide optimum strain contours to improve identification and reduce noise effects.

This work extended VFM identification to general anisotropic sheet materials and introduced a novel load fixture designed to produce the necessary strain fields. DIC was used to investigate full-field strains under a variety of multi-axial load configurations for two different paper materials. Quantification of nonlinear constitutive behavior, quality of parameter identification, and examination of the effect of VFM mesh density were performed. For each material, VFM-evaluated Q_{ij} were repeatable and compared favorably with those determined by ultrasonic and tensile coupon tests. A multi-step process is provided to improve VFM parameter identification through recognition of orthotropy and to recognize independence of angular orientation of Q_{66}.

Chapter 4

Stiffness identification of simulated heterogeneous materials with VFM

4.1 Introduction

In Chapter 3 identification of anisotropic Q_{ij} with VFM was validated by performing experiments and comparing the identification with those determined by ultrasonic and tensile tests. It is not feasible to perform a similar validation for heterogeneous materials because material fabrication is an important component of the analysis. Use of numerically simulated materials eliminates that component and provides greater confidence that the identification algorithms are effective. This chapter describes validation of VFM parameter identification on numerically simulated heterogeneous materials.

Pierron and Grédiac [1] have used simulated tests and materials to develop optimal test geometry for parameter identification. Rossi and Pierron [77] have created a test simulator that numerically reproduces the entire measurement and analysis process to find the best compromise between experiment variables. Devivier et al. [78] numerically simulated damage in composite materials to validate a detection algorithm.

The objective of this chapter is to verify analysis procedures used to identify local stiffnesses in heterogeneous materials. Because the precise nature of stiffness gradients in cellulose materials is unknown procedures were developed that range from broad scope identification to a narrow scope. Heterogeneous materials were simulated with

FEM models and their local stiffnesses were determined. These analyses were used to characterize systematic error in identification, benefits of one method over another and validation of the proposed methods. Accuracy and resolution were addressed directly, where possible, and indirectly in other cases.

The overall goal of this thesis is the characterization of the heterogeneity of paper. Whether paper is used as a structural material, for communicating a message in print or a moisture barrier it is generally not sold directly to the consumer. Instead, paper is usually sold to a converter who adds value to the paper through specific processes. The integrity of the paper is critical for the converter and quality issues are discovered in their converting processes. These processes not only require a certain paper quality but also uniformity of quality. As stated by Bristow and Kolseth in [79]'Uniformity of quality depends on uniformity of structure.'

The inability to relate physical properties, e.g. mass and fiber orientation, and mechanical properties provides an important motivation for this work. The primary focus of paper structure has been on mass uniformity, e.g. [80]. However, local fiber orientation varies throughout paper and the manner of variation depends on papermachine variables [81]. Enomae et al. [82] measured macroscopic fiber orientation and found that fiber orientation did not, in general, agree with ultrasound-measured anisotropy. These works suggest three different types of heterogeneity in paper materials, mass-based, mass-based with non-uniform fiber orientation and stiffness-based but uncorrelated to any mass-based heterogeneity. Therefore, parameter identification algorithms should be constructed cognizant of these types of heterogeneity.

Improvements in DIC coupled with VFM analyses provide a new opportunity to inspect local stiffness behavior independent of mass variation. This work focuses on development of VFM analyses appropriate of heterogeneous evaluation of materials.

4.2 Application of VFM to heterogeneous materials

Three modifications to previous VFM analyses are presented for the purpose of heterogeneity characterization. The PVW (Equation 3.1 for 2-D case) provides the basis for use of VFM to examine heterogeneous materials.

4.2.1 Location of inclusion known a priori

Assume that the region S in Equation 3.1 contains an inclusion whose location and boundaries are known. If $S = S_1 \cup S_2$, where S_2 is the inclusion region and S_1 is all of S outside S_2, then PVW can be rewritten as

$$\int_{S_1} \left(\sigma_1 \varepsilon_1^* + \sigma_2 \varepsilon_2^* + \sigma_6 \varepsilon_6^*\right) dS_1 + \int_{S_2} \left(\sigma_1 \varepsilon_1^* + \sigma_2 \varepsilon_2^* + \sigma_6 \varepsilon_6^*\right) dS_2 = \int_{L_f} \bar{T}_i u_i^* dl \tag{4.1}$$

Accordingly, if k inclusions exist within S, then the left hand side of Equation 4.1 would contain $k+1$ integral terms, where the $+1$ refers to the region not contained in the inclusions, i.e. the matrix material. For simplicity, the following development will assume only a single inclusion, but the development for multiple inclusions is straightforward.

If S_1 and S_2 are assumed to be comprised of different linear elastic anisotropic materials then Q_{ij} are constants and can be placed outside the integrals in 4.1. Using Q_{ij}^k, where $k = 1, 2$ denotes region S_1 or S_2 the new equilibrium equation becomes

$$\begin{aligned}
Q_{11}^1 \int_{S_1} \varepsilon_1 \varepsilon_1^* dS_1 + Q_{22}^1 \int_{S_1} \varepsilon_2 \varepsilon_2^* dS_1 + Q_{12}^1 \int_{S_1} \left(\varepsilon_1 \varepsilon_2^* dS_1 + \varepsilon_2 \varepsilon_1^*\right) dS_1 + \cdots \\
\cdots + Q_{16}^1 \int_{S_1} \left(\varepsilon_1 \varepsilon_6^* + \varepsilon_6 \varepsilon_1^*\right) dS_1 + Q_{26}^1 \int_{S_1} \left(\varepsilon_2 \varepsilon_6^* + \varepsilon_6 \varepsilon_2^*\right) dS_1 + Q_{66}^1 \int_{S_1} \varepsilon_6 \varepsilon_6^* dS_1 + \cdots \\
Q_{11}^2 \int_{S_2} \varepsilon_1 \varepsilon_1^* dS_2 + Q_{22}^2 \int_{S_2} \varepsilon_2 \varepsilon_2^* dS_2 + Q_{12}^2 \int_{S_2} \left(\varepsilon_1 \varepsilon_2^* + \varepsilon_2 \varepsilon_1^*\right) dS_2 + \cdots \\
\cdots + Q_{16}^2 \int_{S_2} \left(\varepsilon_1 \varepsilon_6^* + \varepsilon_6 \varepsilon_1^*\right) dS_2 + Q_{26}^2 \int_{S_2} \left(\varepsilon_2 \varepsilon_6^* + \varepsilon_6 \varepsilon_2^*\right) dS_2 + Q_{66}^2 \int_{S_2} \varepsilon_6 \varepsilon_6^* dS_2 = \cdots \\
\cdots = \int_{L_f} \bar{T}_i u_i^* dl
\end{aligned} \tag{4.2}$$

While no limit on the number of S_k exists, Q_{ij}^k identification requires sufficient strain data, ε_i, for each region. Practical experience in this work has shown unstable identification for $k > 5$.

Additional development of VFM for cases in which inclusion location and geometry are known corresponds to work in Section 3.5.

4.2.2 Q_{ij} varies spatially

If the material is assumed to be heterogeneous, but the nature of the heterogeneity is unknown, the Q_{ij} can be approximated by a spatially varying function such as $Q_{ij} = f_{ij}(x, y)$ where x, y represent coordinate location within the material. Here a polynomial is used to describe Q_{ij} as follows

$$\begin{aligned}
Q_{11} &= \sum_{i=1}^{n+1}\sum_{j=1}^{n+1} \alpha_{11}^{ij}(\frac{x_1}{R})^{i-1}(\frac{x_2}{R})^{j-1} \\
Q_{22} &= \sum_{i=1}^{n+1}\sum_{j=1}^{n+1} \alpha_{22}^{ij}(\frac{x_1}{R})^{i-1}(\frac{x_2}{R})^{j-1} \\
Q_{12} &= \sum_{i=1}^{n+1}\sum_{j=1}^{n+1} \alpha_{12}^{ij}(\frac{x_1}{R})^{i-1}(\frac{x_2}{R})^{j-1} \\
Q_{66} &= \sum_{i=1}^{n+1}\sum_{j=1}^{n+1} \alpha_{66}^{ij}(\frac{x_1}{R})^{i-1}(\frac{x_2}{R})^{j-1} \\
Q_{16} &= \sum_{i=1}^{n+1}\sum_{j=1}^{n+1} \alpha_{16}^{ij}(\frac{x_1}{R})^{i-1}(\frac{x_2}{R})^{j-1} \\
Q_{26} &= \sum_{i=1}^{n+1}\sum_{j=1}^{n+1} \alpha_{26}^{ij}(\frac{x_1}{R})^{i-1}(\frac{x_2}{R})^{j-1},
\end{aligned} \tag{4.3}$$

where R is the radius of the circular specimen used for examination.

Equation 4.3 is written specifically for this work; a more general formulation would include different polynomial order for x_1 and x_2 variation and for each Q_{ij}. This work uses a fourth order polynomial, i.e. $n = 4$, unless otherwise specified. The α_{kl}^{ij} are constants and can be placed outside the integrals; Equations 3.2 and 4.3 are substituted into Equation 3.1 to create a VFM for a polynomial Q_{ij} as

$$
\begin{aligned}
&\sum_{i=1}^{n+1}\sum_{j=1}^{n+1}\alpha_{11}^{ij}\int_S\left(\frac{x_1}{R}\right)^{i-1}\left(\frac{x_2}{R}\right)^{j-1}\varepsilon_1\varepsilon_1^*dS+\cdots\\
&\cdots+\sum_{k=1}^{n+1}\sum_{l=1}^{n+1}\alpha_{22}^{kl}\int_S\left(\frac{x_1}{R}\right)^{k-1}\left(\frac{x_2}{R}\right)^{l-1}\varepsilon_2\varepsilon_2^*dS+\cdots\\
&\cdots+\sum_{p=1}^{n+1}\sum_{q=1}^{n+1}\alpha_{12}^{pq}\int_S\left(\frac{x_1}{R}\right)^{p-1}\left(\frac{x_2}{R}\right)^{q-1}\left(\varepsilon_1\varepsilon_2^*+\varepsilon_2\varepsilon_1^*\right)dS+\cdots\\
&\cdots+\sum_{r=1}^{n+1}\sum_{s=1}^{n+1}\alpha_{16}^{rs}\int_S\left(\frac{x_1}{R}\right)^{r-1}\left(\frac{x_2}{R}\right)^{s-1}\left(\varepsilon_1\varepsilon_6^*+\varepsilon_6\varepsilon_1^*\right)dS+\cdots\\
&\cdots+\sum_{t=1}^{n+1}\sum_{u=1}^{n+1}\alpha_{26}^{tu}\int_S\left(\frac{x_1}{R}\right)^{t-1}\left(\frac{x_2}{R}\right)^{u-1}\left(\varepsilon_2\varepsilon_6^*+\varepsilon_6\varepsilon_2^*\right)dS+\cdots\\
&\cdots+\sum_{v=1}^{n+1}\sum_{w=1}^{n+1}\alpha_{66}^{vw}\int_S\left(\frac{x_1}{R}\right)^{v-1}\left(\frac{x_2}{R}\right)^{w-1}\varepsilon_6\varepsilon_6^*dS+\cdots\\
&=\int_{L_f}\bar{T}_iu_i^*dl
\end{aligned}
\tag{4.4}
$$

Additional development of VFM for cases in which Q_{ij} vary spatially corresponds to work in Section 3.5. The polynomial Q_{ij} formulation of VFM is used to estimate location of inclusions and stiffness variation within a specimen.

4.2.3 Equilibrium gap

A further development in the virtual fields method [78] comes from the understanding that PVW can also be used to examine local equilibrium. A similar procedure has been used to examine errors in FEM modeling [83]. Discrepancies in local equilibrium are ‘equilibrium gaps’ and can be used to locate boundaries of regions which are not in equilibrium with each other when material homogeneity is assumed.

Equation 3.3 can be written as:

$$
\begin{aligned}
&Q_{11}\int_S\varepsilon_1\varepsilon_1^*dS+Q_{22}\int_S\varepsilon_2\varepsilon_2^*dS+Q_{12}\int_S\left(\varepsilon_1\varepsilon_2^*+\varepsilon_2\varepsilon_1^*\right)dS+Q_{16}\int_S\left(\varepsilon_1\varepsilon_6^*+\varepsilon_6\varepsilon_1^*\right)dS+\cdots\\
&\cdots+Q_{26}\int_S\left(\varepsilon_2\varepsilon_6^*+\varepsilon_6\varepsilon_2^*\right)dS+Q_{66}\int_S\varepsilon_6\varepsilon_6^*dS-\int_{L_f}\bar{T}_iu_i^*dl=0
\end{aligned}
\tag{4.5}
$$

Equation 4.5 describes the equilibrium of a region S, where S is a portion of a larger region. If all Q_{ij} are known and u^* are kinematically admissible then summation of the integrals should be zero; a non-zero result is termed to be an 'equilibrium gap.'

A piecewise approach to the virtual fields was used with four elements, as shown in Figure 4.1. The four elements cover a region under inspection. The inspection window, comprised of the 4 virtual elements, is rastered, horizontally and vertically, across the entire specimen. Two parameters can be adjusted to produce different types of EG maps, the number of data points in each element and the movement of the inspection window to the next location. For this work two different window sizes were used; each virtual element contained 4 simulated-DIC data points (2 points horizontally x 2 points vertically) or 25 simulated-DIC data points (5 points x 5 points). The inspection window was moved by a single simulated-DIC row or column.

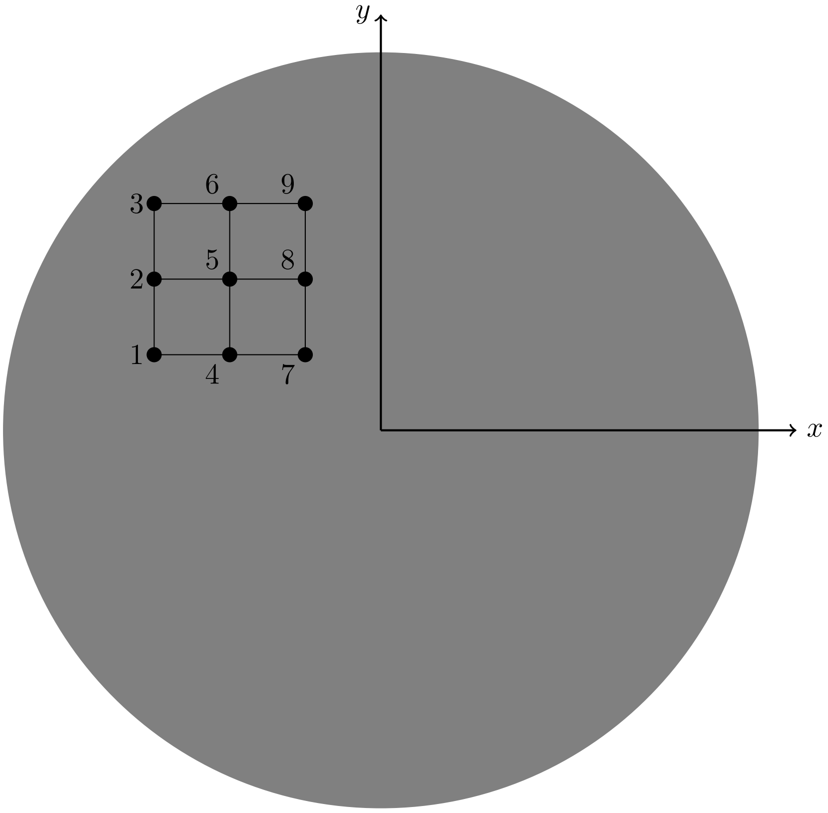

FIGURE 4.1: Four virtual elements used in EG analysis.

All virtual degrees of freedom for nodes on the edge of the inspection window are set to zero, i.e. nodes 1, 2, 3, 4, 6, 7, 8, 9. This process eliminates all work of external forces on the window boundary. Node 5 is subject to a horizontal displacement fixed at

$u = 1$. Equation 4.5 is discretized using summations and the equilibrium gap contour is determined by sliding the window over the entire specimen.

4.3 Model Geometry

Model geometry was based on work in the previous chapter in which a circular specimen under multiaxial force produced heterogeneous strain fields for determination of the six anisotropic Q_{ij}. The same model is used here and is shown in Figure 4.2. Forces and fixed positions are 45° apart and are offset from the global coordinates by 22.5°. The 150 N forces were chosen based on estimated total forces of the superposition tests used in Chapters 3 and 5. The appropriateness of the geometry will be demonstrated to be independent from the load configuration to demonstrate the ability of VFM to identify hetergeneous Q_{ij}.

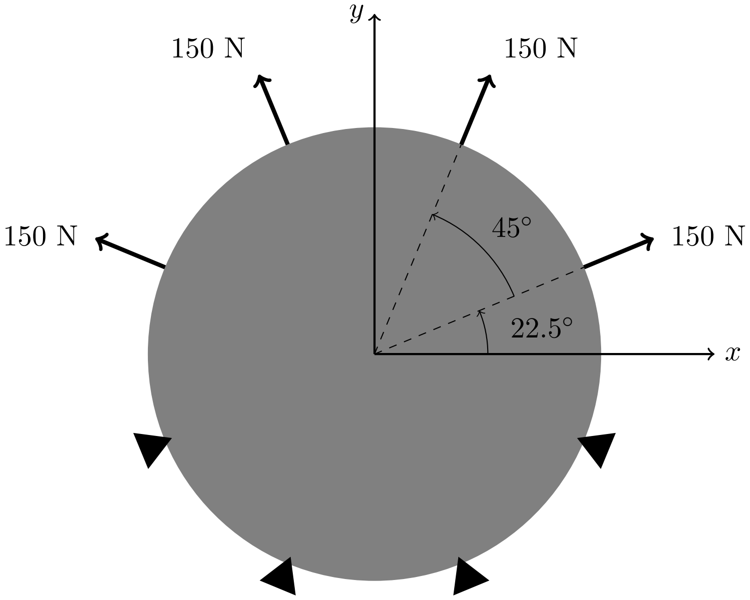

FIGURE 4.2: Schematic of model used for simulations.

4.4 Simulated Materials

A simulated heterogeneous material with four inclusions, regions of stiffness different from surrounding material, was created in a quasi-random process. Heterogeneities were assumed to be inclusions shaped as ellipses with a 2:1 ratio of major to minor axis. The 2:1 ratio was selected based on expected ratio in paper materials. Length of major axis of the ellipse was allowed to vary within a range so that the area of the heterogeneity was never larger than 8% of the total specimen area. Orientation of the ellipses was allowed to vary ±10°; location was allowed to vary with the requirement that the heterogeneities lay completely within the specimen with no overlapping heterogeneous regions. Orientation of the principal material direction was allowed to vary with respect to the surrounding material. Two additional materials were created by choosing a single inclusion from the first simulated material, either hard (stiff) or soft (compliant), but inclusion size was allowed to increase up to 8% maximum of total specimen area.

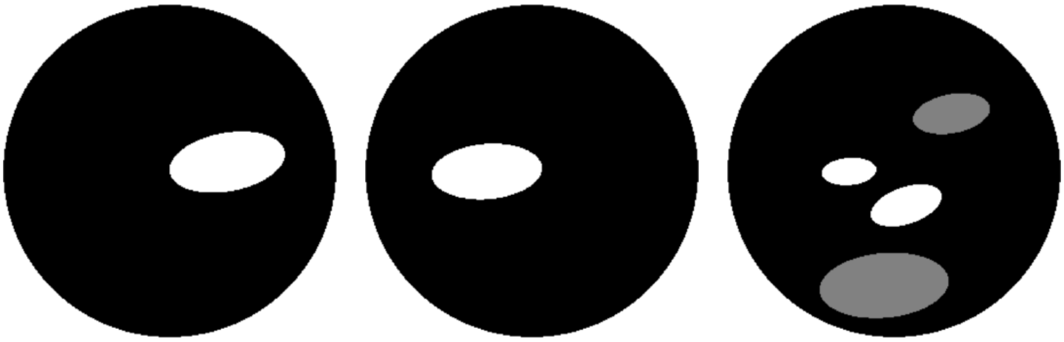

(a) Material 1 with a single soft inclusion.

(b) Material 2 with a single hard inclusion.

(c) Material 3 with two soft inclusions (gray) and two hard inclusions (white).

FIGURE 4.3: Simulated materials showing size and location of inclusions.

Figure 4.3 shows the materials with locations and sizes of inclusions used in this work. Material 1, Figure 4.3(a), represents a material with a soft inclusion; the inclusion had moduli E_{11}, E_{22}, and G_{12} set to 75% of those in the surrounding material, called the matrix. Poisson's Ratio, ν_{12}, was the same for both the inclusion and the matrix. Principal material direction for inclusion was rotated 11.66° to that of the matrix. Area of the inclusion was 6.20% of the total specimen area and the orientation of the inclusion was rotated 10.28° with respect to the global coordinate axes.

Material 2, Figure 4.3(b), represents a material with a hard inclusion; the inclusion had moduli E_{11}, E_{22}, and G_{12} set to 125% of those in the matrix. Poisson's Ratio, ν_{12}, was the same for both the inclusion and matrix. Principal material direction for inclusion was rotated -3.32° to that of the matrix. Area of the inclusion was 5.55% of the total specimen area and the orientation of the inclusion was rotated 4.55° with respect to the global coordinate axes.

Material 3, Figure 4.3(c), represents a material with soft and hard inclusions; both soft inclusions, denoted in gray, had the same moduli E_{11}, E_{22}, and G_{12} which were set to

70% of those in the matrix. Principal material directions for the soft inclusions were rotated 11.66° to that of the matrix. Both hard inclusions, denoted in white, had the same moduli E_{11}, E_{22}, and G_{12} which were set to 130% of those of the matrix. Principal material directions for the hard inclusions were rotated -3.32° to that of the matrix. Area of the smaller soft inclusion was 2.75% of the total area and the orientation of the inclusion was rotated 10.28° with respect to the global coordinate axes; the larger soft inclusion was 7.60% of the total area and the orientation of the inclusion was rotated 5.17° with respect to the global coordinate axes. Area of the smaller hard inclusion was 1.36% of the total area and the orientation of the inclusion was rotated 4.55° with respect to the global coordinate axes; the larger hard inclusion was 2.47% of the total area and the orientation of the inclusion was rotated 18.81° with respect to the global coordinate axes. Poisson's Ratio, ν_{12}, was the same for all inclusions and the matrix.

4.5 FEM analysis

A FEM model was created in ANSYS® using the PLANE82, 6-node triangular element, in plane stress. This element was chosen because it is well-suited to modeling curved boundaries of the specimen and inclusions. Mesh was freely-mapped; inclusions were initially meshed and then surrounding matrix material. Mesh density was high with over 108K elements for each of the materials in Figure 4.3 and was established with a mesh convergence study performed for fixture geometry validation.

Figures 4.4-4.6 show the results of the FEM analysis for each material, using the load configuration shown in Figure 4.2. Inclusions were hardly noticeable in displacement contour plots, but were evident on strain contour plots.

The strain contours showed significant gradients, especially near the grip locations. Each material had small ε_1 and ε_6 over a large portion of the specimen. Because of these small strains parameter identification was greatly influenced by the grip regions.

4.6 Numerical implementation of VFM for heterogeneous materials

Numerical implementation was performed in Matlab® and was based on analysis in Chapter 3 for homogeneous materials. Extension of that analysis for a single inclusion,

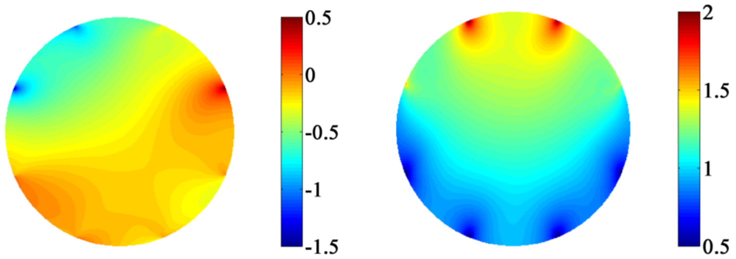

(a) u, units (mm).

(b) v, units (mm).

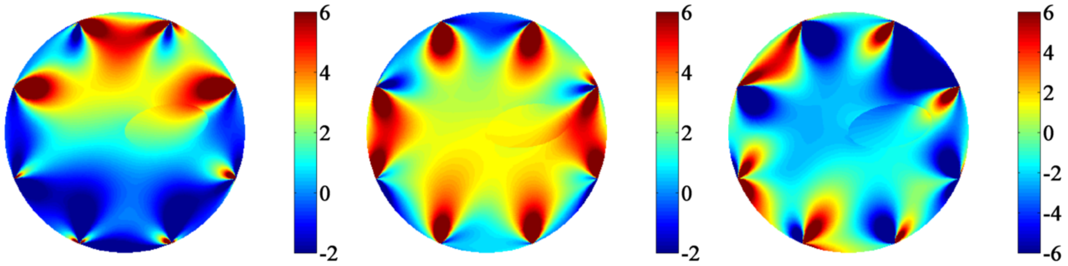

(c) ε_1, units (mm/m).

(d) ε_2, units (mm/m).

(e) ε_6, units (mm/m).

FIGURE 4.4: FEM displacements and strains for Material 1.

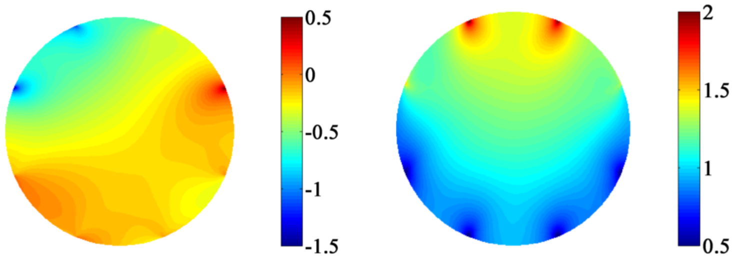

(a) u, units (mm).

(b) v, units (mm).

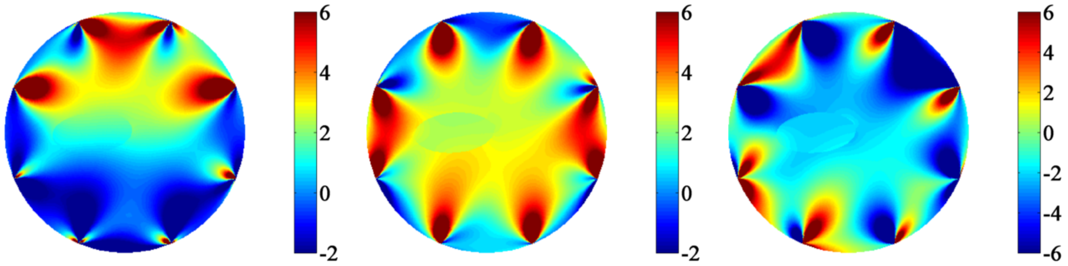

(c) ε_1, units (mm/m).

(d) ε_2, units (mm/m).

(e) ε_6, units (mm/m).

FIGURE 4.5: FEM displacements and strains for Material 2.

Equation 4.2 required 12 special, optimized virtual fields for the 6 Q_{ij} of the matrix and the 6 Q_{ij} of the inclusion. Similarly, modifications of $\mathbf{G}$ (Equation 3.5), the noise optimization matrix, were made for the inclusions.

Polynomial formulation for Q_{ij} used a fourth order polynomial, $n = 4$ unless otherwise

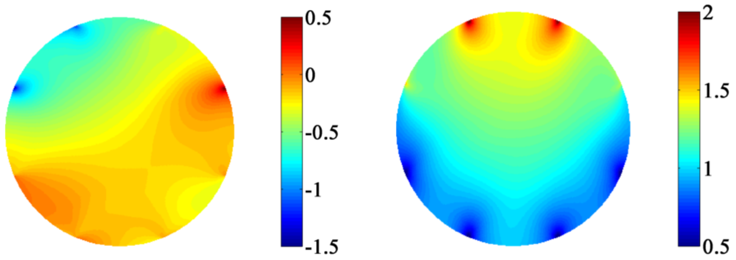

(a) u, units (mm).

(b) v, units (mm).

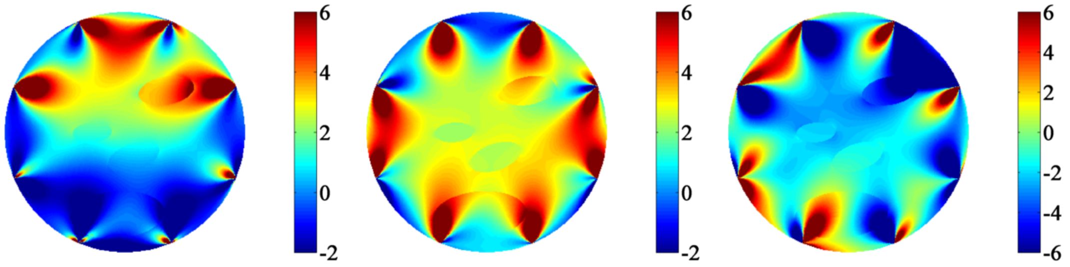

(c) ε_1, units (mm/m).

(d) ε_2, units (mm/m).

(e) ε_6, units (mm/m).

FIGURE 4.6: FEM displacements and strains for Material 3.

specified, and required the identification of 150 α's, $((n+1)^2 \cdot 6)$ and, therefore, 150 special, optimized virtual fields. Limit of order of the polynomial must be examined on a case-by-case basis. For these simulations the identification started to become unstable at $n = 6$, but other simulations, used for preliminary work and not included here, were stable up to $n = 8$. Here, the polynomial formulation was intended to show the existence of heterogeneities and a high polynomial order adds little information.

The EG analysis was performed by using the same analysis used in Chapter 3, i.e. assume the material is homogeneous and determine Q_{ij}. Those Q_{ij} were then used in the EG analysis as described in Section 4.2.3. When the sliding window covers the boundary of the specimen the EG analysis believes a gap in equilibrium exists. Those results were set to equilibrium, i.e. 0.

4.7 VFM Mesh density determination

The objectives for this portion of the work were to demonstrate the systematic error of the simulation and to determine an appropriate VFM mesh density for subsequent simulations. The systematic error consists of combined errors of the FEM analysis, discrete summation of the integrals in Equation 4.2, numerical errors associated with operations, including interpolation and optimization, in Matlab®.

While not required in practice, it was desirable to use the same virtual mesh element for each of the analyses here in order to reduce simulation variables. Effect of different mesh densities were examined, from 49 total VF elements to 400 total VF elements, on accuracy of Q_{ij} identification. For this analysis no noise was added to the FEM strains, i.e. the FEM strain were used directly in Equation 4.2 for parameter identification.

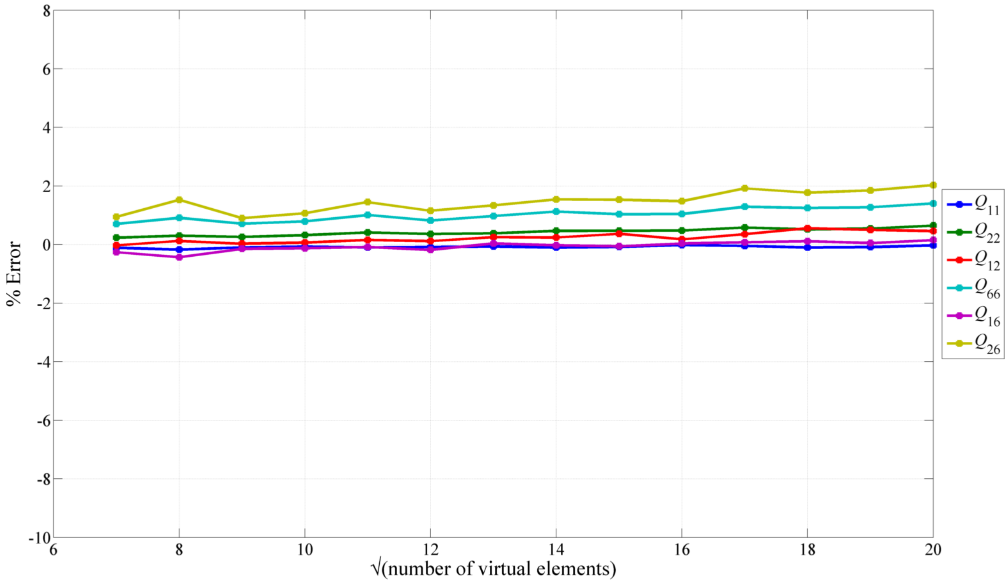

(a) Matrix Q_{ij} identification.

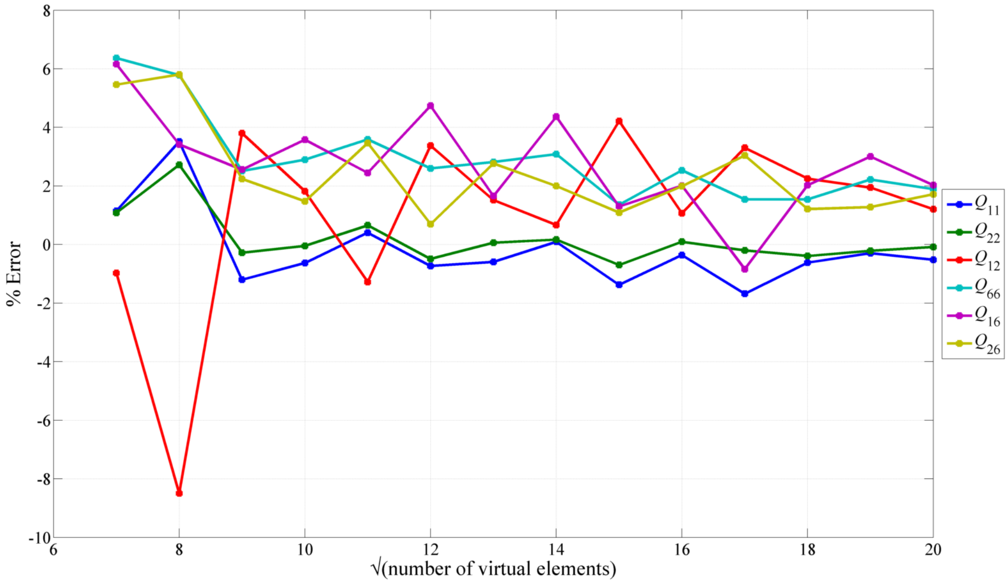

(b) Inclusion Q_{ij} identification.

FIGURE 4.7: Effect of VF mesh density on error of Q_{ij} identification for Material 1.

Figure 4.7 shows small, but increasing error for matrix Q_{ij} identification in Material 1. As the mesh density increased, the conditioning of the optimization matrix degraded because additional virtual node displacements were determined that were not necessary for the solution. Inclusion Q_{ij} identification had larger error but error stabilized after 9^2 elements because fewer elements did not provide sufficient degrees of freedom for identification.

For Material 1, using 15^2 virtual elements, the systematic error was about 1% or less for Q_{11} and Q_{22} in both the matrix and inclusion. Errors for the other Q_{ij} were slightly higher, but quite low for the matrix.

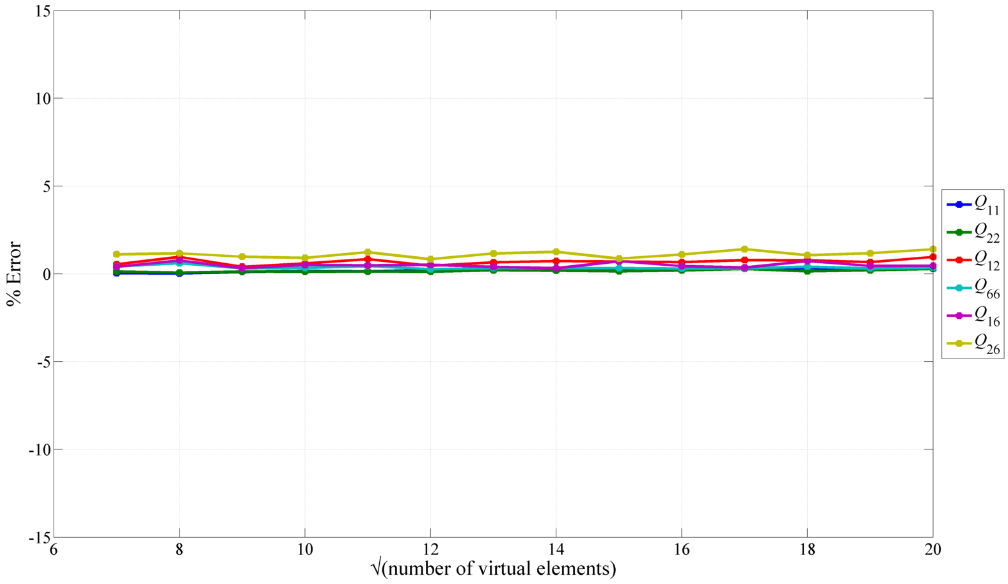

(a) Matrix Q_{ij} identification.

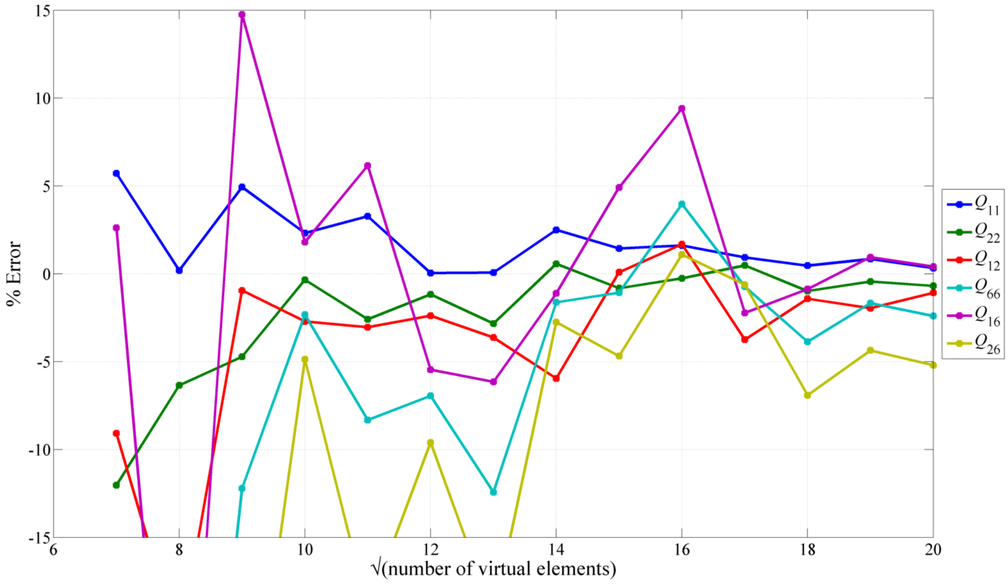

(b) Inclusion Q_{ij} identification.

FIGURE 4.8: Effect of VF mesh density on error of Q_{ij} identification for Material 2

Figure 4.8 shows small errors for Material 2 matrix Q_{ij} identification, similar to Material 1, which increased with mesh density. The y-scale for inclusion Q_{ij} error was reduced to better show the error greater mesh density. For Material 2 inclusion identification did not stabilize until 14^2 elements. Identification error for the hard inclusion in Material 2 was larger than for the soft inclusion in Material 1. The primary factor creating identification error was due to less strain in the inclusion as seen in Figure 4.5.

In particular, ε_6 was smaller in the hard inclusion than surrounding matrix which created the large identification errors for Q_{66}, Q_{16}, Q_{26}. Another contributing factor was that the hard inclusion in Material 2 was smaller than the soft inclusion in Material 1. Both factors combined to reduce the magnitude and quantity of the strain data. While the identification error in the inclusion is high, the errors associated with 15^2 elements are less than 3% for Q_{11}, Q_{22}, Q_{12} and Q_{66}.

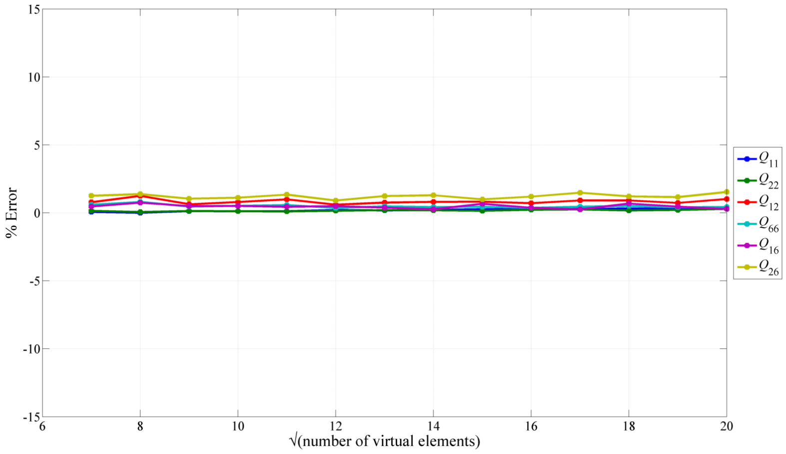

(a) Matrix Q_{ij} identification.

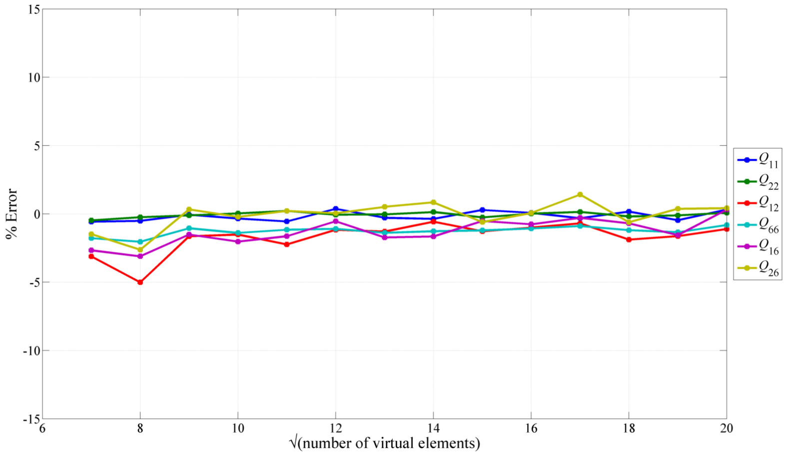

(b) Soft inclusions: Q_{ij} identification.

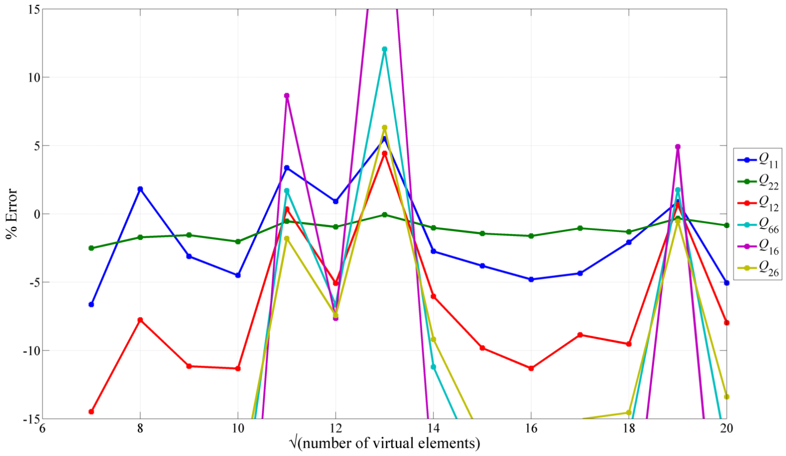

(c) Hard inclusions: Q_{ij} identification.

FIGURE 4.9: Effect of VF mesh density on error of Q_{ij} identification for Material 3.

Figure 4.9 shows identification error for Material 3 which had two soft and two hard inclusions. Material 3 had good identification at all mesh densities for the matrix and soft inclusions. But, like the hard inclusion in Material 2, the hard inclusion in Material 3 required a slightly greater mesh density, up to 14^2 elements, before identification error became stable. The physical separation of the soft inclusions did not adversely affect identification, in fact, the greater proportional area of the soft inclusions in Material 3 as compared to the single soft inclusion in Material 1 tended to improve inclusion parameter identification, as seen in Figures 4.7(b) and 4.9(b).

Systematic identification error for Material 3 was less than 5% for the matrix and soft inclusions and for Q_{11} and Q_{22} in the hard inclusions. Error for Q_{12} in the hard inclusion was slightly higher. Inability to accurately identify those stiffnesses associated with shear, Q_{66}, Q_{16} and Q_{26}, is related to several factors, including specific load condition, location and size of inclusions and simulation parameters. For paper materials, large stiffness gradients are unlikely to occur; a more gradual gradient is expected.

Based on error analysis the 225 element (15^2) virtual element mesh shown in Figure 4.10 was used for all subsequent analyses. This mesh does not have uniform element size. The outer boundary of elements had larger aspect ratios to accommodate grip and force application nodes. Most interior elements are square except for those which have a boundary colinear with a grip or force application nodes.

Elements completely outside the specimen boundary (blue circular line) do not contribute to parameter identification. Those elements which straddle the specimen boundary only have a contribution for the portion inside the boundary. Nodes outside the boundary had no displacements conditions specified.

4.8 Simulation of experimental data

In order to simulate experiment strain data, different levels of noise were added to the FE strains shown in Figures 4.4-4.6. Random Gaussian noise with zero mean value was added to strain data at ten different, equally-spaced, standard deviations with the largest standard deviation as 0.9 mm/m. This maximum noise level was large compared to the calculated FE strains and represented three times the standard deviation of the DIC strain determined from two consecutively captured no-load specimens from earlier work. A single standard deviation, 0.3 mm/m strain, represents resolution of the DIC system and is specific to DIC pattern, lighting, cameras and their settings, and DIC analysis

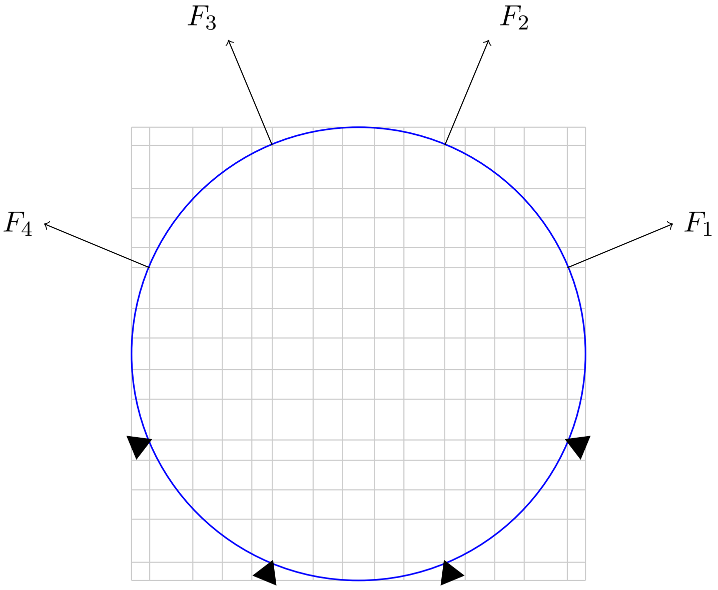

FIGURE 4.10: Virtual element mesh used; 225 elements.

including any data smoothing. Ten randomizations of noise addition were performed for each noise level. Figure 4.11 shows an example random strain noise addition to Material 1, where the strain noise was the largest possible, i.e. 0.9 mm/m. At this noise level the soft inclusion was obscured in the strain maps, Figures 4.11(d) and 4.11(e).

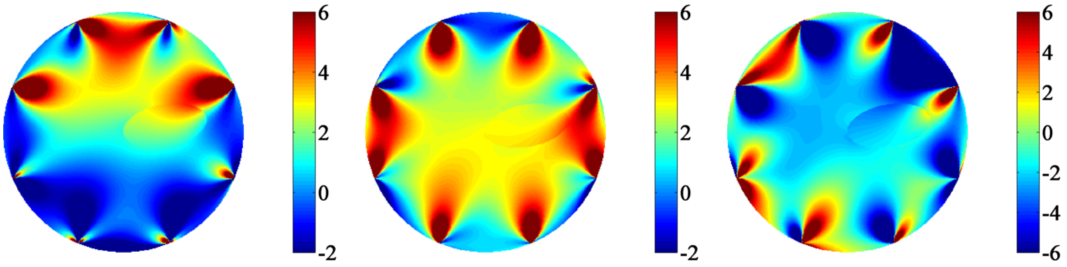

(a) FEM ε_1, units (mm/m).
(b) FEM ε_2, units (mm/m).
(c) FEM ε_6, units (mm/m).

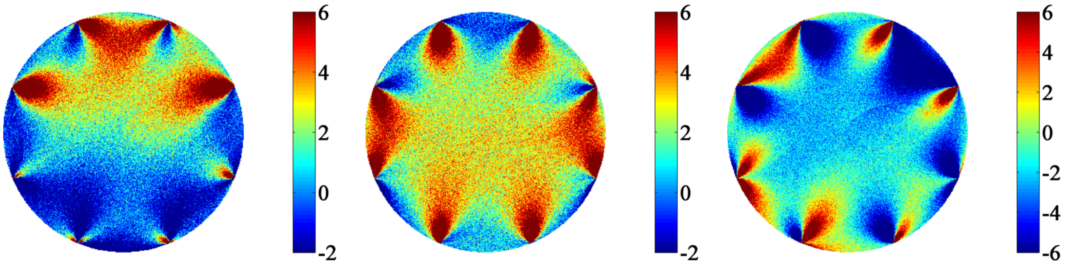

(d) Noisy ε_1, units (mm/m).
(e) Noisy ε_2, units (mm/m).
(f) Noisy ε_6, units (mm/m).

FIGURE 4.11: FEM strains for Material 1 with no noise (top row) and with noise addition (bottom row).

4.8.1 Inclusion location and geometry known

Given the location and geometry of inclusion or inclusions Equation 4.2, or modified version to include an additional region S_3, was used for parameter identification. One hundred simulations were performed (10 noise levels x 10 randomizations of white noise for each noise level) for each material.

TABLE 4.1: Comparison of identified Q_{ij} for Material 1 when inclusion location is known. Units for Q_{ij} are km^2/s^2

		Q_{11}	Q_{22}	Q_{12}	Q_{66}	Q_{16}	Q_{26}
Matrix	Reference	3.49	3.49	0.95	1.35	0.64	0.64
	Mean VFM	3.49	3.51	0.95	1.36	0.64	0.65
	Error(%)	-0.10	0.46	0.38	1.04	-0.06	1.51
	COV (%)	0.01	0.02	0.05	0.02	0.04	0.03
Inclusion	Reference	2.24	3.01	0.70	1.00	0.42	0.46
	Mean VFM	2.21	2.99	0.73	1.01	0.43	0.47
	Error(%)	-1.39	-0.73	4.12	1.35	1.39	0.93
	COV(%)	0.24	0.23	1.02	0.59	0.60	0.42

Table 4.1 shows identification results for Material 1. Reference values denote those used in FEM modeling. Mean VFM are the mean of the identifications of the 100 simulations. Error shows % difference between Reference and Mean VFM identifications and is the accuracy of the method. This accuracy does not include errors caused by interpolation, smoothing and other data manipulations, such as coordinate transformation. Similarly, COV gives the coefficient of the variation of the 100 simulations and is the resolution of the method.

The errors associated with Material 1 Q_{ij} identification were less than 2%, except for inclusion Q_{12}, which is the most difficult stiffness to identify using full field techniques. Even so, the identification error for inclusion Q_{12} was only 4%. Q_{12} was also difficult to identify in Chapter 3. The low COV's suggest the analysis was quite stable and was able to find the special, optimized virtual fields reliably.

An orthotropic inclusion with a different orientation of material principal properties with respect to an orthotropic matrix will produce an 'homogenized' anisotropic material, i.e. if the material is assumed to be homogeneous, as in Chapter 3, the stiffness identification will show the material is anisotropic. Table 4.1 shows that if the inclusion location and geometry are known the analysis can separately determine the orthotropic stiffnesses of the matrix and inclusion.

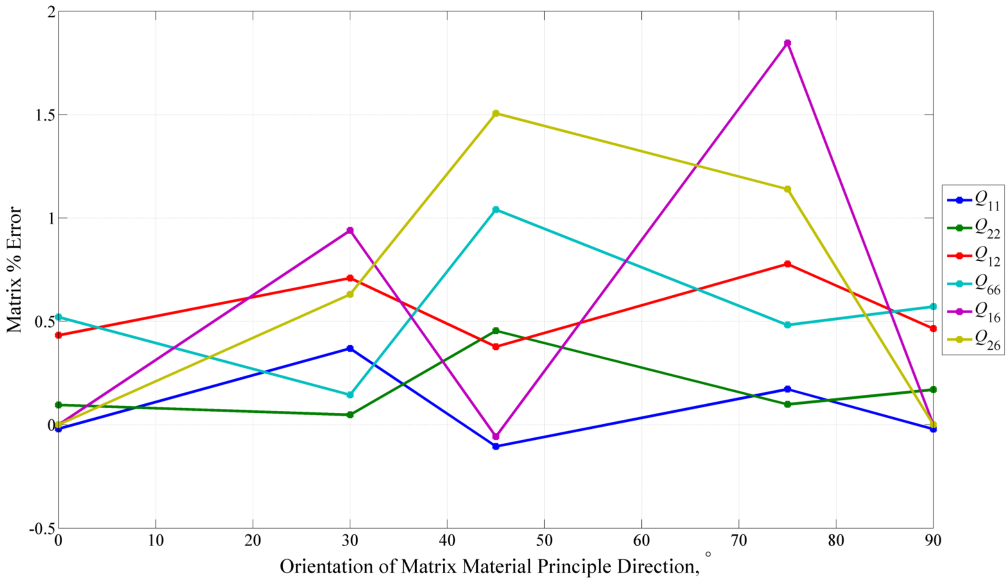

(a) Matrix identification error.

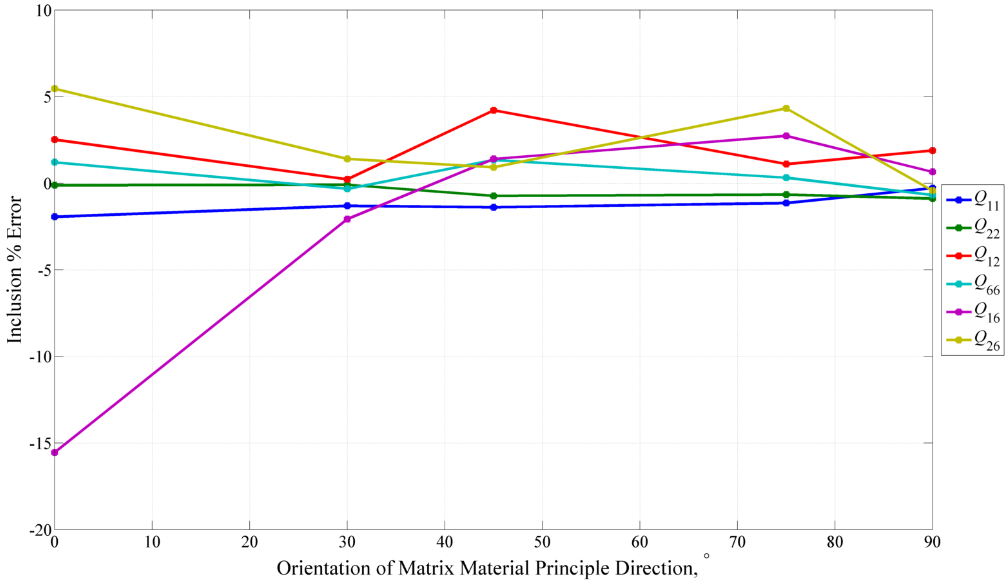

(b) Inclusion identification error.

FIGURE 4.12: Effect of orientation of material principal directions on Q_{ij} identification for Material 1.

Orientation of material principal axes within the specimens does have a small effect on parameter identification. For Table 4.1 orientation of matrix material principal direction was 45° and orientation of the inclusion principal material direction was 56.66°. Figure 4.12 shows identification error for matrix and inclusion of Material 1 for different orientations of matrix material principal direction. Location and size of the inclusion were not changed; material principal direction of the inclusion was kept at +11.66° with respect to the matrix properties. Matrix reference values for Q_{16} and Q_{26} are zero at 0° and 90° and their errors were set to 0 in Figure 4.12(a) even though small values were identified. Matrix identification error was small for all orientations; inclusion identification error was smallest for 30° but was 5% error or less for orientations above 0°. The consistently small error regardless of material property principal directions indicates a level of robustness in the identification method.

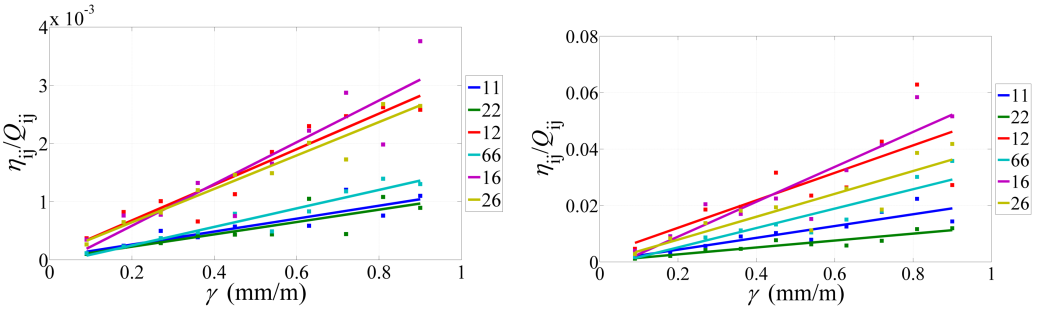

(a) Effect of strain noise on matrix COV(Q_{ij}). (b) Effect of strain noise on inclusion COV(Q_{ij}).

FIGURE 4.13: Effect of strain noise on COV(Q_{ij}) for Material 1.

Figure 4.13 shows the COV (η_{ij}/Q_{ij}) for each stiffness as related to added strain noise for Material 1. The lines represent a linear correlation of the points for each respective stiffness; symbols represent the mean value of the 10 simulations at each noise level. Magnitude of line slope indicates the relative effect of noise on identification. The matrix Q_{16}, Figure 4.13(a), was more affected by noise than the other stiffnesses; Q_{22} was least affected by noise. Accurate identification of Q_{22} was also observed in the previous chapter and was attributed to loading geometry. For the inclusion, relative order of influence of noise on identification was the same as the matrix, though the effect of noise was much larger on inclusion identification. Somewhat surprisingly, identification of Q_{12} was more affected by noise than Q_{26} for both the matrix and inclusion. Determination of Poisson's effect is challenging in many configurations [1].

Identification results for Material 2 are shown in Table 4.2. Matrix identification was similar to Material 1 will small errors and COVs for all Q_{ij}. Inclusion identification had larger errors and higher COVs. Increased difficulty in identification of inclusion Q_{ij} was not surprising considering the small strain gradients in the inclusion shown in Figures 4.5(c)-4.5(e). Location of the hard inclusion within the matrix greatly reduced the effects of external forces. Strains, especially ε_6, transmitted by the matrix material to the inclusion were damped within the inclusion. Consequently, identification of Q_{66}, Q_{16}, and Q_{26} were adversely affected.

Table 4.2: Comparison of identified Q_{ij} for Material 2 when inclusion location is known. Units for Q_{ij} are km^2/s^2

		Q_{11}	Q_{22}	Q_{12}	Q_{66}	Q_{16}	Q_{26}
Matrix	Reference	3.49	3.49	0.95	1.35	0.64	0.64
	Mean VFM	3.50	3.50	0.96	1.35	0.65	0.65
	Error(%)	0.29	0.15	0.71	0.33	0.71	0.87
	COV (%)	0.02	0.01	0.06	0.02	0.05	0.05
Inclusion	Reference	4.55	4.18	1.19	1.68	0.81	0.79
	Mean VFM	4.59	4.13	1.20	1.66	0.85	0.74
	Error(%)	0.94	-1.14	1.28	-1.51	5.23	-5.75
	COV(%)	0.58	0.76	1.31	3.20	3.53	4.07

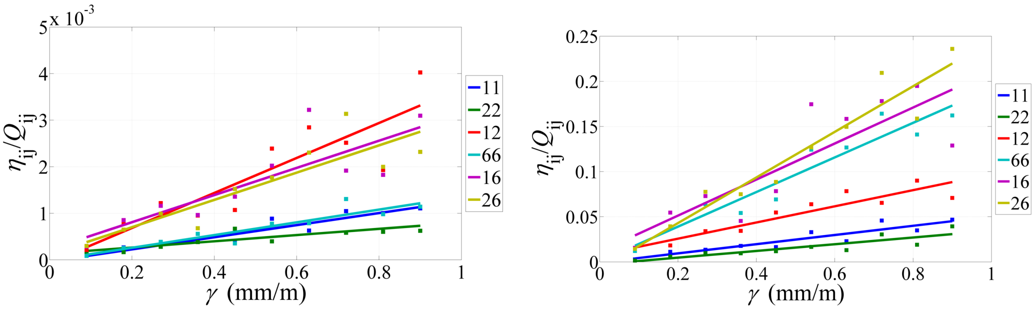

(a) Effect of strain noise on matrix COV(Q_{ij}). (b) Effect of strain noise on inclusion COV(Q_{ij}).

Figure 4.14: Effect of strain noise on COV(Q_{ij}) for Material 2.

Figure 4.14 shows the COV (η_{ij}/Q_{ij}) for each stiffness as related to added strain noise for Material 2. Since the matrix material had similar area for Materials 1 and 2 it is instructive to compare matrix identification for these materials in Figures 4.13(a) and 4.14(a). The y-axis in these figures is similar for both materials, except for Q_{12} of Material 2 which was more affected by noise. Identification for Material 2 matrix Q_{11} was more affected by noise than for Material 1. This effect seems to be caused by the reduced strain in the matrix caused by the hard inclusion. Figure 4.14(b) shows the difficulty in identification of stiffnesses associated with shear strain, namely Q_{66}, Q_{16}, and Q_{26}. Note that error of inclusion Q_{ij} scaled with their respective COVs in Table 4.2.

Identification results for Material 3 are shown in Table 4.3. The VFM analysis underestimated the soft inclusion Q_{ij}, except for Q_{11}. Figure 4.9(b) shows the identification was stable with respect to mesh density. Hard inclusion identification error for Material 3 was large, but it is important to note that COV's were smaller than errors. In this case, resolution of this analysis was greater than the accuracy. This result is encouraging because some of the error can be attributed to FEM analysis, discrete summation, noise

Table 4.3: Comparison of identified Q_{ij} for Material 3 when inclusion locations are known. Units for Q_{ij} are km^2/s^2

		Q_{11}	Q_{22}	Q_{12}	Q_{66}	Q_{16}	Q_{26}
Matrix	Reference	3.49	3.49	0.95	1.35	0.64	0.64
	Mean VFM	3.50	3.50	0.96	1.35	0.65	0.65
	Error(%)	0.27	0.14	0.79	0.42	0.63	0.95
	COV (%)	0.01	0.03	0.07	0.02	0.06	0.04
Soft Inclusions	Reference	2.09	2.81	0.66	0.93	0.39	0.43
	Mean VFM	2.10	2.80	0.65	0.92	0.39	0.43
	Error(%)	0.29	-0.30	-1.45	-1.20	-0.64	-0.69
	COV(%)	0.17	0.08	0.25	0.11	0.40	0.36
Hard Inclusions	Reference	4.73	4.34	1.23	1.75	0.84	0.82
	Mean VFM	4.50	4.27	1.09	1.33	0.51	0.65
	Error(%)	-4.93	-1.79	-11.58	-23.73	-39.79	-20.22
	COV(%)	2.62	0.27	2.55	8.36	20.45	5.28

optimization and selected VFM mesh. Figure 4.9(c) shows that a 14^2 mesh would likely have produced smaller errors.

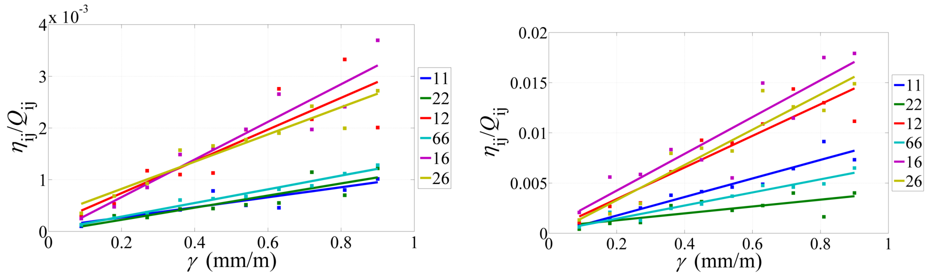

(a) Effect of strain noise on matrix COV(Q_{ij}). (b) Effect of strain noise on soft inclusions COV(Q_{ij}).

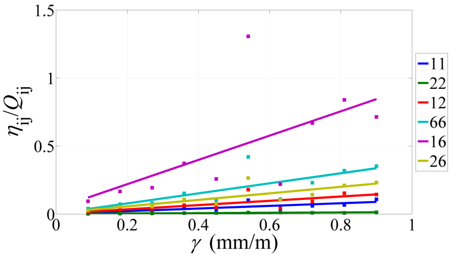

(c) Effect of strain noise on hard inclusions COV(Q_{ij}).

Figure 4.15: Effect of strain noise on COV(Q_{ij}) for Material 3.

Figure 4.15 shows the COV (η_{ij}/Q_{ij}) for each stiffness as related to added strain noise for Material 3. Notice the large disparity in y-scale in each figure which indicates the relative difficulty in parameter identification; the matrix was least affected by strain noise and the hard inclusions were most affected by strain noise. The relative difficulty of stiffness identification was similar for the matrix and soft inclusions in that the order of colors was similar. However, for the hard inclusion the shear-related stiffnesses were more affected by strain noise than the other parameters.

4.8.2 Spatial variability of Q_{ij}

In order to simulate experimental data, the FE strains shown in Figures 4.4-4.6 were interpolated to a grid, 300x300 points, meant to represent the output of DIC (digital image correlation) analysis using the Matlab® function *TriScatteredInterp*. The grid spacing was larger than any element in the FEM model; the grid had a total of 90K points and the FEM model had 108K+ elements, but the elements were completely within the specimen boundary. Approximately 19K grid points, of the 90K total, laid outside the specimen boundary. Grid size was chosen to approximate window size in the DIC analysis in Chapter 3. Random Gaussian white noise with zero mean value was added to gridded strain data at ten different, equally-spaced, levels with the largest level as 0.9 mm/m. This maximum noise level was large compared to the calculated FE strains and represented three times the standard deviation of the DIC strain determined from two consecutively captured no-load specimens from earlier work. Ten randomizations of noise addition were performed for each noise level. A fourth order polynomial was used to examine the ability of a smoothly varying function to perform parameter identification. Total number of parameters fit was 150 (25 parameters for 6 Q_{ij}) and, therefore, 150 special optimized virtual fields were required.

Figure 4.16 shows the contour maps for each Q_{ij} for Material 1. Mappings show large gradients, narrow color contours, near and around the soft inclusion. Mappings were created by averaging 100 α_{ij}^{kl} (10 strain noise levels x 10 randomizations/noise level). Figure 4.17 shows contour maps of the ratio of $Q_{ij}/Q_{ij}^{\text{FEM}}$. Green contours indicate that identified Q_{ij} agreed with Q_{ij}^{FEM}, i.e. their ratio = 1.

The polynomial mapping of Q_{ij} for Material 1 gave a general indication of size and location of the soft inclusion. Viewing Figure 4.16 without prior knowledge of the inclusion an analyst would infer an inclusion existed and further analysis was warranted. Figures 4.16(a) and 4.16(c) seemed to show the presence of the inclusion more dramatically than other Q_{ij}.

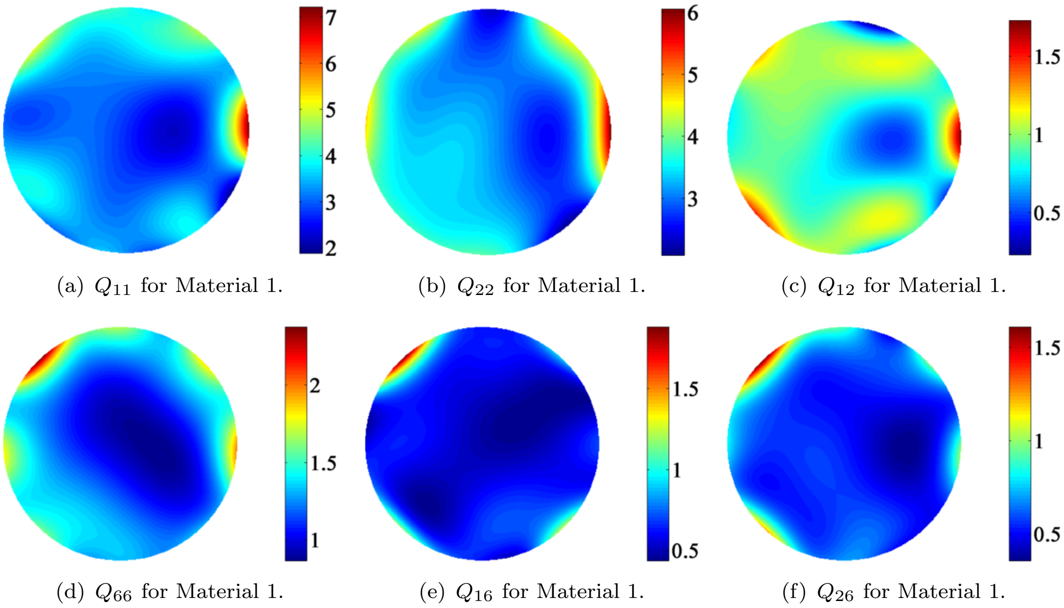

(a) Q_{11} for Material 1. (b) Q_{22} for Material 1. (c) Q_{12} for Material 1.

(d) Q_{66} for Material 1. (e) Q_{16} for Material 1. (f) Q_{26} for Material 1.

FIGURE 4.16: Fourth order polynomial Q_{ij} contour maps for Material 1, units km^2/s^2.

Figure 4.18 shows the contour maps for each Q_{ij} for Material 2. These maps do not provide clear indication of the hard inclusion geometry and location. However, the maps still have unusual contours that suggest presence of some foreign material.

Figure 4.19 shows contour maps of the ratio of $Q_{ij}/Q_{ij}^{\text{FEM}}$. The light blue color within the inclusion location shows the polynomial formulation underestimated the inclusion stiffnesses. As stated in the previous section with regard Material 2, identification of the hard inclusion was made more difficult because the interior of the hard inclusion showed less strain than the matrix material adjacent to the inclusion and its strain gradients were small.

Figure 4.20 shows the contour maps for each Q_{ij} for Material 3. Presence of inclusions are not apparent in these maps, but large gradients in the maps for Q_{11} and Q_{66} suggest that analysis with a higher order polynomial should be considered. Since Figure 4.20(d) contains a large, interior region where $Q_{66} < 0$, which is physically impossible, the 4^{th} order polynomial was unable to provide reasonable identification.

Figure 4.21 shows contour maps of the ratio of $Q_{ij}/Q_{ij}^{\text{FEM}}$ for Material 3. While none of the inclusions had good stiffness identification, the best inclusion identification was for the large soft inclusion near bottom of specimen. Large portion of blue for Figures 4.21(c)-4.21(f) indicate large underestimation of those stiffnesses. Gradients were

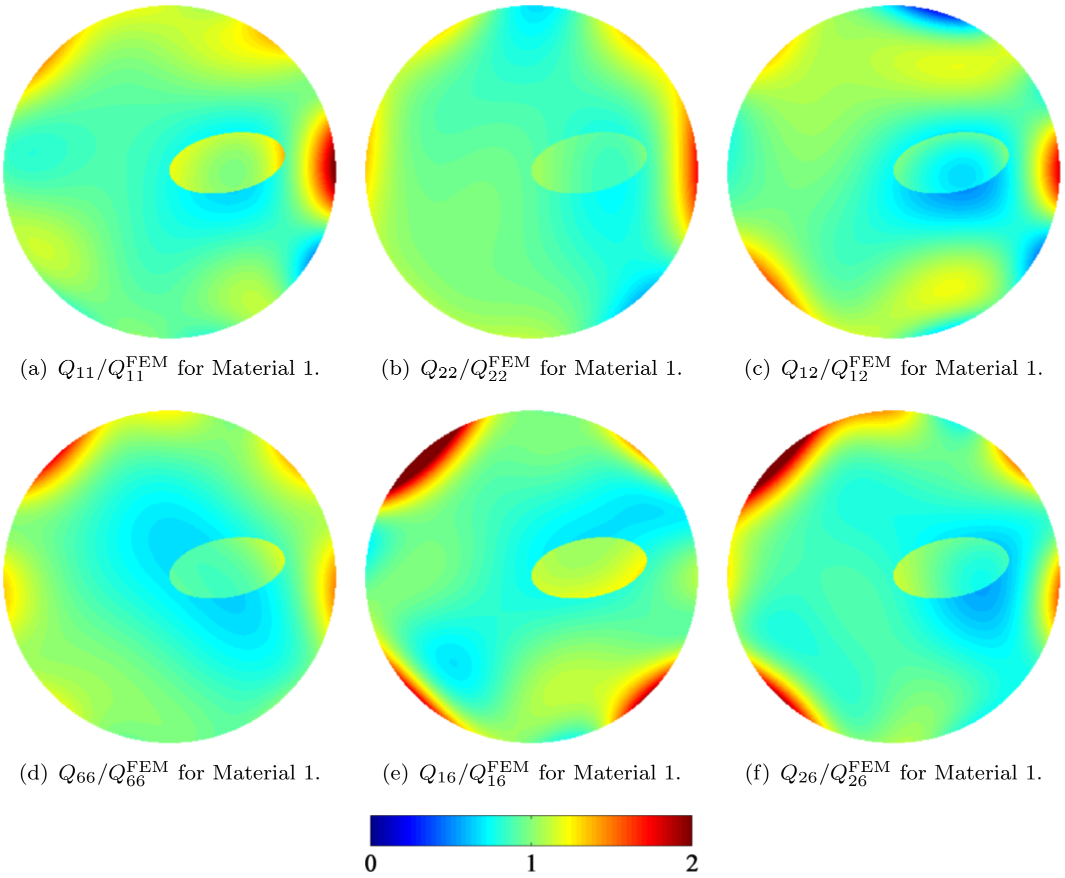
(a) $Q_{11}/Q_{11}^{\mathrm{FEM}}$ for Material 1.
(b) $Q_{22}/Q_{22}^{\mathrm{FEM}}$ for Material 1.
(c) $Q_{12}/Q_{12}^{\mathrm{FEM}}$ for Material 1.
(d) $Q_{66}/Q_{66}^{\mathrm{FEM}}$ for Material 1.
(e) $Q_{16}/Q_{16}^{\mathrm{FEM}}$ for Material 1.
(f) $Q_{26}/Q_{26}^{\mathrm{FEM}}$ for Material 1.

FIGURE 4.17: Ratio of Q_{ij} contour maps for Material 1 using 4th order polynomial.

smallest for Q_{22}; Q_{22} is the consistently best identified stiffness given loading configuration.

For Material 3 only a 5th order polynomial was used for Q_{ij}. The Q_{ij} contours are shown in Figures 4.22 and 4.23. As expected, increasing the spatial frequency for stiffness did not improve stiffness mapping. Errors were greater for all stiffnesses as seen when comparing Figure 4.21, the 4th order polynomial representation, to Figure 4.23, the 5th order polynomial representation. The 5th order polynomial consistently underestimated stiffnesses.

4.8.3 Equilibrium Gap

Materials were assumed to be homogeneous and VFM Q_{ij} identification was performed as in Chapter 3. The Equilibrium Gap analysis was performed with two window sizes. Figure 4.24 shows the EG analysis for each material at two window sizes, 2x2 and 5x5.

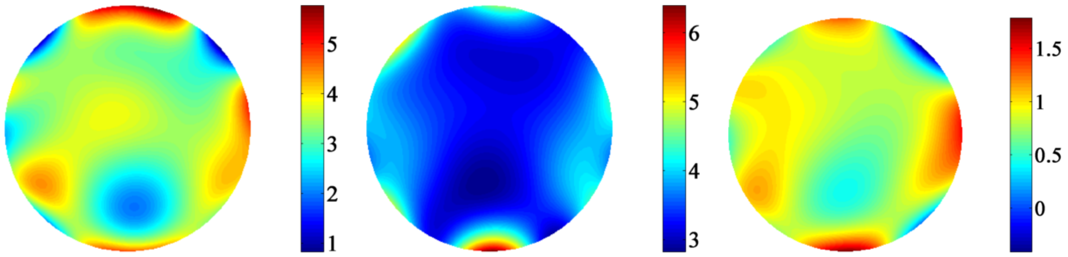

(a) Q_{11} for Material 2. (b) Q_{22} for Material 2. (c) Q_{12} for Material 2.

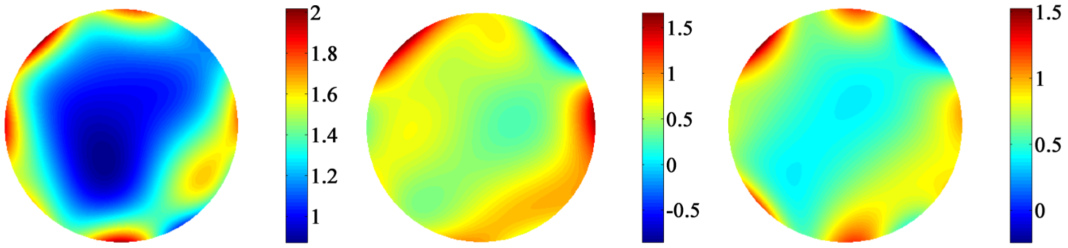

(d) Q_{66} for Material 2. (e) Q_{16} for Material 2. (f) Q_{26} for Material 2.

FIGURE 4.18: Fourth order polynomial Q_{ij} contour maps for Material 2, units km^2/s^2.

Figures 4.24(g)-4.24(i) show EG contours with addition of 0.3 mm/m of strain noise. A smaller strain noise was added here because this is the expected noise, as determined in Chapter 3.

Without added noise, Figures 4.24(a)-4.24(f), EG maps were able to locate inclusion boundaries. The large soft inclusion of Material 3, Figures 4.24(c) and 4.24(f), showed some non-equilibrium within the inclusion due to mismatch in Poisson's Ratio between the homogeneous VFM estimate and the actual Poisson's Ratio in the inclusion.

Inclusion boundary colors are related to the direction of rastering during the EG calculation. If rastering direction was reversed the colors would reverse. The large regions of green denote local equilibrium, but does not indicate accurate Q_{ij} identification. The EG formulation given in Equation 4.5 will give the same EG mapping, though at a different scale, independent of any Q_{ij}. If the EG window covers a region comprising only a single material the EG contour will show the region is in equilibrium regardless of Q_{ij} choice, because these terms cancel each other. For example, virtual displacement of node 5 in Figure 4.1 creates virtual tensile strain, ε_1^*, in two elements and exactly equal, but opposite, compressive strain in the other two elements. Regardless of any choice for Q_{11}, the integral term associated with $\varepsilon_1 \varepsilon_1^*$ is zero when the window covers a homogeneous portion of the specimen. Similar explanations can be made for each term in Equation 4.5.

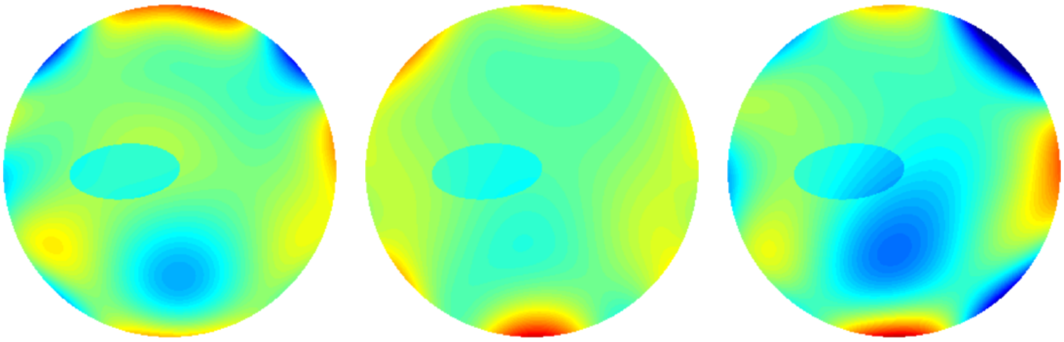

(a) $Q_{11}/Q_{11}^{\text{FEM}}$ for Material 2. (b) $Q_{22}/Q_{22}^{\text{FEM}}$ for Material 2. (c) $Q_{12}/Q_{12}^{\text{FEM}}$ for Material 2.

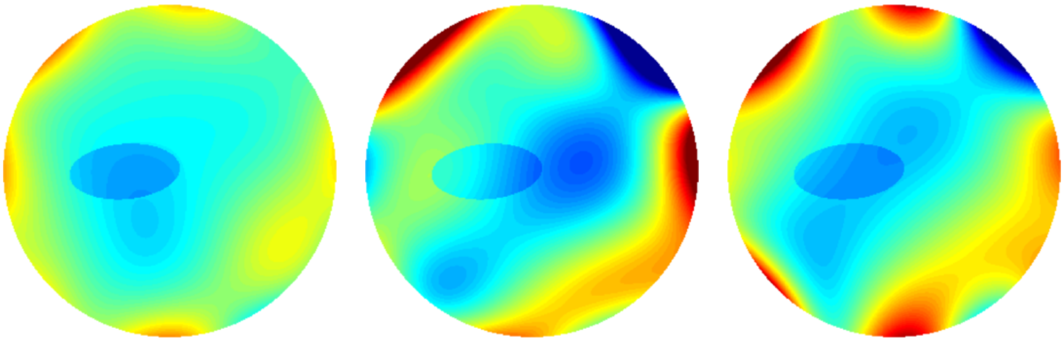

(d) $Q_{66}/Q_{66}^{\text{FEM}}$ for Material 2. (e) $Q_{16}/Q_{16}^{\text{FEM}}$ for Material 2. (f) $Q_{26}/Q_{26}^{\text{FEM}}$ for Material 2.

FIGURE 4.19: Ratio of Q_{ij} contour maps for Material 2 using 4th order polynomial.

Added strain noise, Figures 4.24(g)-4.24(i), tended to obscure inclusion boundaries. More importantly, the added strain noise was sufficient to indicate areas of non-equilibrium throughout the materials, indicated by small regions of yellow and blue. Inclusion boundaries are broken and the bottom of each material shows non-equilibrium similar to the magnitude of inclusion boundaries. Unfortunately, stronger data smoothing erodes Q_{ij} identification, particularly Q_{12}.

4.9 Discussion

Systematic error was examined by direct use of FE strains in the VFM identification procedure without addition of any artificial strain noise and was shown in Figures 4.7-4.9. Error associated with matrix parameter identification was less than 3% for each material. Inclusion identification had greater error, around 5% for the soft inclusions and 10% or more for the hard inclusions. These errors are reasonable considering that the

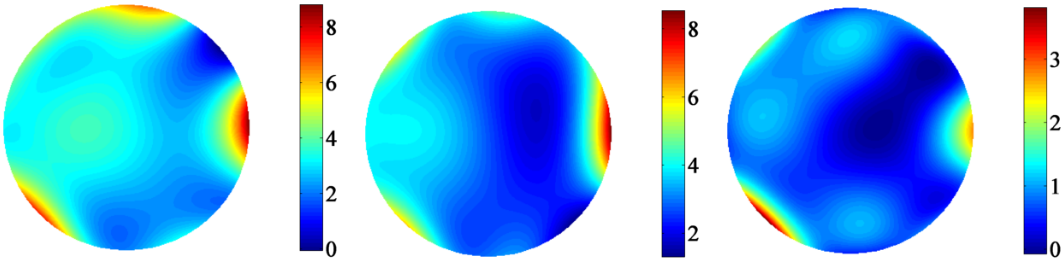

(a) Q_{11} for Material 3. (b) Q_{22} for Material 3. (c) Q_{12} for Material 3.

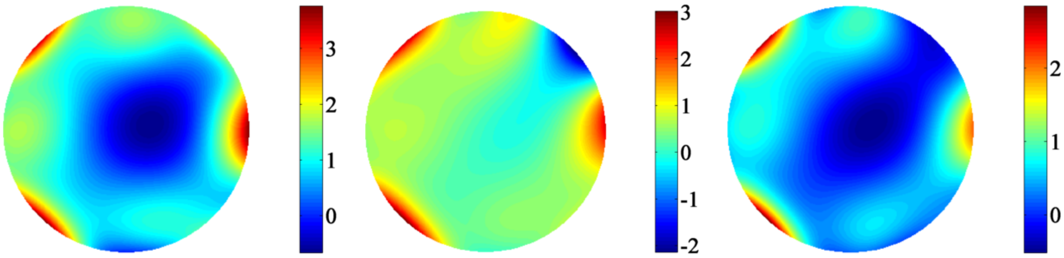

(d) Q_{66} for Material 3. (e) Q_{16} for Material 3. (f) Q_{26} for Material 3.

FIGURE 4.20: Fourth order polynomial Q_{ij} contour maps for Material 3, units km^2/s^2.

only mesh variable adjusted was density. Iterative meshing which would create greater VF node density with inclusions would further reduce systematic error.

When inclusion location and geometry are known the accuracy and resolution of VFM parameter identification is good, as shown in Tables 4.1-4.3. Even with errors associated with FEM analysis, discretization of integrals and noise optimization, the VFM analysis produced results which allow discrimination between matrix and inclusion properties. Users of this technique will be able to determine the contribution to errors from physical properties (location, geometry) and mechanical properties. Analysis of Material 3 provides an additional challenge for the material scientist, namely that they can have confidence that two (or more) inclusions have the same mechanical properties and can be identified as a single material.

Effect of material orientation, Figure 4.12, was small, except if the material principal directions were aligned with global $x - y$ axes. Generally, some physical evidence, such as fiber alignment, or knowledge of material production, can provide an approximation for material principal directions. Accuracy of inclusion identification was significantly improved if material principal directions were not aligned with $x - y$ axes in Figure 4.2.

Larger inclusions had more accurate identification than smaller inclusions. In most cases the interaction stiffnesses, i.e. Q_{12}, Q_{16} and Q_{26}, were more difficult to identify, with the exception being the hard inclusions in Material 3 where all Q_{ij} identifications

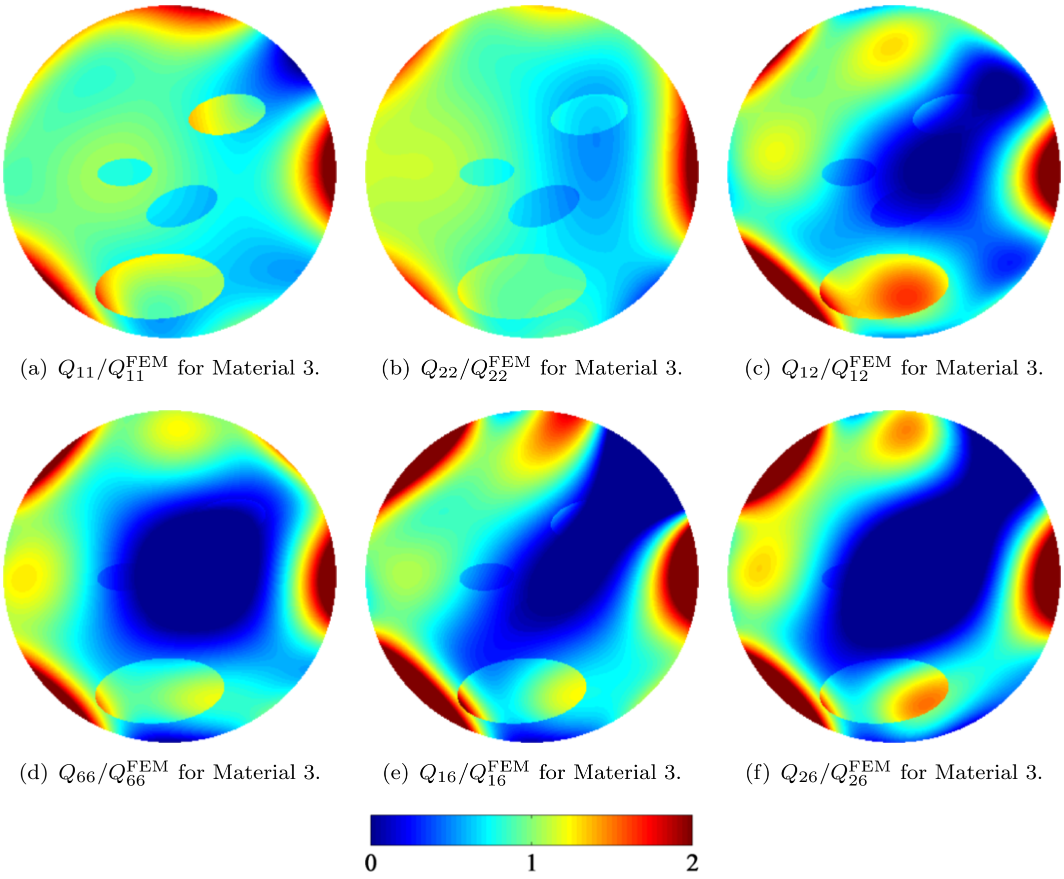
(a) $Q_{11}/Q_{11}^{\mathrm{FEM}}$ for Material 3. (b) $Q_{22}/Q_{22}^{\mathrm{FEM}}$ for Material 3. (c) $Q_{12}/Q_{12}^{\mathrm{FEM}}$ for Material 3.

(d) $Q_{66}/Q_{66}^{\mathrm{FEM}}$ for Material 3. (e) $Q_{16}/Q_{16}^{\mathrm{FEM}}$ for Material 3. (f) $Q_{26}/Q_{26}^{\mathrm{FEM}}$ for Material 3.

FIGURE 4.21: Ratio of Q_{ij} contour maps for Material 3 using 4th order polynomial.

were greatly affected by noise. In most cases, error scaled directly with COV. This scaling provides an additional method for evaluation of experimental results. Often experimental accuracy determination is elusive but COV is readily available. The scaling allows accuracy comparison between each Q_{ij}.

Characterizations of heterogeneous stiffness often include bounds on different homogenized stiffnesses [84]. The Reuss [85] and Voigt [86] estimates provide lower and upper bounds on compliances and stiffnesses of heterogeneous materials. The Reuss estimate assumes the average stress of each inclusion and the matrix is equal to the applied stress and is given by

$$\overline{\mathbf{C}} = (1-f)\mathbf{C} + \sum_{p=1}^{s} f_p \mathbf{C}^p \tag{4.6}$$

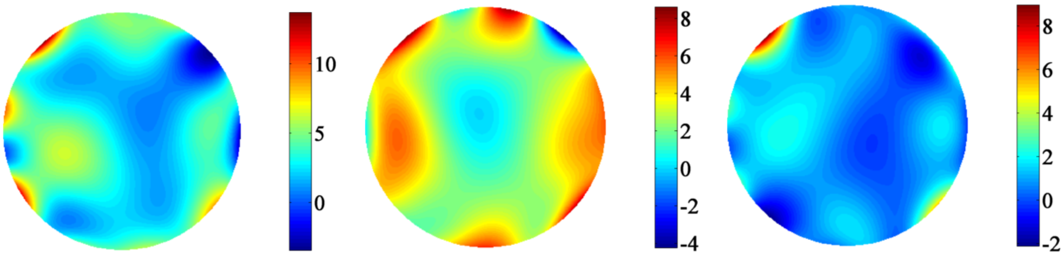

(a) Q_{11} for Material 3. (b) Q_{22} for Material 3. (c) Q_{12} for Material 3.

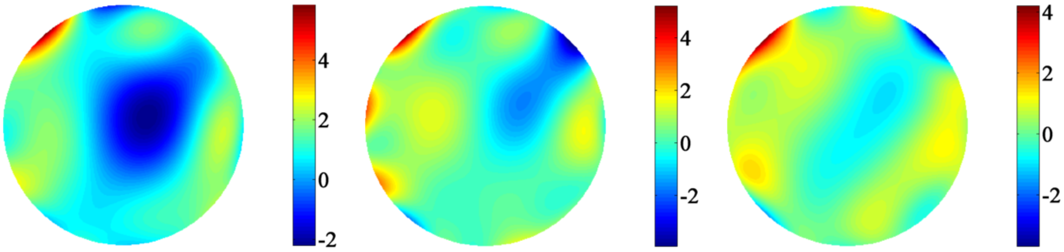

(d) Q_{66} for Material 3. (e) Q_{16} for Material 3. (f) Q_{26} for Material 3.

FIGURE 4.22: Fifth order polynomial Q_{ij} contour maps for Material 3, units $\mathrm{km}^2/\mathrm{s}^2$.

The Voigt estimate assumes the average strain of each inclusion and the matrix is equal to the applied strain and is given by

$$\overline{\mathbf{Q}} = (1-f)\mathbf{Q} + \sum_{p=1}^{s} f_p \mathbf{Q}^p \tag{4.7}$$

where $\mathbf{C}$ and $\mathbf{Q}$ are the compliance and stiffness matrices respectively, f_p is the area fraction of the inclusion of inclusion p and f is the area fraction of all inclusions.

Table 4.4 lists the Reuss and Voigt estimates with the mean homogeneous VFM identification and the mean polynomial stiffness for each material. For the VFM identification, 10 randomizations of 0.3 mm/m strain noise was added to FE strain data. Only a single level of noise was added for these calculations. For these materials the Reuss and Voigt estimates gave narrow bounds, generally less than 1% and usually even less. Therefore, under a variety of load conditions, these materials will act as if they are homogeneous.

With the exception of one case, the homogeneous VFM identified Q_{ij} were within the Reuss and Voigt estimates or greater than the Voight estimate. The single exception is the Material 2, Q_{26}. The largest disparity between the Voight and homogenized VFM identificaton was for Material 3, Q_{12}, just of 6%. The good agreement between these estimate bounds and mean homogenized VFM identified Q_{ij} shows some of the difficulty in characterization of heterogeneous materials. Materials which lack periodic

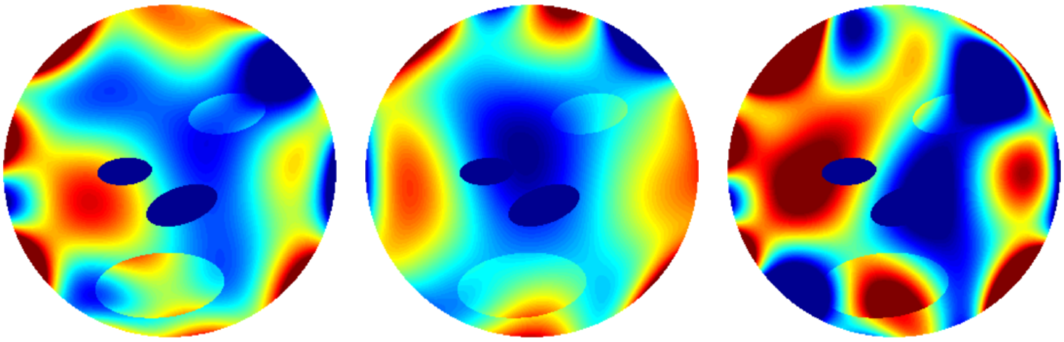

(a) $Q_{11}/Q_{11}^{\mathrm{FEM}}$ for Material 3. (b) $Q_{22}/Q_{22}^{\mathrm{FEM}}$ for Material 3. (c) $Q_{12}/Q_{12}^{\mathrm{FEM}}$ for Material 3.

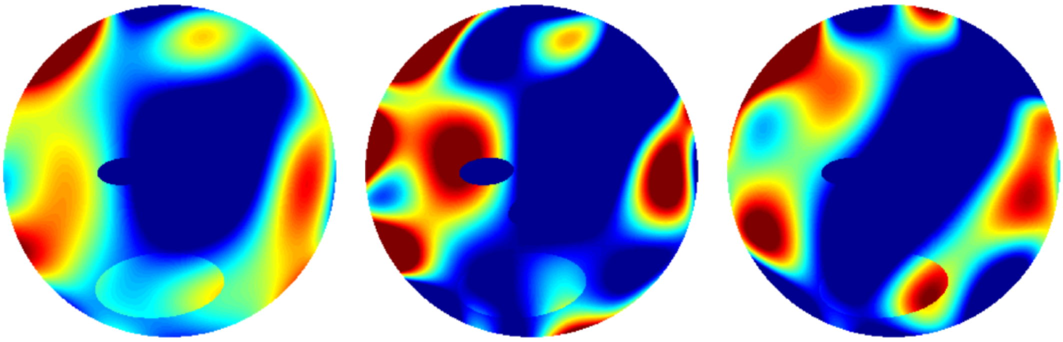

(d) $Q_{66}/Q_{66}^{\mathrm{FEM}}$ for Material 3. (e) $Q_{16}/Q_{16}^{\mathrm{FEM}}$ for Material 3. (f) $Q_{26}/Q_{26}^{\mathrm{FEM}}$ for Material 3.

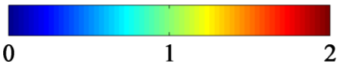

FIGURE 4.23: Ratio of Q_{ij} contour maps for Material 3 using 5th order polynomial.

heterogeneity complicate identification because the effect of different load conditions, whose bounds are given by the Reuss and Voigt estimates, are smaller than experimental error.

Mean Q_{ij} of the 4th order polynomial were similar to the mean homogenized stiffnesses. A portion of this result can be attributed to the large portion of the matrix as compared to the inclusion(s). Except for Material 3, the mean polynomial stiffnesses were below the Reuss estimate. This result is encouraging because Reuss and Voigt estimates are generally unavailable or not possible to calculate. The homogenized VFM, a 0th order polynomial, and higer order polynomial stiffnesses create bounds which can be determined directly from testing.

Expansion of these bounds can give a more precise estimate of the stiffness range within a material. The 5th order polynomial had greater overall error than the 4th order polynomial as shown in Figures 4.21 and 4.23. However, the mean value of the 5th order polynomial Q_{ij} was closer to those in the soft inclusions and effectively reduced the lower

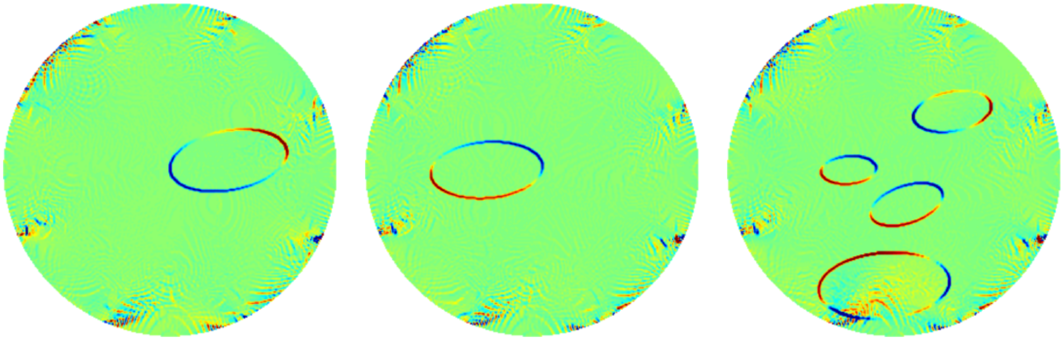

(a) Material 1, 2x2 window size. (b) Material 2, 2x2 window size. (c) Material 3, 2x2 window size.

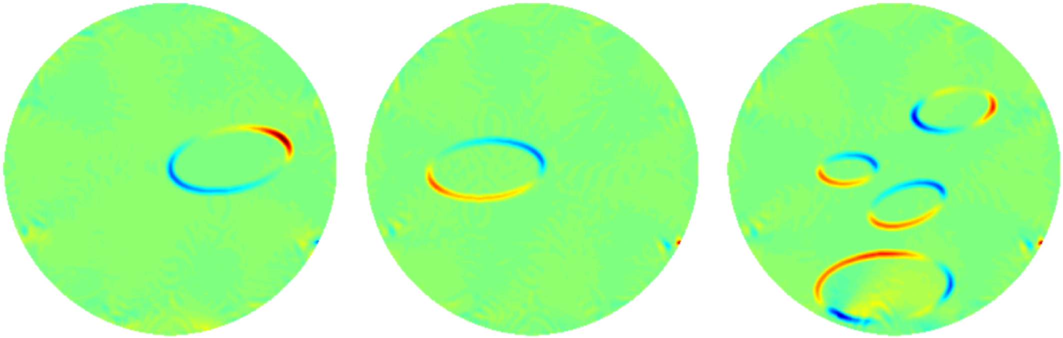

(d) Material 1, 5x5 window size. (e) Material 2, 5x5 window size. (f) Material 3, 5x5 window size.

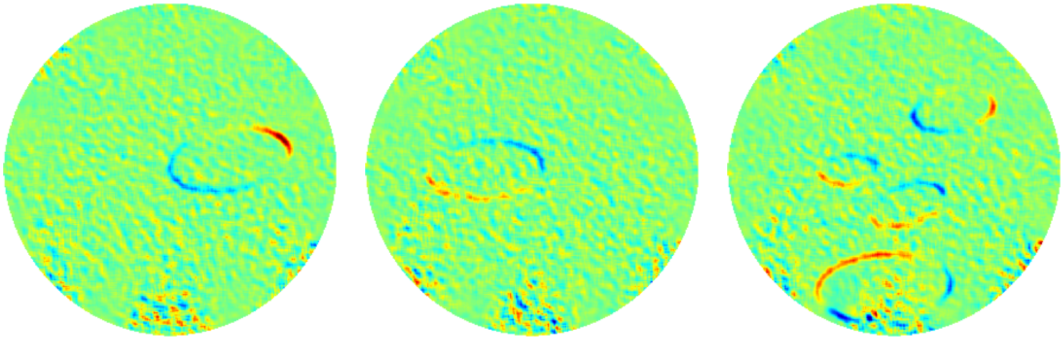

(g) Material 1, 5x5 window size with noise. (h) Material 2, 5x5 window size with noise. (i) Material 3, 5x5 window size with noise.

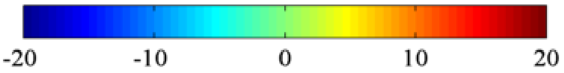

FIGURE 4.24: Equilibrium gap analysis for each material at different window sizes and with 0.3 mm/m noise where indicated; units for scale are dimensionless.

Q_{ij} estimate for Material 3. Many qualifications to this result can be offered, e.g. the soft inclusions had uniformly lower stiffnesses than the matrix which may rarely occur in practice, but careful use of spatially varying polynomial formulations for Q_{ij} can be an effective tool for heterogeneous characterization. Alternatively, these materials were a kind of worst case scenario for the chosen polynomial formulation for Q_{ij} due to the asymmetries of inclusion location and geometry.

Table 4.4: Comparison of Reuss and Voight estimates, homogeneous VFM identified Q_{ij} and mean polynomial Q_j. Units for Q_{ij} are km^2/s^2

Material	Method	Q_{11}	Q_{22}	Q_{12}	Q_{66}	Q_{16}	Q_{26}
1	Reuss	3.37	3.45	0.93	1.32	0.62	0.62
	Voight	3.41	3.46	0.93	1.33	0.63	0.63
	VFM	3.43	3.49	0.93	1.36	0.64	0.65
	4th Order Polynomial	3.40	3.32	0.90	1.23	0.57	0.59
2	Reuss	3.54	3.52	0.96	1.36	0.65	0.65
	Voight	3.55	3.53	0.96	1.37	0.65	0.65
	VFM	3.52	3.50	0.97	1.35	0.65	0.64
	4th Order Polynomial	3.52	3.51	0.86	1.35	0.63	0.68
3	Reuss	3.29	3.43	0.91	1.30	0.61	0.61
	Voight	3.39	3.45	0.93	1.32	0.62	0.63
	VFM	3.44	3.44	0.97	1.31	0.66	0.61
	4th Order Polynomial	3.53	3.48	0.95	1.32	0.69	0.61
	5th Order Polynomial	2.94	2.87	0.95	0.71	0.21	0.23

The EG analysis, Figure 4.24, was able to locate inclusion boundaries effectively. EG mapping should produce zero everywhere except at inclusion boundaries. The 2x2 window size (Figures 4.24(a)-4.24(c)) had more noise near grip and force locations. Some of this noise could be caused by non-equilibrium of the FEM solution. The 5x5 window size (Figures 4.24(d)-4.24(f)) had less noise but the boundaries of the inclusions were wider. Addition of strain noise, Figures 4.24(g)-4.24(i) obscured inclusion boundaries and created regions of non-equilibrium throughout the materials. Given that the inclusions here had large stiffness gradients, ±25-30% of the matrix stiffness, and that less severe gradients are expected in polymeric materials, use of EG mapping in polymeric materials should be used carefully. Determination of differences between non-equilibrium caused by experimental noise and those of heterogeneities may be formidable.

The simulations used in this work were chosen to validate specific approaches to quantifying heterogeneities that may occur in polymers like paper. These simulations do not scale for understanding of micro- or nano-sized inclusions in stiffer, e.g. crystalline, materials. At the smaller scales in these materials misfit strains develop between matrix and inclusion that require the addition of interface energy for equilibrium [87]. For these materials equilibrium is dependent on anisotropy, interface energy, inclusion size and deformation [88].

4.10 Conclusion

Stiffness identification was performed on three, simulated, heterogeneous materials using two VFM formulations. Systematic errors were less than 5% for the matrix and soft inclusions and between 5%-10% for hard inclusions. Accuracy and resolution of Q_{ij} identification were determined by comparison with those used to create the materials in the FEM models. Good accuracy and high resolution validated the VFM approaches described here.

For narrow scope parametrization, spatially-specific stiffness identification was used to describe matrix and inclusion stiffnesses when locations and geometries of the inclusions were known. For broad scope parametrization, a general spatially varying stiffness formulation was used. The broad and narrow scope provided upper and lower bounds on stiffnesses that corresponded well with each material.

A third VFM formulation was used to locate inclusion boundaries. Addition of artificial strain noise blurred inclusion boundaries but boundaries were still evident.

Chapter 5

Heterogeneous, anisotropic stiffness characterization of paperboards with VFM

5.1 Introduction

This chapter characterizes the heterogeneity of three paperboards by specifying upper and lower local stiffness bounds which were identified by different VFM analyses. To the author's knowledge this work represents the first work to use stiffness instead of grammage variation as a measure of heterogeneity.

5.1.1 Background

Strain and deformation heterogeneity in paper and paperboard have been observed by many researchers. Lyne and Hazell [57] produced a comprehensive work attempting to related tensile strength to formation, local strain as measured by holography, and surface temperature distribution. They found a reasonable correlation of $COV(\varepsilon)$ to $COV(formation)$, where $COV(\varepsilon)$ was determined from holograms of tensile specimens. Axelrad et al. [89] used double-sided holographic interferometry to examine a light-weight (62 g/m^2) paper strip in tension. Though not explicitly stated, the specimen appeared to be a handsheet. Stresses were determined on strips across specimen width that were approximately 10 mm long. Stresses in these strips varied widely from near zero to almost three times the mean macroscopic stress in the specimen. de Oliveira et al. [61] evaluated local strain fields in tissue paper. Heterogeneous strains were measured; local strains in direction of applied load were measured up to three times higher and down to 75% lower than macroscopic strain. Hanada and Onabe used holography to examine local deformation field variation [90, 91] of uniaxial tensile specimens. Their holographic images of the macroscopically elastic region showed very large fringe pattern differences between a handsheet with good formation and a handsheet with poor formation. Korteoja et al. [15] examined translucence variation of silicone-impregnated paper during tensile straining and incorporated those results in a FEM model to simulate tensile modulus variation. They did not expect, and their findings did not support, a direct relationship between formation and tensile strength due to competing influences of non-uniform intra-fiber bonding, varying fiber density (along fiber length), uneven planar distribution of fines (very short fibers, < 1 mm long), uneven z-direction distribution of fillers, and non-oriented drying strains. Translucent lines were not observed in MD at any strain level but were observed in CD beginning below 50% ε_{fail}. They performed a numerical simulation in which E, tensile modulus, was assumed to have $COV(E) = 10\%$ and E was linearly related to grammage. Two other parameters for their simulation were G/E, shear modulus to tensile modulus ratio and ratio of $\varepsilon_{fail}/\varepsilon_{yield}$. They assumed flocs were approximately 5 mm in diameter. Two interesting results were increased $COV(E)$ led to increased strain localization, and macroscopic E did not significantly change even up to $COV(E) = 30\%$. Subsequent work by Korteoja et al. [16, 23, 92] used modeling to show $COV(E) \propto COV(\varepsilon)$. To support their modeling, they performed 4000+ tensile tests and determined that $max(E)/mean(E)$ ranged from 1.2 to 3.1 and $min(E)/mean(E)$ ranged from 0.1 to 0.7.

Yamauchi and Murakami [93] examined acoustic emissions and opacity changes of different papers under increasing tensile stress and found almost complete lack of acoustic events during linear elastic loading portion of the test. They also used thermography to examine well-formed and poorly-formed papers [94]; the poorly-formed papers had uneven temperature maps quite early during tensile testing.

Variation of fiber orientation also creates heterogeneity. Enomae et al. [82] measured macroscopic fiber orientation and found that fiber orientation did not, in general, agree with ultrasound-measured anisotropy, which they attributed to non-uniform drying stresses. Erikkilä et al. [81] found fiber orientation varied through thickness of material and the manner of variation depended on rush/drag ratio, the ratio of fiber speed to papermachine wire speed at moment of contact. Odell and Pakarinen [95] measured local (3 mm x 3 mm region) fiber orientation. Their Figure 27 shows a quiver plot, with wide variation, of fiber orientation and anisotropy ratio for an approximately 150 mm wide x 36 mm long paper strip. Though only qualitative, it appeared that fiber mis-orientation tended to decrease anisotropy ratio. Osaki [96] showed fiber orientation varies from $+24°$ to $-30°$ across the width of a paper web. While at International Paper David Vahey helped develop a laser system to analyze local fiber orientation on the millimeter scale. He found that local orientation can vary between $\pm 10°$ and $\pm 20°$ [**?**].

Paper cockling is local out-of-plane deformation. In-plane size of cockles is usually 5-50 mm in diameter and the out-of-plane deviation around 1 mm. Leppänen [97] used a sheet-splitting and imaging technique developed by Erikkilä et al. [81] and found disorder of the local fiber orientation angles was an important factor in the cockling tendency of paper. Relevant for this work is a quote from his thesis, "When considering the future of the modelling of the cockling phenomenon, the lack of measured material parameters could be seen as a huge weakness of these models."

Some researchers have successfully related grammage to stiffness. I'Anson et al. [98] developed a random fiber network model to examine the effects of grammage on tensile specific modulus and specific strength. Their model and associated experiments indicated that the grammage-modulus relationship was more complicated and depended on constituent fibers and amount of pressing. Below a certain grammage, approximately 40 g/m^2, grammage and modulus were directly related; above 40 g/m^2 the specific modulus plateaued. Ostoja-Starzewski and Castro [22] cross-correlated formation images with a biaxial tests of two paper materials. By assuming a constitutive relation that was a function of grammage they achieved good cross-correlation with biaxial tests and an FEM model of the tests and concluded that the representative volume element was on the order of 10 times the floc size.

Wong et al. [19] may have some of the most directly applicable results for this work where they tested laboratory handsheets made at different formation levels. Local grammage was measured using β-radiation. DIC was performed on tensile specimens with dimensions 2 cm wide x 5 cm long. They reported a direct linear relationship between local grammage and local axial strain, though their Figure 9 is not strong evidence of this conclusion; the linear relationship had $R^2 = 0.22$. They suggested that local orientation of properties, material principal property direction, varied from point-to-point in the sheet and would tend to disrupt that linear relationship. One particularly interesting discussion point was shielding, where close proximity of high and low grammage regions could have beneficial or detrimental effects. High grammage regions surrounding a low grammage region seemed to reduce local strains while low grammage regions surrounding a high grammage region seemed to magnify strain in the low grammage regions.

This chapter shows how upper and lower bounds of local stiffness can be defined in order to characterize paperboard heterogeneity. No new techniques or analysis approaches are developed in this chapter, rather, work from previous chapters is employed to define these bounds. The VFM is central to all the work in this chapter and a more full use of all identification parameters is described. Upper and lower stiffness bounds are validated by visual comparison with formation and with VFM-determined stiffness variation.

5.2 Materials

Three materials were examined, two linerboards and a filter paper. Linerboards were denoted Linerboard 2 and Linerboard 3; Linerboard 2 was also examined in Chapter 2 where it was also denoted Linerboard 2 and in Chapter 3 where it was denoted Linerboard. A designation 'Linerboard 1' was used in Chapter 2 and so that designation is not used here. The filter paper was also examined in Chapters 2 and 3, where it was denoted as F or Filter. Linerboard 3 was not examined previously.

Filter is a commercial filter paper manufactured by Whatman® International (Maidstone, Kent, UK), identified as Chromotography Paper, Model 3MM CHR, and was chosen because it is 100% cellulose from cotton linters, one of the longest cellulose fibers available. Linerboard 2 was made on a Fourdrinier papermachine and is an unbleached, kraft single-ply linerboard; Linerboard 3 was made on a different Fourdrinier papermachine than Linerboard 2, but is also an unbleached, kraft single-ply linerboard. Both linerboards represent those used in structural paperboard products such as corrugated containers.

Filter was chosen for this analysis because it is visually homogeneous and its homogeneity is important in application. As with the linerboards, it is made on a Fourdrineir papermachine, but at lower speed, approximately 3x lower, than the speed used for general linerboard production. The lower speed, lower grammage and density, help reduce material variability. Material variability in linerboards is higher, but is considered to be an inherent part of the manufacturing process and is compensated for by using higher grammage and larger safety factors when used in structural applications. A safety factor of 5 or higher is not uncommon in corrugated structures.

Table 5.1: Physical and mechanical properties of materials examined

Property	Filter	Linerboard 2	Linerboard 3
Grammage (g/m^2)	187	209	214
Thickness (mm)	0.31	0.30	0.33
Density (kg/m^3)	603	688	645

5.3 Experimental plan

Chapter 3 described the load frame used to provide full-field strains used to identify anisotropic stiffnesses. Those stiffnesses were identified using a VFM analysis which assumed a homogeneous material. Variation of identified stiffnesses was used to determine quality of identification.

Chapter 4 described three VFM analysis methods which were used to characterize simulated heterogeneous materials. The first method assumed that heterogeneous regions were known a priori. The second method used a spatially-varying polynomial function for Q_{ij}. The third method, labeled 'EG' for 'equilibrium gap', examined the specimen to define borders between dissimilar materials.

Here, the load fixture described in Chapter 3 and the homogeneous VFM analysis are used to identify stiffness values which should be contained within upper and lower stiffness bounds. The VFM analysis developed in Chapter 4, in which location and geometry of inclusions were known a priori, were used on the same data used to identify homogeneous stiffnesses to determine if Q_{ij} variation was grammage-based. Such a relation may exist for some paper materials, such as handsheets, but would be unexpected for the materials selected here. An entirely grammage-based variation for stiffness would suggest either that the entire specimen had the same fiber orientation or that fiber orientation also varied directly with mass. Either possibility is unlikely in Fourdrinier papermaking. To examine the possibility that local stiffness and mass were related, local grammage was measured prior to specimen preparation. The method used to measure grammage variation is described in the following section.

Following measurement of local grammage variation the specimens were prepared according the the procedure in Chapter 3. Dot pattern used for prior DIC investigations was photocopied on specimens with a Sharp® (Sharp Electronics Corp., Mahwah, New Jersey) MX-3100N copier.

In Chapter 3 specimens were approximately aligned so that MD was coincident with the y-direction of the load fixture, Figure 5.1, to maximize the strains in the 1-principal direction of the material. Since the concern here is for accurate parameter identification of all stiffnesses the MD was oriented at approximately 135°. This orientation will maximize the absolute value of Q_{16} and Q_{26} and provide reasonable η (COV of stiffness) for those parameters. All other measurement details correspond with those in Sections 3.3-3.4.

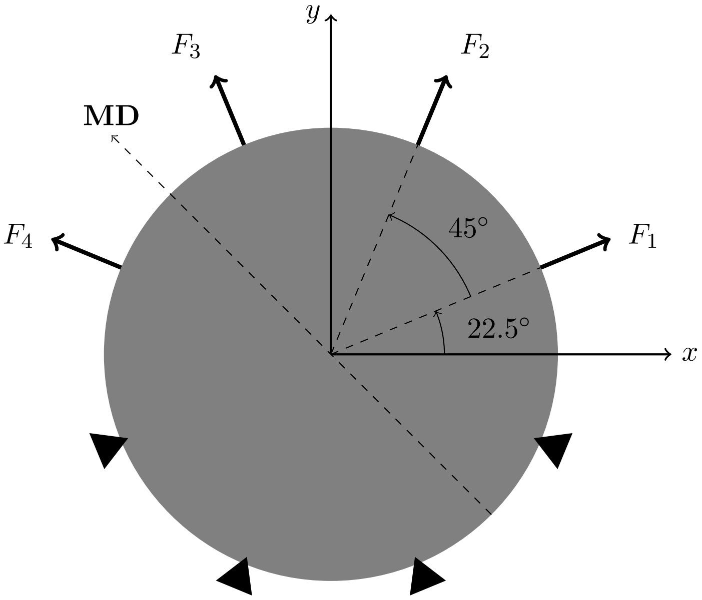

FIGURE 5.1: Schematic of load fixture, note orientation of MD.

5.4 Measurement of grammage variation[1]

Different methods are used to determine grammage variation, but all methods involve measurement of energy through the material. White light [99, 100], beta-radiation [101] and x-rays [102] have been successfully used to examine grammage variation. NIR (near infrared radiation) has many beneficial attributes for examination of cellulose materials [103] and, important for this work, is its relative insensitivity to lignin. NIR is preferred over visible light, especially for unbleached linerboards containing lignin. Lignin absorbs more in the ultraviolet and visible regions than in the NIR, resulting

---

[1] This section was produced in collaboration with Dr. Vahey.

in dark images with poor resolution. NIR transmission was used to provide a local grammage map for each material.

A beam of NIR of uniform intensity was projected on a paper specimen and the transmitted output was imaged by a CCD camera. Brightness of the NIR source and aperture of the camera lens were adjusted so that the average GV (gray value) of the image was close to 128 on a scale from 0 to 256. The bell-shaped curve describing the histogram of the image indicates darker regions (GV $<$ 128), generally corresponding to higher grammage regions, and lighter regions (GV $>$ 128) generally corresponding to lower grammage regions.

The actual relation between grammage and GV depends on the constituents and structure of the paper, and is not likely to be linear. Nevertheless, the NIR method is fast, inexpensive and safe compared to common alternatives involving beta rays or X-rays, especially when there is need to measure large areas with high spatial resolution. If one can tolerate coarse resolution, such as limiting consideration to high, medium and low grammage regions, the use of NIR transmission is a good surrogate for grammage.

Figure 5.2 is a diagram of the grammage measurement system. The source was a 10x10 array of LEDs with 90% of its output above 800 nm in wavelength and 65% of its output in the range 800 850 nm. The manufacturer was DVT Systems, now Cognex (Cognex Corporation, Inc., Natick, MA, USA). The LED array was 5 cm on a side, small compared to the 25 cm diameter of the region of interest of the paper specimen. Distance from paper specimen to array was 60 cm. The LED array was powered by 12V DC, at a constant current of 900 mA, and was not changed during the course of the experiments, except that the array was occasionally powered down to avoid heating effects on output.

The camera was a Hitachi CCD Model KP-160 (Hitachi High Technologies America, Inc., Schaumburg, IL, USA) which had peak spectral response at 750 nm, falling to 50% of peak at 900 nm. Camera images were 640x480 pixels and the sensor format was 1/2 inch. The lens was a Schneider lens optimized for 400-1000 nm wavelengths. Focal length was 12 mm and the maximum aperture was 1.4. In operation, the lens aperture was electronically adjusted to a midrange value that produces histograms centered between 70 and 140 GV for the different materials examined. Once adjusted, the aperture was not changed. Keeping both the power to the LED array and the aperture constant maximizes but does not insure the utility of GV as a surrogate for grammage; changes in GV from sheet to sheet are reflective of changes in constituents and structure of the papers and

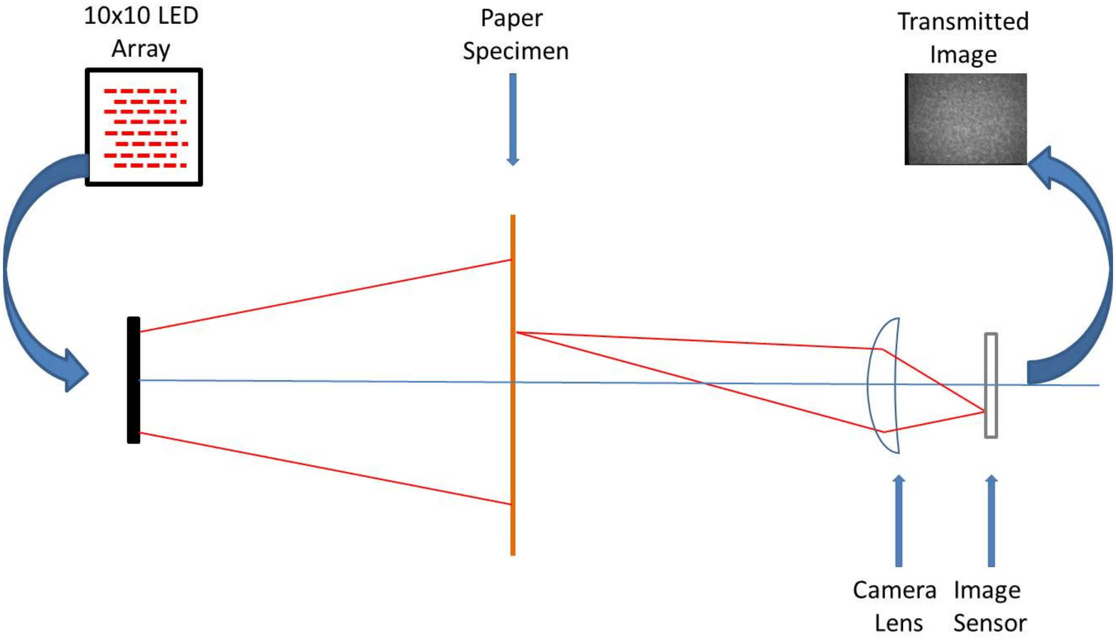

Figure 5.2: Schematic layout for NIR grammage variation measurement.

not changes to the optics. Distance from the specimen to the lens in Figure 5.2 was 72 cm and a 5 mm extender tube was inserted between the lens and camera to provide focus at the required field of view. The ability to measure 0.5 mm variations in GV over a 25-cm field of view is not believed to be common to devices manufactured specifically for measurements of paper samples, owing to the large footprint required.

NIR energy distribution was not uniform across the specimen. Because Filter material was 100% cellulose, and therefore contained no lignin to affect NIR absorbance, and had small grammage variation, it was chosen to create a master image for correcting the NIR energy distribution. A single image of NIR transmission though a Filter specimen is shown in Figure 5.3(a) and is shown in color for better visualization. Specimen was a rectangle nominally 36 cm wide and 25 cm in height. Ten successive images were taken and averaged to reduce affects of electronic fluctuations in system components. A 10-image average is shown in Figure 5.3(b). Figure 5.3(b) was 'blurred' using a PSF (point-spread function) to reduce the GV fluctuations of the Filter specimen. The PSF was set to 31 pixels of linear camera motion and 11° of rotation. The 'blurred' image is shown in Figure 5.3(c) and represents the NIR energy distribution transmitted through a 100% cellulose sheet with density equal to the Filter material. Variation of NIR energy distribution was corrected by performing a pixel by pixel division of the 10-image averaged image by the 'blurred' image. An example normalized image is shown in Figure 5.3(d).

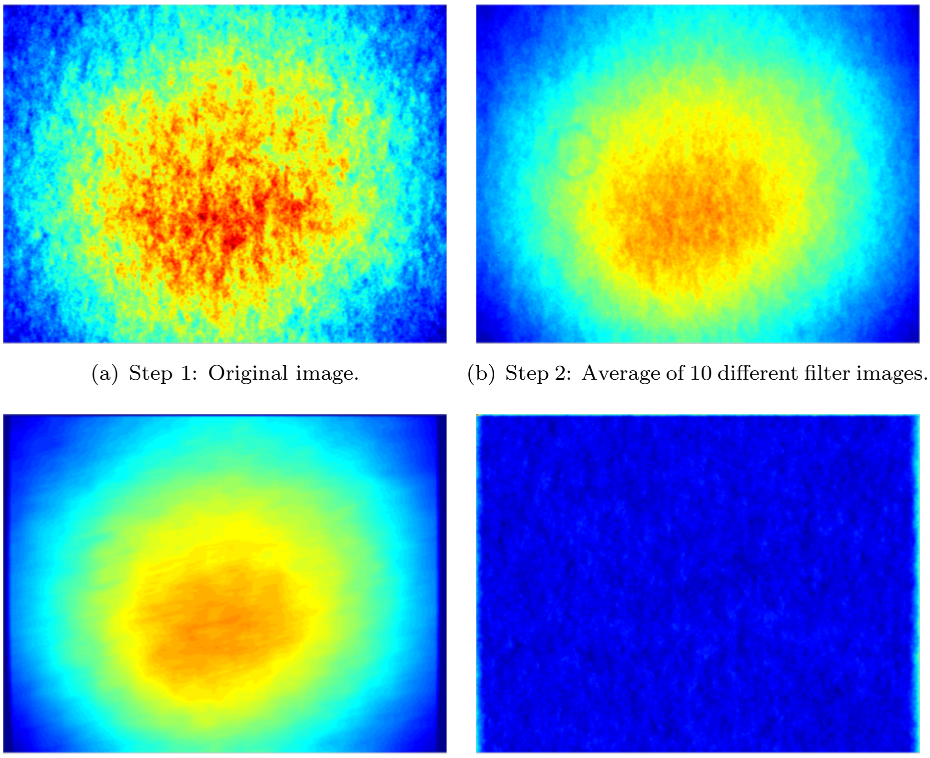

(a) Step 1: Original image.

(b) Step 2: Average of 10 different filter images.

(c) Step 3: Blurrred image.

(d) Step 4: Normalized image.

Figure 5.3: Processing of images to identify density variation. Rectangular specimens were 28 cm high and 36 cm wide.

It was important to spatially correlate images used to evaluate grammage variation with those used in DIC measurements. Accordingly, prior to NIR imaging, two reference holes were punched in each specimen. These holes corresponded to grips at locations 22.5° and 202.5°. Ten NIR images were taken of each specimen; images were taken approximately one minute apart without any changes to the NIR system. These ten images were averaged and then a pixel by pixel division by the image in Figure 5.3(c) was performed to produce a corrected GV image of each material. Using the reference holes, the image was rotated and cropped to correspond to the actual specimen placed in the load fixture. GV images for each material along with their coinciding GV-normalized histograms are shown in Figures 5.4-5.6.

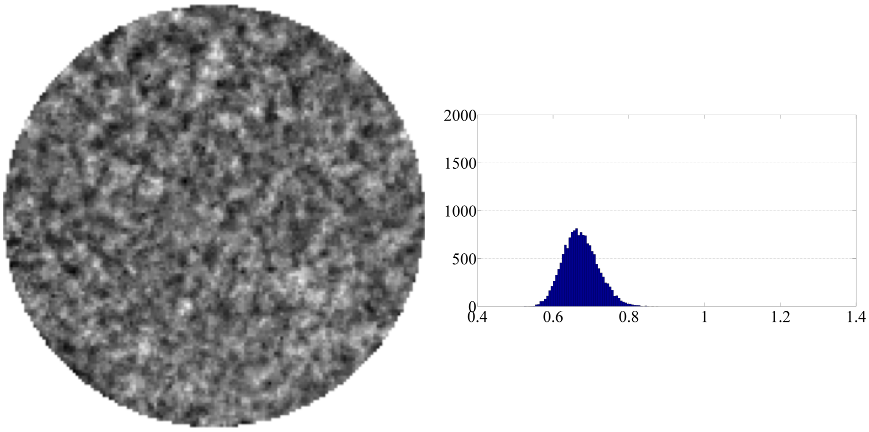

(a) Linerboard 2 corrected grayscale image, specimen was 24.5 cm in diameter.

(b) Linerboard 2 corrected grayscale histogram.

FIGURE 5.4: NIR image with associated histogram for Linerboard 2.

Mottled appearance of Linerboard 2 in Figure 5.5 represents grammage variation, with higher grammage regions being darker and lower grammage regions being lighter. Because Linerboard 2 had higher grammage than Filter the mean corrected GV value was below '1'.

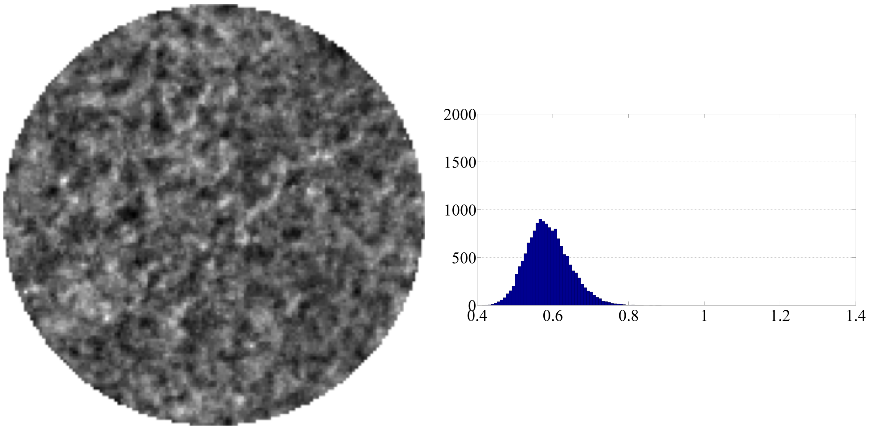

(a) Linerboard 3 corrected grayscale image, specimen was 24.5 cm in diameter.

(b) Linerboard 3 corrected grayscale histogram.

FIGURE 5.5: NIR image with associated histogram for Linerboard 3.

Linerboard 3 had higher grammage than Linerboard 2, therefore its mean corrected GV was lower than that of Linerboard 2. The right tail of the histogram is slightly extended, producing a marginally non-normal GV distribution. The extended right tail indicates that the lighter grammage regions were not reciprocated by heavy grammage regions.

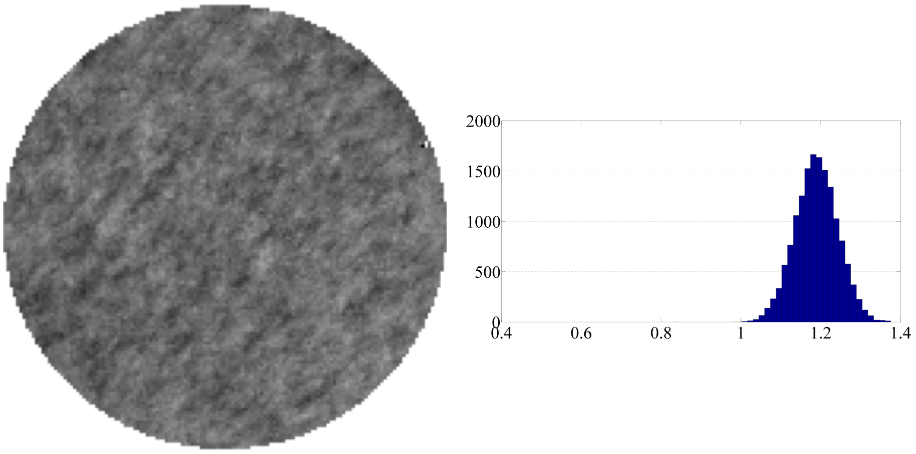

(a) Filter, corrected grayscale image, specimen was 24.5 cm in diameter.

(b) Filter, corrected grayscale histogram.

FIGURE 5.6: NIR image with associated histogram for Filter.

The histogram for Filter, Figure 5.6(b), has a greater peak and narrower half-height width suggesting less grammage variation. The corrected GV image, Figure 5.6(a) shows much less variation than those of Linerboard 2 and 3, Figures 5.4(a) and 5.5(a).

5.5 Specimen preparation and testing

After NIR imaging, the DIC pattern was laser printed on each specimen. Specimen were then cut using alignment holes placed in the specimens prior to NIR imaging and so that the nominal MD was oriented in the load frame at 135°. All tests were performed at 50% RH and 23°C.

No changes were made in the load frame from Chapter 3. The load configurations in those tests were used as a guide for the load configurations used here and were selected to help ensure linear behavior.

5.6 Use of VFM to characterize heterogeneity

The investigation in this chapter incorporates previously developed VFM analyses.

Three items used in the VFM analysis in Chapter 3 are important here. First, superposition of tests, i.e. adding strains and applied loads from individual tests to create a new test, improved identification by reducing strain signal to noise ratio. While that particular aspect is important here, test superposition can also be used to create tests, from different materials, which have similar strain levels. Secondly, the η_{ij}/Q_{ij}s, which are COV(Q_{ij}), were used in Chapter 3 to compare quality of parameter identification. In this chapter, the η_{ij}/Q_{ij}s will be used to provide a relative estimate of parameter variation, where relative means comparison between the same Q_{ij}. Because the η_{ij}/Q_{ij} depend on strain level, this was illustrated in Chapter 3, superposition tests for each material was created to have similar strain levels. Thirdly, the Q_{ij} identified with the homogeneous material assumption should lie within Q_{ij} heterogeneous bounds.

Each of the three analyses developed in Chapter 4 were used here to characterize heterogeneity. Equation 4.2 was used when location and geometry of regions of different materials were known within the specimen. In the present work, the specimens were divided into different regions based on grammage determined by NIR imaging. While the paper specimen can be divided into regions of similar grammage, fiber orientation, density and drying stresses were unknown in these regions. Since these properties were unknown, VFM parameter identification of a material segmented by grammage is greatly improved if all these properties are constant throughout the specimen, i.e. stiffness is directly related to grammage. Unlike the simulated materials in Chapter 4 in which the inclusions comprised a small portion of the specimen, 8%, similar grammage regions comprise a large portion of the specimen, which improves identification, but are subdivided throughout the material, which tends to damp differences in identification. This damping occurs because full-field measured strains are smooth and piecewise virtual fields tend to further increase smoothing.

Equation 4.4 was used to identify a spatially-varying Q_{ij}. In Chapter 4 both 4th and 5th order polynomials were used to provide lower bounds on parameters. Higher order polynomial formulations for Q_{ij} require successively more parameters to be identified. A 4th order polynomial requires 150 parameters to be identified; a 6th order polynomial requires 294 parameters to be identified, nearly twice as many. Likewise, VFM mesh density needs to adjusted so that proportionate degrees of freedom are available. In Chapter 4, the noise optimization matrix, $\mathbf{G}$, became ill-conditioned when high artificial strain noise was added and a 6th order polynomial was used; at low levels of strain noise higher order polynomials could be used. NIR images suggest that spatial frequency of grammage variation is greater than 6th order. The polynomial formulation for Q_{ij} will help provide upper and lower bound estimates for the parameters.

The third VFM analysis developed on Chapter 4 was EG (equilibrium gap) mapping. There EG mapping was effective at determining inclusion boundaries, though addition of artificial strain noise tended to obscure those boundaries. Similar mapping was employed here.

All of these analyses were used with the same, superimposed test data to maximize strain signal-to-noise ratio.

5.6.1 Selection of VFM mesh density

Selection of VFM mesh for subsequent analyses is not straightforward for heterogeneous materials, especially when the manner of heterogeneity is unknown. Sufficient degrees of freedom, determined by unconstrained virtual nodes, are needed for accurate identification. Figure 5.7 shows Q_{ij} identification for several mesh densities. Generally, the coarsest mesh possible for good identification is chosen as high mesh densities tend to intensify strain noise. For two VFM analyses, assumed homogeneity and area-segmented, 10^2 mesh density was used. For the polynomial Q_{ij} VFM analysis 20^2 mesh density was used in order to have necessary degrees of freedom for identification.

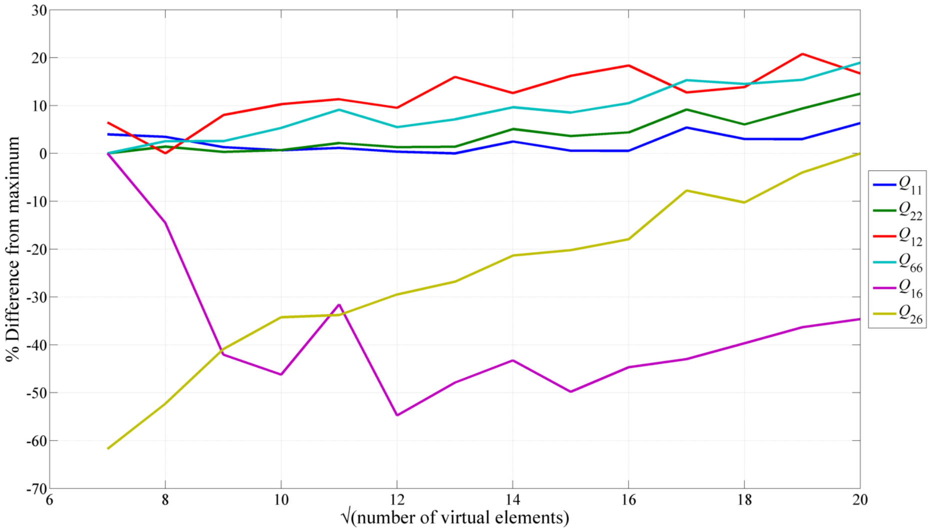

(a) Effect of mesh density on Q_{ij} identification for Linerboard 2.

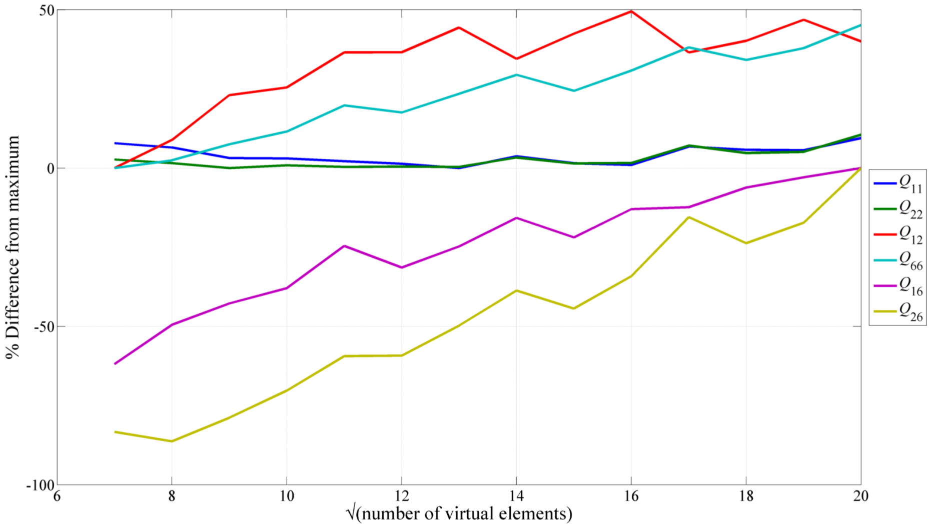

(b) [Effect of mesh density on Q_{ij} identification for Linerboard 3.

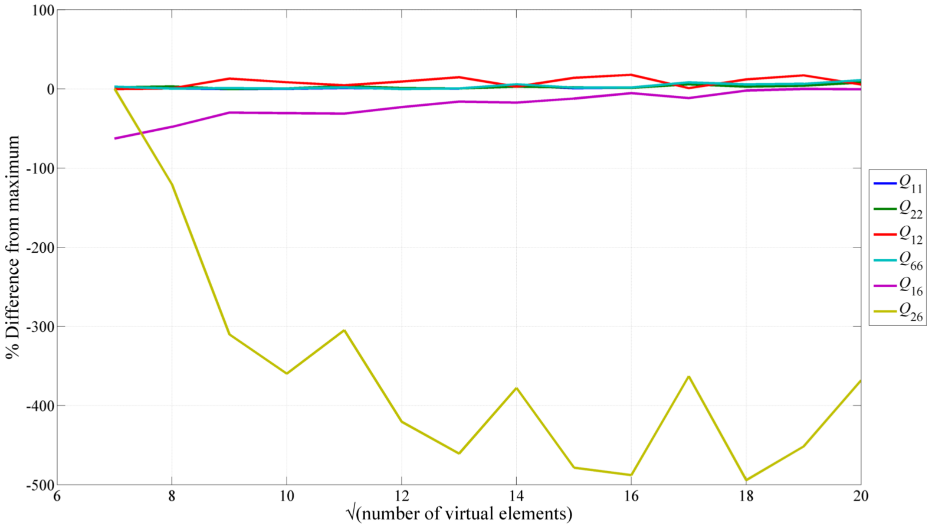

(c) [Effect of mesh density on Q_{ij} identification for Filter.

FIGURE 5.7: Effect of virtual mesh density on Q_{ij} identification for each material.

5.7 Results

Tables 5.2-5.4 give identification results for each of the three materials. The first section of each table gives the Q_{ij}, η_{ij} and F_i for individuals tests; analysis assumed the material was homogeneous. Rows labeled 'mean' and 'COV' list the mean and COVs for identification results of the individual tests. The row labeled 'Superposition' lists identification results when individual tests are superimposed to create a single, composite test. This approach was also used in Chapter 3. For this test, individual strains and forces were added together, i.e. superimposed, to maximize strain and reduce effects of experiment noise on parameter identification. Though not shown, force-strain behavior of the individual tests were examined to ensure materials had linear behavior. VFM mesh used for each of these analyses had 100 elements.

The next section of each table lists results when material was partitioned into similar grammage regions based on NIR images for each material, using GV as a surrogate for grammage. For Linerboard 2 identification was performed by partitioning grammage into three different types of subregions: (1) two equal-area subregions, a high grammage region and a low grammage region, (2) three equal-area subregions, and (3) three subregions with the high grammage region and low grammage subregions at 25% each of specimen area and a medium grammage region at 50% specimen area. Figure 5.8 shows Linerboard 2 divided into three equal-area grammage subregions. Similar subdivisions were made for Linerboard 3, except that the optimized, special virtual fields could not be found for when the grammage was divided into 3 equal-area subregions. For Filter, special optimized virtual fields were found only when grammage was divided in two regions of equal area. All identification in this section was performed using superimposed strain-force data. VFM mesh used for these analyses used 100 elements.

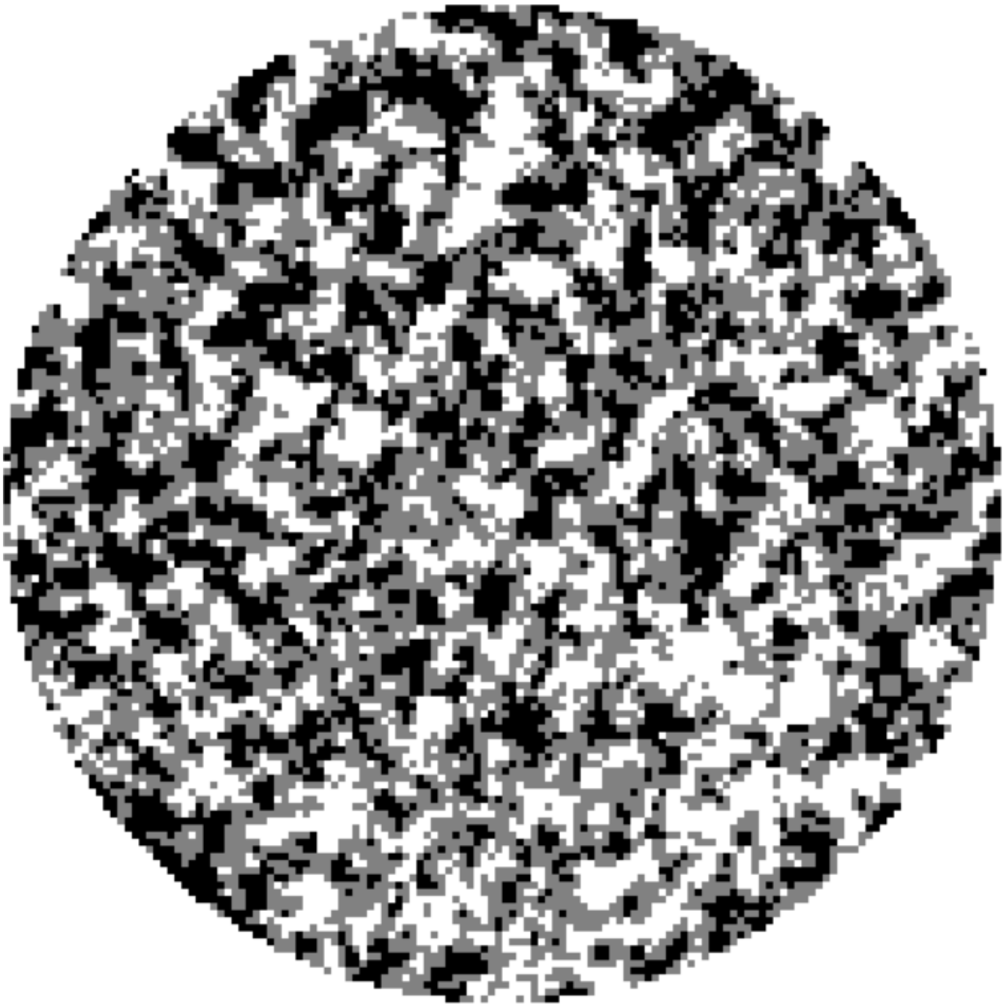

FIGURE 5.8: Linerboard 2: grammage division into 3 equal-area subregions, where white: high grammage regions, gray: medium grammage regions, and black: low grammage regions.

The final section of each table lists the polynomial identification results. Three different polynomial orders were used for identification; 400 VF elements were used for the polynomial analysis. A single, high density mesh was used to provide the necessary degrees of freedom for parameter identification. The 5th order polynomial formulation required identification of 216 parameters. Experience has shown that good identification requires approximately twice the degrees of freedom as the number of parameter to be determined. All identification in this section was performed using superimposed strain-force data.

Figure 5.9 shows the identification mapping for Linerboard 2 with a 4th order polynomial. Figure 5.10 shows same mapping but normalized by the 'Superposition' identification

TABLE 5.2: Identification results for Linerboard 2, η_{ij}/Q_{ij} abbreviated as η_{ij}, units: Q_{ij} (km^2/s^2), η_{ij} (m^3), F_i (N)

	Q_{11}	Q_{22}	Q_{12}	Q_{66}	Q_{16}	Q_{26}	η_{11}	η_{22}	η_{12}	η_{66}	η_{16}	η_{26}	F_1	F_2	F_3	F_4
Homogeneous Analysis	4.69	6.54	1.45	3.58	-0.88	-1.29	44	44	131	89	-207	-145	28.2	28.5	30.5	29.8
	4.57	6.29	1.26	3.42	-0.79	-1.03	41	40	135	82	-203	-157	30.5	30.7	30.5	29.9
	4.48	6.47	1.33	3.45	-0.87	-1.43	41	40	129	88	-194	-119	28.2	28.9	34.9	32.4
	4.45	6.44	1.33	3.64	-0.97	-1.60	41	41	131	91	-188	-114	27.5	28.0	35.5	34.3
	4.62	6.59	1.31	3.60	-0.95	-1.66	40	40	134	87	-185	-107	28.6	28.0	37.0	36.5
	4.75	6.90	1.51	3.78	-1.10	-1.72	39	41	121	85	-160	-109	31.5	28.0	39.1	38.7
mean	4.59	6.54	1.37	3.58	-0.93	-1.45	41	41	130	87	-190	-125				
COV (%)	2.4	2.9	6.2	3.4	-10.5	-16.5	4	3	4	4	-8	-15				
Superposition	4.61	6.60	1.37	3.60	-0.94	-1.48	7	7	22	15	-31	-20	174.5	172.1	207.4	201.7
Grammage-based heterogeneity																
2 grammage divisions, 50% area each																
High	5.25	8.48	1.68	11.69	-1.87	0.50	45	23	81	54	-122	358				
Low	4.41	3.32	1.04	2.06	-0.54	-3.10	62	60	146	336	-498	-61				
Mean	4.83	5.90	1.36	6.87	-1.20	-1.30										
3 grammage divisions, 33% area each																
High	7.15	5.73	-0.05	10.14	-2.79	-2.20	77	89	-9296	172	-223	-235				
Medium	4.54	8.17	2.49	6.11	-0.06	0.41	81	40	100	190	-6077	704				
Low	2.49	4.06	1.52	2.80	-0.26	-2.36	162	78	182	385	-1625	-139				
Mean	4.72	5.99	1.32	6.35	-1.03	-1.38										
3 grammage divisions, 25% high grammage, 50% medium grammage, 25% low grammage																
High	7.31	6.74	-0.22	7.98	0.33	-1.96	50	51	-1172	152	1272	-160				
Medium	3.19	8.11	3.82	10.84	-2.29	1.27	153	51	83	147	-215	301				
Low	1.78	2.44	1.74	1.13	-2.49	-2.81	263	165	174	1132	-186	-131				
Weighted Mean	3.87	6.35	2.29	7.70	-1.69	-0.56										
Polynomial																
3rd Order	2.88	6.21	1.16	1.92	-0.79	-0.63										
4th Order	1.58	4.32	1.47	0.29	0.05	0.04										
5th Order	1.04	5.41	1.47	1.94	-0.89	-0.59										

TABLE 5.3: Identification results for Linerboard 3, η_{ij}/Q_{ij} abbreviated as η_{ij}, units: Q_{ij} (km^2/s^2), η_{ij} (m^3), F_i (N)

	Q_{11}	Q_{22}	Q_{12}	Q_{66}	Q_{16}	Q_{26}	η_{11}	η_{22}	η_{12}	η_{66}	η_{16}	η_{26}	F_1	F_2	F_3	F_4
Homogeneous	5.55	6.86	1.16	5.99	-1.27	-1.93	61	61	274	146	-317	-223	28.4	20.9	32.6	29.6
Analysis	5.64	7.13	0.96	6.12	-1.21	-2.10	61	61	333	143	-339	-207	28.5	22.2	33.5	30.2
	5.58	6.87	1.04	6.47	-1.17	-2.03	55	57	279	131	-324	-204	32.3	22.2	34.9	32.9
	5.19	6.55	1.08	6.21	-1.15	-2.08	52	53	241	133	-312	-185	31.6	24.5	37.9	32.6
	5.27	6.71	1.07	5.39	-1.06	-1.85	47	50	227	133	-281	-180	34.9	24.9	38.2	34.8
	5.11	6.43	1.18	5.88	-1.24	-1.82	46	48	192	123	-249	-182	36.4	26.2	39.0	36.0
mean	5.39	6.76	1.08	6.01	-1.18	-1.97	54	55	258	135	-304	-197				
COV (%)	3.8	3.4	6.9	5.5	-5.6	-5.5	11	10	17	6	-10	-8				
Superposition	5.41	6.80	1.10	6.19	-1.25	-2.04	9	9	42	23	-49	-33	192.1	141.0	216.2	196.0
Grammage-based heterogeneity[a]																
2 grammage divisions, 50% area each																
High	7.85	6.21	-0.13	5.93	0.47	-0.24	30	51	-1517	194	641	-1385				
Low	2.26	6.61	2.55	16.31	-2.04	-4.38	101	53	81	99	-193	-98				
Mean	5.06	6.41	1.21	11.12	-0.78	-2.31										
3 grammage divisions, 25% high grammage, 50% medium grammage, 25% low grammage																
High	4.71	4.12	-0.46	15.31	-4.55	-1.96	125	120	-802	175	-175	-303				
Medium	10.24	8.90	1.96	5.01	3.85	1.46	73	90	264	830	267	694				
Low	1.39	8.10	4.05	20.36	1.46	-6.32	461	81	105	159	646	-128				
Weighted Mean	6.64	7.51	1.88	11.42	1.15	-1.34										
Polynomial																
3rd Order	1.39	6.34	-0.53	1.90	-1.04	-0.43										
4th Order	2.15	3.95	0.55	2.18	-0.21	-0.72										
5th Order	1.74	5.55	0.16	-0.57	-1.77	0.18										

---

[a] Could not find special optimized fields when grammage divided equally into 3 grammage divisions

TABLE 5.4: Identification results for Filter, η_{ij}/Q_{ij} abbreviated as η_{ij}units: Q_{ij} (km^2/s^2), η_{ij} (m^3), F_i (N)

	Q_{11}	Q_{22}	Q_{12}	Q_{66}	Q_{16}	Q_{26}	η_{11}	η_{22}	η_{12}	η_{66}	η_{16}	η_{26}	F_1	F_2	F_3	F_4
Homogeneous	3.36	3.76	0.71	1.68	-0.51	-0.11	30	31	122	54	-118	-589	25.0	16.0	26.0	24.7
Analysis	3.32	3.95	0.71	1.69	-0.58	-0.08	27	26	110	48	-95	-664	28.2	17.3	34.4	25.2
	3.23	4.32	0.70	1.78	-0.62	-0.40	24	24	103	43	-80	-133	28.0	17.3	45.7	29.0
	3.25	4.16	0.64	1.81	-0.64	-0.46	22	21	101	38	-72	-102	27.7	17.8	49.2	32.2
mean	3.29	4.05	0.69	1.74	-0.59	-0.26	26	25	109	46	-91	-372				
COV (%)	1.6	5.2	4.5	3.2	-8.3	-64.5	12	14	8	13	-19	-69				
Superposition	3.31	4.09	0.68	1.74	-0.61	-0.28	6	6	28	11	-22	-49	108.9	68.5	155.4	111.1
Grammage-based heterogeneity[a]																
2 grammage divisions																
High	4.39	1.90	0.26	6.05	-2.40	0.00	28	69	373	49	-44	31787				
Low	1.96	6.58	0.91	0.29	1.14	-0.69	62	24	107	931	81	-150				
Mean	3.17	4.24	0.59	3.17	-0.63	-0.34										
Polynomial																
3rd Order	2.35	4.62	1.23	2.21	-0.00	-0.82										
4th Order	2.11	3.80	0.85	1.55	0.17	-0.56										
5th Order	0.74	2.58	0.77	0.08	-0.04	-0.25										

---

[a] Could not find special optimized fields for smaller grammage subdivisions

in Table 5.2; 'H' denotes homogeneous identification. The wide scale for Figure 5.9 comprises large negative values, even for Q_{11} and Q_{22}. Mapping for Q_{66} shows a negative shear modulus for approximately one third of the specimen and has an axis of symmetry at about -45°. Figure 5.10 shows amount of deviation from homogeneity.

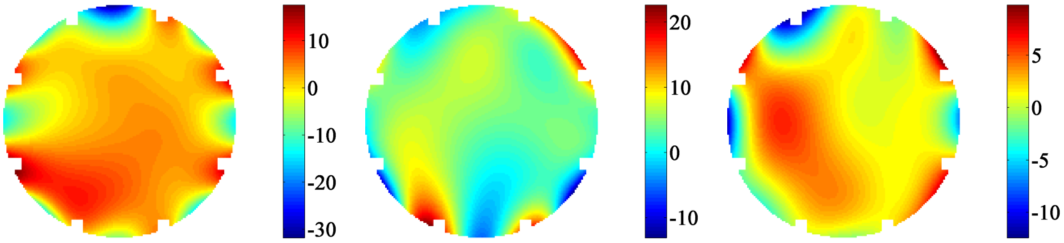

(a) Q_{11} for Linerboard 2. (b) Q_{22} Linerboard 2. (c) Q_{12} Linerboard 2.

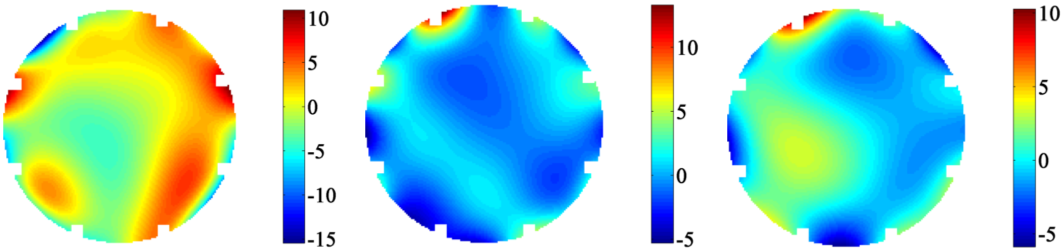

(d) Q_{66} Linerboard 2. (e) Q_{16} for Linerboard 2. (f) Q_{26} for Linerboard 2.

FIGURE 5.9: Fourth order polynomial Q_{ij} contour maps for Linerboard 2, units $\mathrm{km}^2/\mathrm{s}^2$.

Figure 5.11 shows the identification mapping for Linerboard 3 with a 4th order polynomial. Figure 5.12 shows same mapping but normalized by the 'Superposition' identification in Table 5.3. Very noticeable was a low stiffness region in Figure 5.9(b) and high modulus regions in Figures 5.11(c) and 5.11(d). The normalized maps in Figure 5.12 showed large stiffness gradients in the central region, where the strain gradients were small. Stiffness gradients near grip locations may be developed by some concentrated nonlinear material behavior, but gradients in the central region of the specimen indicate material heterogeneity.

Figure 5.13 shows the identification mapping for Filter with a 4th order polynomial. Figure 5.14 shows the same mapping but normalized by the 'Superposition' identification in Table 5.4. The stiffness gradients near the grip regions are emphasized in Figure 5.14. It is unclear why the grip regions indicated greater stiffness instead of reduced stiffness. However, the high stiffness regions in Figure 5.13 comprise only a small portion of the specimen area.

The left column of Figure 5.15 shows the EG mapping for each material using 3x3 data points for each EG element. Stiffnesses used to calculate local equilibrium came from

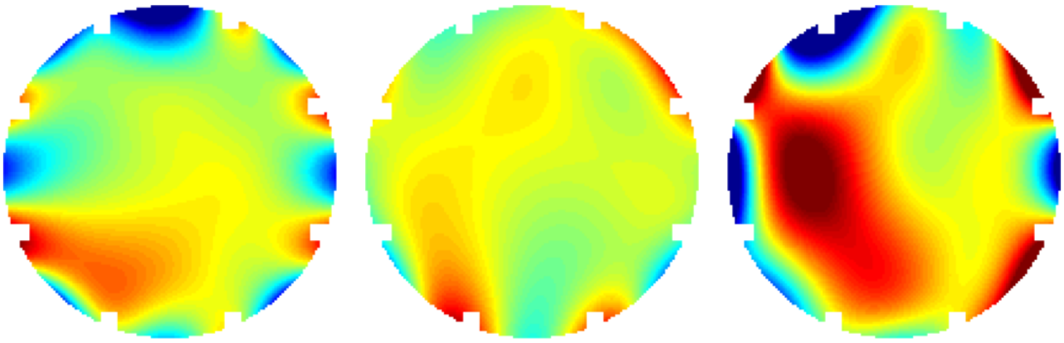

(a) Q^P_{11}/Q^H_{11} for Linerboard 2. (b) Q^P_{22}/Q^H_{22} for Linerboard 2. (c) Q^P_{12}/Q^H_{12} for Linerboard 2.

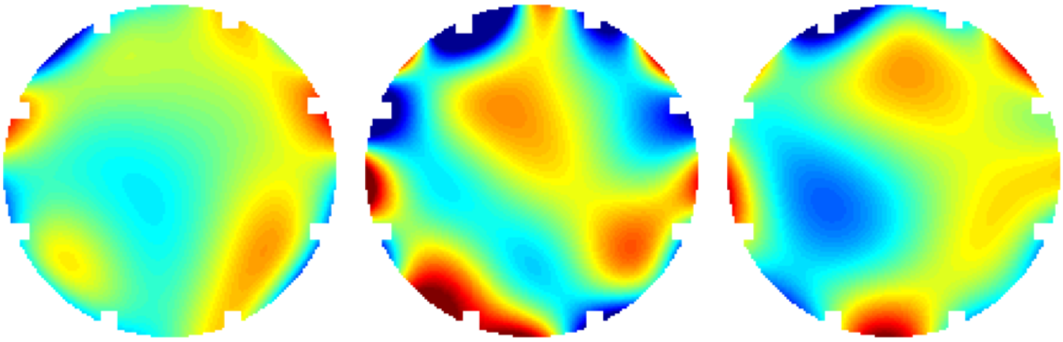

(d) Q^P_{66}/Q^H_{66} for Linerboard 2. (e) Q^P_{16}/Q^H_{16} for Linerboard 2. (f) Q^P_{26}/Q^H_{26} for Linerboard 2.

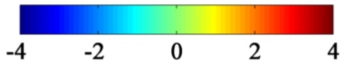

FIGURE 5.10: Fourth order polynomial Q^P_{11}/Q^H_{11} contour maps for Linerboard 2, mappings are normalized by the homogeneous 'Superposition' identification in Table 5.2.

the Superposition test. The EG results were normalized by squaring each EG point and those mappings are shown in the right column of Figure 5.15.

The left column of Figure 5.16 shows the EG mapping for each material using 5x5 data points for each EG element. Stiffnesses used to calculate local equilibrium came from the Superposition test. The EG results were normalized by squaring each EG point and those mapping are shown in the right column of Figure 5.16. These EG maps look very similar to those in Figures 4.24(g)-4.24(i) of Chapter 4. The matrix material for the simulated materials in Chapter 4 was set similar to have properties similar to Filter. The addition of artificial noise of magnitude was set to resolution of these DIC measurements which tended to obscure the border of the simulated inclusions. The smaller stiffness gradients in these materials were not discernible by EG mapping.

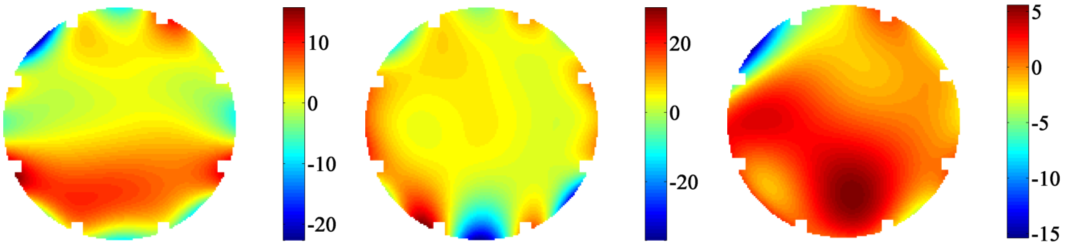

(a) Q_{11} for Linerboard 3. (b) Q_{22} for Linerboard 3. (c) Q_{12} for Linerboard 3.

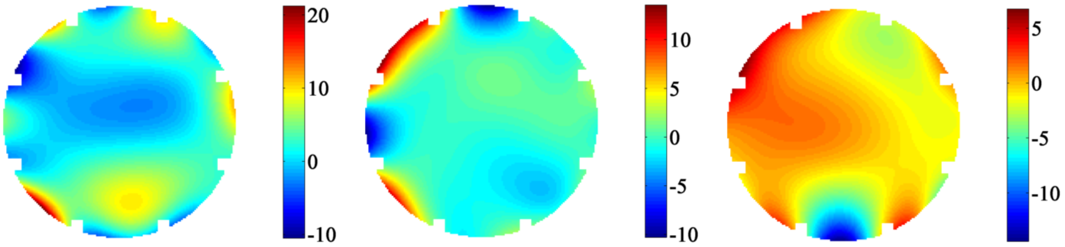

(d) Q_{66} Linerboard 3. (e) Q_{16} for Linerboard 3. (f) Q_{26} for Linerboard 3.

FIGURE 5.11: Fourth order polynomial Q_{ij} contour maps for Linerboard 3, units $\mathrm{km}^2/\mathrm{s}^2$.

5.8 Discussion

The objective is to develop a characterization of heterogeneity in paper materials by defining upper and lower bounds for Q_{ij}. Comparison of the range of these bounds between materials will provide means to objectively determine degree of heterogeneity.

It was initially hoped that the EG mapping would be sensitive enough to locate heterogeneous regions which could then be examined by sub-dividing from the remainder of the material. Clearly the EG mappings in Figures 5.15 and 5.16 were unable to separate those regions due to strain noise. Several different EG window sizes, EG smoothing parameters and number of VF elements were examined without improved resolution. In these materials, the 3x3 EG element was 5.4 mm square which made the EG window 10.8 x 10.8 mm square; the 5x5 EG element was 9.0 mm square giving a 18.0 x 18.0 mm square EG window.

However, for Linerboards 2 and 3 the grammage variation appears to occur such that the 3x3 EG window would have been able to determine heterogeneity if strain resolution were improved and heterogeneity was grammage-based. While the grayscale NIR images have not been contrast adjusted, camera aperture and light source have been set to maximize grayscale differences. Grammage variation is considered poor if it is more than ±10% and it is likely to be less in these materials.

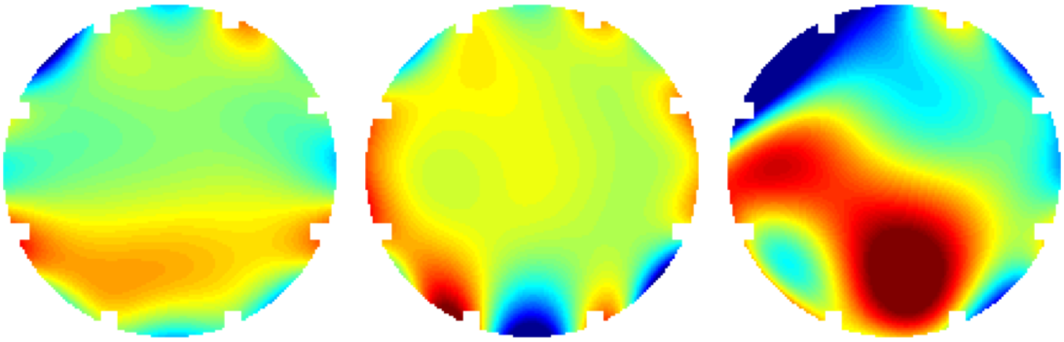

(a) Q^P_{11}/Q^H_{11} for Linerboard 3. (b) Q^P_{22}/Q^H_{22} for Linerboard 3. (c) Q^P_{12}/Q^H_{12} for Linerboard 3.

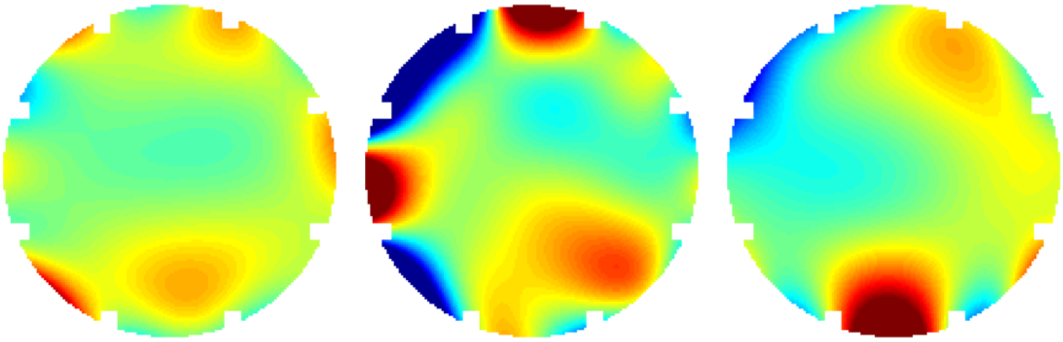

(d) Q^P_{66}/Q^H_{66} for Linerboard 3. (e) Q^P_{16}/Q^H_{16} for Linerboard 3. (f) Q^P_{26}/Q^H_{26} for Linerboard 3.

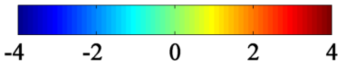

FIGURE 5.12: Fourth order polynomial Q^P_{11}/Q^H_{11} contour maps for Linerboard 3, mappings are normalized by the homogeneous 'Superposition' identification in Table 5.3.

Assumption of homogeneity furnishes a starting point for bounding of Q_{ij}; a minimal assumption would be that the stiffnesses identified presupposing the material to be homogeneous should be contained within the upper and lower bounds of the stiffness range. The first section of Tables 5.2-5.4 showed homogeneous stiffness identifications. Variation of parameter identification, as indicated by η_{ij}, is quite good and smaller than for similar tests on the same materials in Chapter 3; see Figures 3.9 and 3.10. The highest COV for identified stiffnesses Q_{11}, Q_{22}, Q_{12} and Q_{66} was 6.9%. Superposition of all the tests produced increased stiffnesses, with the only exception as Filter Q_{12} which decreased negligibly. Additionally, orthotropy of each material was examined by comparing the orthogonality of the material principal directions. Using the superposition Q_{ij} values the linerboards were orthotropic within 0.5° and Filter was orthotropic within 1.5°.

The bounds for Q_{ij} can be determined from grammage-based heterogeneity identification and polynomial formulation for Q_{ij}. In Chapter 4 the hard inclusions were best identified

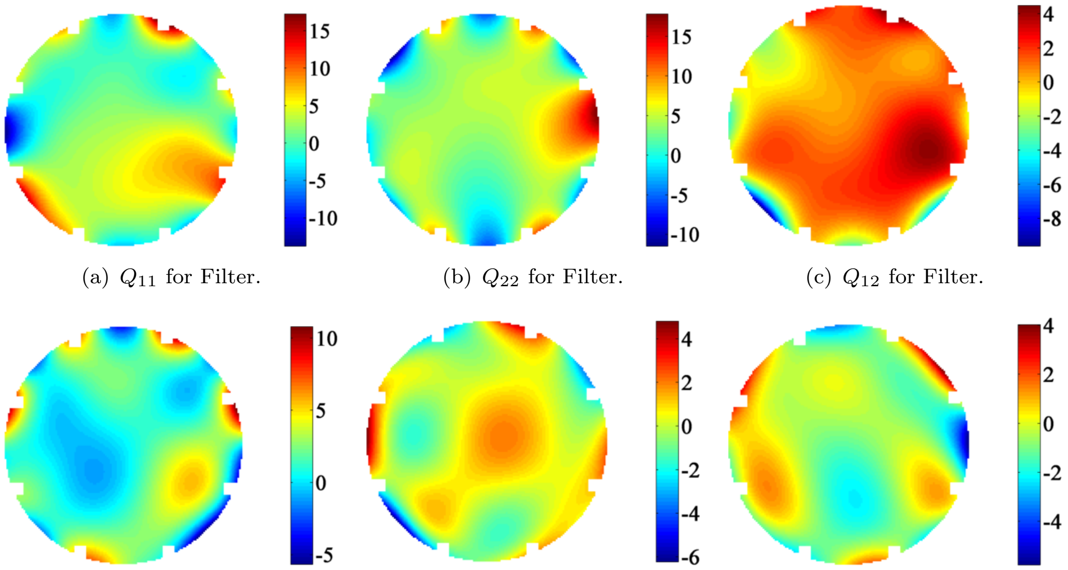

(a) Q_{11} for Filter. (b) Q_{22} for Filter. (c) Q_{12} for Filter.

(d) Q_{66} for Filter. (e) Q_{16} for Filter. (f) Q_{26} for Filter.

Figure 5.13: Fourth order polynomial Q_{ij} contour maps for Filter, units km^2/s^2.

when their location was known. Here, local grammage was used as a surrogate for knowledge of inclusion location and geometry, however a direct relationship between grammage and stiffness is not expected and was not found in these materials. None of the stiffness identification based on grammage variation trended with grammage, e.g. stiffnesses in the high grammage regions were not uniformly higher than those in the low grammage regions. Two other factors complicate this type of identification, namely fiber orientation likely varies in regions of similar grammage and residual stresses, created during restraint drying, do not generally align with either fiber orientation or the MD (machine direction) of the material. But, even with those concerns, grammage-based identification can provide some estimates for high stiffness regions.

Three different grammage-based identifications were performed for Linerboard 2 whose results are shown in Table 5.2. In the first division the high and low grammage regions were separated by the mean GV of Figure 5.4. Except for the value of Q_{66} in the high grammage region, 11.69 km^2/m^2, the remaining stiffnesses were justifiable. The high and low grammage division would correspond to a more stiff region and a softer region, respectively, except that orthotropy changes dramatically between regions. In the high grammage region Q_{22} is stiffer than Q_{11} and the converse is true in the low grammage region. While the aforementioned Q_{66} may be a concern, the other identified stiffnesses produced mean values in good agreement with those identified with the Superposition test.

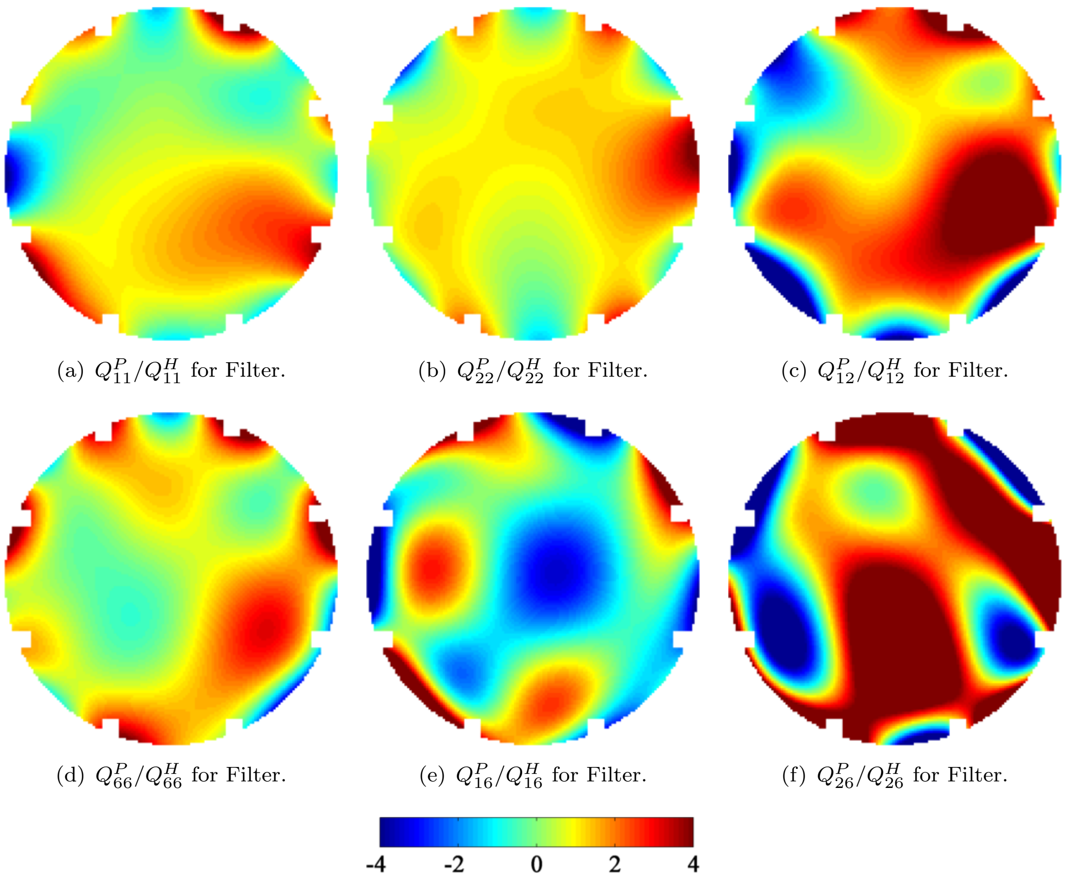

(a) Q^P_{11}/Q^H_{11} for Filter.

(b) Q^P_{22}/Q^H_{22} for Filter.

(c) Q^P_{12}/Q^H_{12} for Filter.

(d) Q^P_{66}/Q^H_{66} for Filter.

(e) Q^P_{16}/Q^H_{16} for Filter.

(f) Q^P_{26}/Q^H_{26} for Filter.

FIGURE 5.14: Fourth order polynomial Q^P_{11}/Q^H_{11} contour maps for Filter, , mappings are normalized by the homogeneous 'Superposition' identification in Table 5.4.

Comparison COV of the identification provides another tool tool to evaluate performance of the analysis method. Both the Superposition identification and the division into two equal-sized region based on grammage used the same number of tests, six for Linerboard 2. For all identifications, the η_{ij} were greater for the grammage-based divisions than for a single homogeneous division. Clearly, grammage-based divisions did not improve identification and, therefore, stiffness is not directly related to grammage. However, one other trend is that η_{ij}s were generally higher for lower grammage regions. This trend was expected because they depend on strain level and the lower grammage regions are likely to have higher strain; this trend is most evident in Linerboard 2 results.

The other two grammage divisions, one of three equal sized-regions and the other with a large medium grammage regions and equal, but smaller high and low grammage regions, gave results which tended to reinforce the results with two equal divisions of grammage. Mean and weighted mean, the latter weighted by area, gave identifications which were

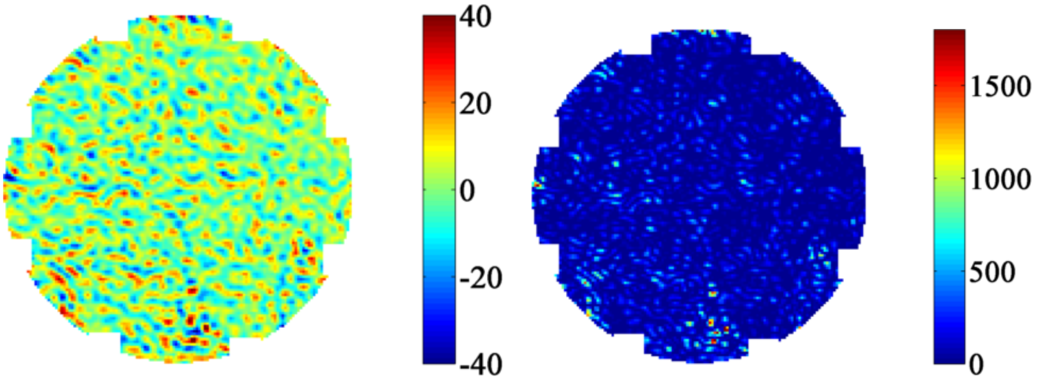

(a) EG: Linerboard 2. (b) EG: Linerboard 2, normalized.

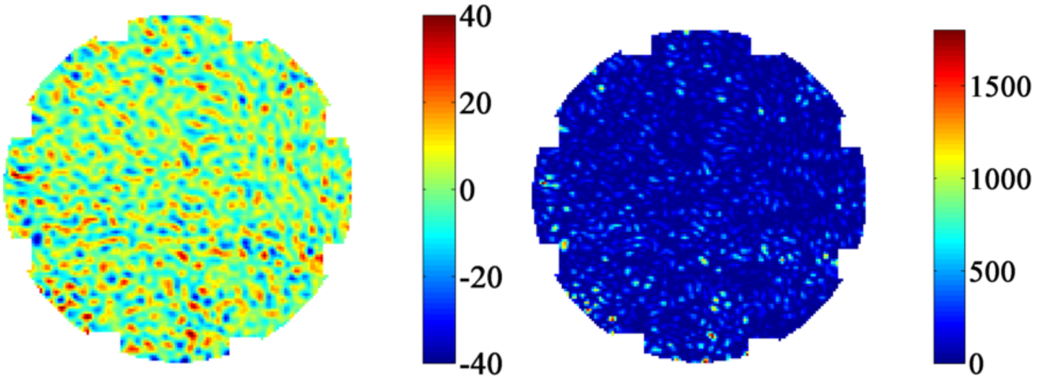

(c) EG: Linerboard 3. (d) EG: Linerboard 3, normalized.

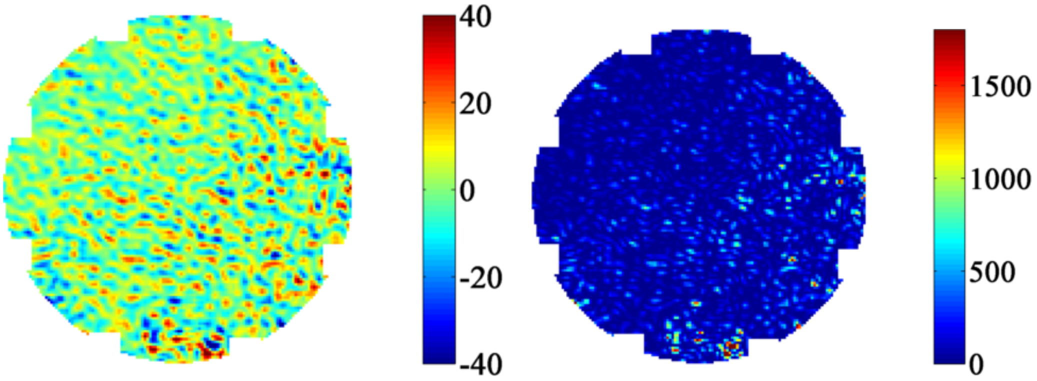

(e) EG: Filter. (f) EG: Filter, normalized.

FIGURE 5.15: EG contours for 3x3 window size.

similar to that of the Superposition test. These grammage divisions both identified auxetic, $Q_{12} < 0$, behavior in their respective high grammage regions. While such behavior is possible, and has been observed simulated random fiber composites [104], here it seems plausible that these values represent identification error. Values for $\nu_{12} < 0.10$ have been reported in paper materials [105].

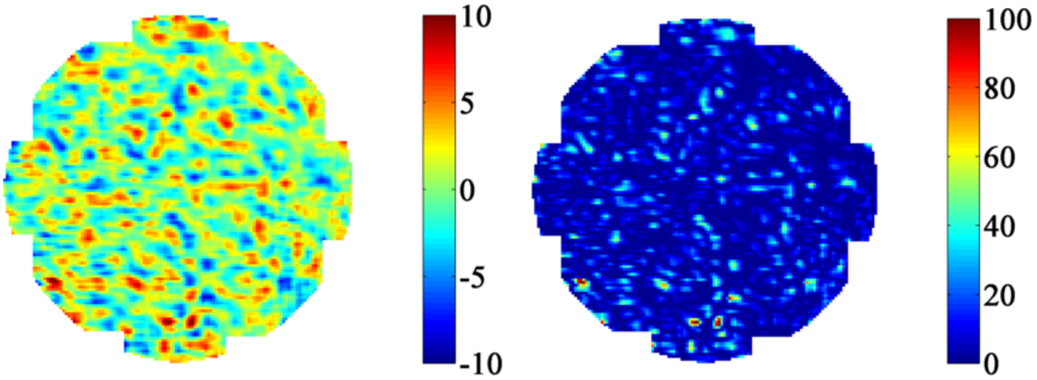

(a) EG: Linerboard 2. (b) EG: Linerboard 2, normalized.

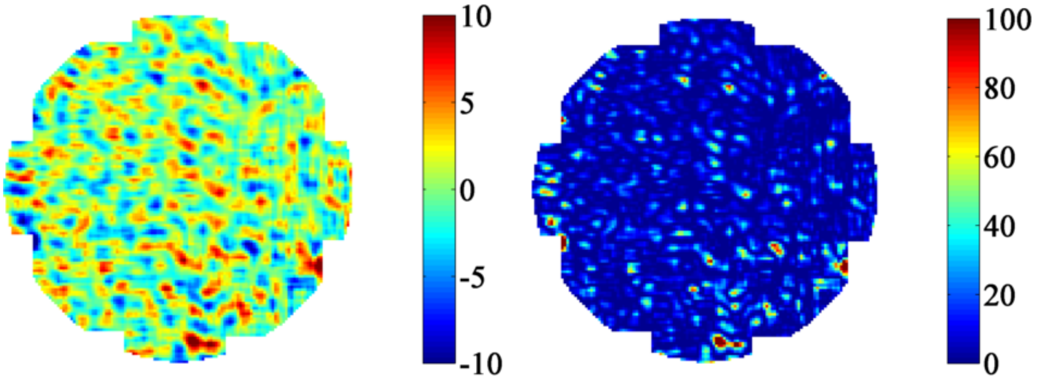

(c) EG: Linerboard 3. (d) EG: Linerboard 3, normalized.

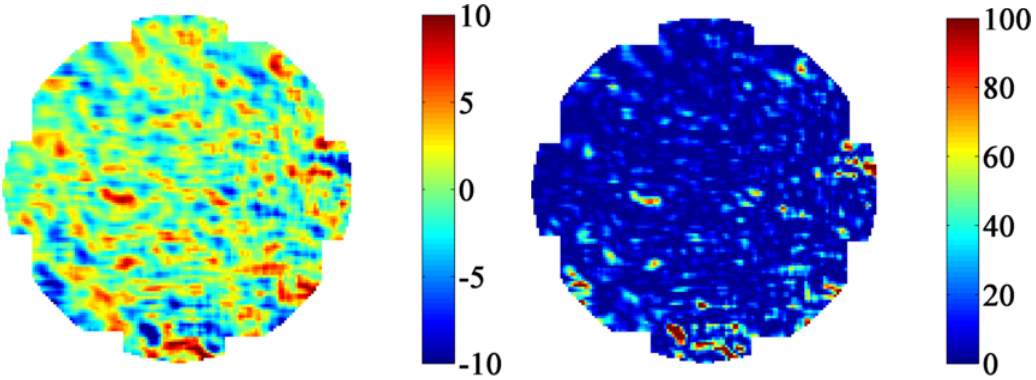

(e) EG: Filter. (f) EG: Filter, normalized.

Figure 5.16: EG contours for 5x5 window size.

The final section of Table 5.2 gives mean identifications from three different polynomial formulations for Q_{ij}. Three orders of polynomial were evaluated because the polynomial formulation tends to emphasize regions of low stiffness. If low stiffness regions are present then the high order polynomial will identify lower stiffnesses than a low order polynomial.

Only two types of grammage division were possible with Linerboard 3. As listed in the footnote in Table 5.3, the special, optimized virtual fields needed to identify each stiffnesses could not be found, after 100 iterations, for the case of three equal-sized grammage-based subdivisions. As with Linerboard 2, neither of each grammage divisions gave stiffness identification which corresponded with grammage. Due to heterogeneity, the stiffnesses identified here are a type of average across the specimen; auxetic behavior was identified for both high grammage regions, but, as stated for Linerboard 2, are indicative of identification error.

The mean 3$^{\text{rd}}$ order polynomial Q_{ij} formulation for Linerboard 3 identified auxetic behavior of greater magnitude than identified in the high grammage divisions; $Q_{12} = -0.53$ for the polynomial and -0.13, -0.46 for the high grammage divisions. It is still not possible to definitively state that auxetic behavior exists in Linerboard 3, but it seems more prudent to maintain these identifications are representative of identification error.

Only a single type of grammage division was possible for Filter, equal division into high grammage and low grammage regions. Except for Q_{66} the means of the Q_{ij} agree reasonably well with those determined by the Superposition identification. The polynomial formulation gave decreasing Q_{11}, Q_{22}, Q_{12}, Q_{66} with higher polynomial order. As the 'most' homogeneous of the three materials and the material which experienced the least drying restraint during manufacture, Filter also had the longest fibers and the smallest orthotropy ratio. These factors reduce the effect of changing local fiber orientation and residual stresses, allowing the polynomial formulation to better emphasize less stiff regions.

Before developing Q_{ij} bounds recall that the specimens were approximately oriented within the load fixture at 45° in order to have non-zero Q_{16} and Q_{26} and have improved identification for Q_{11}, which is difficult due to location of load cells and grips. Therefore, all identifications correspond to stiffnesses at that orientation. However, due to the nature of heterogeneity in these materials, local material principal directions are unknown. An upper bound for Q_{11} or Q_{22} is more likely to reflect local primary material principal direction when the specimen is oriented at 45° than for other orientations. If the specimen MD was vertically aligned then variation of local fiber orientation around the MD would be emphasized at the sacrifice of local fiber orientation about the CD. By orienting the specimen with the MD approximately aligned at 135°, local fiber orientation about the MD and CD have similar likelihood for identification.

Table 5.5: Upper and lower Q_{ij} bounds for each material, units (km^2/s^2)

		Q_{11}	Q_{22}	Q_{12}	Q_{66}	Q_{16}	Q_{26}
Linerboard 2	Upper	7.31	8.48	3.82	10.84	0.05	0.41
	Lower	1.58	2.44	-0.22	0.29	-2.79	-3.10
	Superposition η_{ij}/Q_{ij}	7	7	22	15	-31	-20
Linerboard 3	Upper	10.24	8.90	4.05	20.36	3.85	1.46
	Lower	1.39	3.95	-0.53	1.90	-4.55	-6.32
	Superposition η_{ij}/Q_{ij}	9	9	42	23	-49	-33
Filter	Upper	4.39	6.58	1.23	6.05	1.14	0.00
	Lower	1.96	1.90	0.26	0.29	-2.40	-0.82
	Superposition η_{ij}/Q_{ij}	6	6	28	11	-22	-49

Upper bounds were set at the highest values of identification for either a grammage-based heterogeneity or the 3rd or 4th order polynomial analyses. Similarly, lower bounds were set at the lowest values of identification for either a grammage-based heterogeneity or the 3rd or 4th order polynomial analyses. The 5th order polynomial analysis was not used for bound determination to reduce range of the bounds. However, if included it would have only changed the bounds for Linerboard 2 Q_{11}, Linerboard 3 Q_{66}, Filter Q_{11} and Q_{66}, 4 of the 18 bounds. While these bounds seem large they are similar to those found by Korteoja et al. [23] who measured modulus of over 4000 tensile specimens of a single paper material to determine low modulus values at 10% of mean stiffness and high modulus values at 300% of mean stiffness.

Earlier work used values for η_{ij}/Q_{ij} to determine the effect of strain noise on the identification. As seen in the **G** matrix, Equation 3.5, their magnitudes depend on measured strain; higher strain reduces the signal to noise ratio and improves (reduces) the η_{ij}/Q_{ij}s. Here, local strain variation caused by heterogeneity behaves as signal noise and tends to increase η_{ij}/Q_{ij}. Comparison between η_{ij}/Q_{ij} for each material depends on the relative applied strain for each test. The composite strains, given by Equation 3.8, for the Superposition test for Linerboard 2, Linerboard 3 and Filter were 6.5, 5.6, and 6.0 $\mu\varepsilon$, respectively. Because strain levels were similar between tests, the η_{ij}/Q_{ij} can be compared between tests.

The ranges given in Table 5.5 tend to agree with the η_{ij}/Q_{ij}. For example, comparing the ranges for Q_{11} Linerboard 3 has the largest range and η_{11}/Q_{11}; Filter has the smallest range and η_{11}/Q_{11}. The range-η_{ij}/Q_{ij} comparison always holds between Linerboard 2 and Linerboard 3 and between Linerboard 3 and Filter; it holds between Linerboard 2 and Filter for η_{11}/Q_{11}, η_{22}/Q_{22} and, η_{66}/Q_{66}.

Besides agreement between range and η_{ij}/Q_{ij}s, the ranges also tend to agree with the grammage heterogeneity observed in Figures 5.4-5.6. The grayscale image of Filter is dramatically smoother than those of the linerboards, which indicated less grammage-based heterogeneity. Differences between Linerboard 2 and 3 are best seen in their GV histograms where Linerboard 3 had a slightly extended right tail, indicating more low grammage regions than high grammage regions, and so it's range was expected to be larger.

For the Superposition test of each material, Q_{12} had the second largest η_{12}/Q_{12} which suggests some difficultly in identification. Both linerboards had lower bounds for Q_{12} which indicated auxetic behavior in some region of the specimens, but as stated earlier can likely be attributed to identification error. Developing a rationale to increase these values to zero, or higher, is reasonable, but further investigation would be helpful. Increased resolution of the full-field measurements would be a good first step to improving/refining upper and lower bounds.

In Chapter 3, the possibility of special orthotropy [74, 75] was examined for Linerboard 2 and Filter, but results were inconclusive. Interestingly, if each material is considered to be homogeneous and orthotropic (not special) and the Superposition Q_{ij} are rotated to maximize Q_{11}, both linerboards are auxetic with Linerboard 2 $Q_{12} = -0.14$ and Linerboard 3 $Q_{12} = -2.47$. More conclusive determination of special orthotropy is not possible here because specimen orientation at 45° causes one of the special orthotropy constants to equal zero.

5.9 Conclusion

A characterization of paper heterogeneity has been developed which agrees with visual observation and variation of stiffness when homogeneity is assumed and is similar to those found by other researchers. The characterization has two components which complement each other, upper and lower bounds for each Q_{ij} and coefficient of variation for each Q_{ij}. The characterization was used to compare three materials with different heterogeneity.

The characterization used tools developed in earlier chapters. In Chapter 3, validation of the load frame and homogeneous parameter identification was accomplished. A portion of the homogeneous identification, namely variation of stiffness, was used for this characterization. In Chapter 4, three different VFM analyses were developed to examine local stiffness. Two of those analyses, area-segmented identification and a polynomial formulation for Q_{ij}, were used here to define upper and lower stiffness bounds. The third VFM analysis in Chapter 4, the Equilibrium Gap analysis, was ineffective here because the strain measurement resolution was similar to strain variation created by heterogeneity. While discouraging, the result was anticipated because artificial strain noise in simulated materials tended to mask even dramatic ±30% stiffness variation.

This work represents the first reported effort, to the author's knowledge, in which heterogeneity in paper was stiffness-based, as opposed to grammage-based. Improvements in this heterogeneity characterization are possible; two of the most obvious are a higher resolution strain measurement and modification of the load frame to allow tests at multiple specimen orientations.

Chapter 6

Conclusion

This work has demonstrated that paper heterogeneity can be characterized by examination of strength loss and stiffness variability. Ultimate tensile strength, defined as tensile strength without variability, was related to actual tensile strength by application of two different strength criteria. Range of stiffnesses were determined through development of a new multiaxial load fixture and three different VFM analyses.

Tensile strength variation and formation have been the de facto standards for characterizing paper heterogeneity, even though multiple studies have showed little or no relation between the two measurements. A new approach was used here which estimated the amount of tensile strength improvement in the absence of variability. Because paper materials are often sold on a strength/weight basis, this new approach provides a tool for papermakers to use in cost/benefit analyses. Alterations to paper machinery are expensive, in up front costs and machine down time. This methodology creates a basic, easy-to-use relationship between variability and tensile strength.

The characterization of paper heterogeneity by defining upper and lower stiffness bounds is original. Mathematical stiffness bounds for special materials require well-defined inclusions which don't exist in paper. Instead, bounds were determined by direct measurement of local strains, application of an appropriate constitutive relationship and the requirement for equilibrium.

An underlying goal of paper physics research it to improve utilization of the cellulose fiber resource. Reduction of heterogeneity in paper creates opportunities to reduce the amount of fiber while improving performance. Some specific examples include extended currency durability, stronger, lighter packaging, improved print registration, and increased vapor barrier properties. New, specialized products can be developed to include cellulose fiber which require very small variability, such as flexible electronics and energy storage devices.

These analysis methods can be extended to other, stiffer materials. Determination of heterogeneity in those materials may require some novel fixture development, but the analysis tools remain applicable.

When I reflect to the beginning of this work, the anticipated results and the manner in which I thought paper materials behaved under stress, the results of this work surprised me in two ways. I expected the strength variation to be larger and the stiffness variation to be smaller. I anticipate these results will be surprising to many papermakers. These results encourage me and provide many opportunities for paper physics research as stiffness is a more critical property for many applications.

The primary contributions of this work are:

- A methodology to determine paper and paperboard maximum strength in absence of heterogeneity
- Extension of VFM for analysis of fully anisotropic Q_{ij}. A critical component of this extension was the determination of the noise optimization matrix, $\mathbf{G}$, given in Equation 3.5.
- Use of VFM for determination of anisotropic Q_{ij} on a thin web material, used here on paperboard. A novel load fixture was designed and fabricated to create heterogeneous strain fields while preventing wrinkling.
- Direct identification of local anisotropic Q_{ij} in simulated heterogeneous materials. The basic methodology comes from Section 5.2 of Pierron and Grédiac [1], and was extended here for anisotropic materials. The other portion of this contribution was the understanding of how different VFM formulations provide complimentary information on the nature of material heterogeneity.
- Specification of upper and lower stiffness bounds for paper. Analysis of full-field strains with heterogeneous stiffness VFM formulations provided identification of bounds. Mechanical property bounds are unique in paper physics work and provide information which directly affects converting and end-use behavior.

- A more comprehensive understanding of the capability of VFM for anisotropic material characterization. By examining the effects of resolution of full-field displacements and strains, ill-conditioned matrices when trying to determine, e.g., 200+ stiffness parameters, VFM mesh density, stiffness variability on anisotropic material characterization the avenues for future work are more apparent.

6.1 Recommendations for Future Work

Selection of a linear elastic constitutive behavior was important to validate stiffness identification. However, limit of that behavior was reached during some of the tests here. Extension to heterogeneity and nonlinear elastic behavior is possible within the VFM analysis.

The effect of fiber length on paper strength has been well-examined. Fiber length affects flocculation and fiber orientation. It seems reasonable that paper constitutive behavior would also contain a length component. Cosserat constitutive behavior has a length parameter which determines its ability to resist couple stresses. Cosserat behavior has been observed in other fibrous materials. Examination of possible Cosserat behavior would require some modification of VFM and DIC, or other full-field measurement technique.

Improved resolution for full-field displacement and strain measurements would provide more precise parameter identification. The goal would be to improve strain resolution sufficiently so that the equilibrium gap analysis could identify local stiffness changes. Another benefit would the ability to perform identification at reduce stress levels.

Monte-Carlo sampling could be used for heterogeneity characterization. A general inclusion shape, such as an ellipse, could be used in the identification by performing many simulations which uses different locations, sizes, ellipse-aspect ratios and, ellipse orientations, to determine inclusion stiffnesses. A compilation of those results could help identify regions of high or low stiffness.

New load fixtures could be simulated with FEM analyses to determine how to improve identification. Grip location relative to load application points, number of grips and load application points, and different sizes can be examined with the goal to improve heterogeneous stiffness identification.

Bibliography

[1] F. Pierron and M. Grédiac. *The Virtual Fields Method: Extracting Constitutive Mechanical Parameters from Full-Field Deformation Measurements*. Springer, 2012.

[2] J.M. Considine, D.W. Vahey, J.W. Evans, K.T. Turner, and R.E. Rowlands. Evaluation of strength-controlling defects in paper by stress concentration analyses. *J. Compos. Mater.*, 46(11):1323–1334, 2011.

[3] P.P.J. Miettinen, J.A. Ketoja, and T. Hjelt. Simulated structure of wet fiber networks. *Nord. Pulp Pap. Res. J.*, 22(4):516–522, 2007.

[4] M. Rigdahl, H. Andersson, B. Westerlind, and H. Hollmark. Elastic behaviour of low density paper described by network mechanics. *Fibre Sci. Technol.*, 19(2): 127–144, 1983.

[5] J. Astrom, S. Saarinen, K. Niskanen, and J. Kurkijarvi. Microscopic mechanics of fiber networks. *J. Appl. Phys.*, 75(5):2383–2392, 1994.

[6] R.J. Norman. Dependence of sheet properties on formation and forming variables. *Consolidation of the Paper Web, Transactions of the IIIrd Fundamental Research Symposium*, 1:269–309, 1965.

[7] J.M. Moffat, L.R. Beath, and W.G. Mihelich. Major factors governing newsprint strength. *The Fundamental Properties of Paper Related to Its Uses, Transactions of the Vth Fundamental Research Symposium*, 1:104–127, 1973.

[8] M.M. Nazhad, E.J. Harris, C.T.J. Dodson, and R.J. Kerekes. The influence of formation on tensile strength of papers made from mechanical pulps. *Tappi J.*, 83 (12):63–63, 2000.

[9] M.M. Nazhad, W. Karnchanapoo, and A. Palokangas. Some effects of fibre properties on formation and strength of paper. *Appita*, 56(1):61–65, 2003.

[10] U.-B. Mohlin. Fiber dimensions-formation and strength. *Nord. Pulp Pap. Res. J.*, 16(3):235–239, 2001.

[11] B. Nordström. Effects of grammage on sheet properties in one-sided and two-sided roll forming. *Nord. Pulp Pap. Res. J.*, 18(3):280–287, 2003.

[12] R. Wathén and K. Niskanen. Strength distributions of running webs. *J. Pulp Paper. Sci.*, 32(3):137–144, 2006.

[13] S.J. I'Anson and W.W. Sampson. Competing Weibull and stress-transfer influences on the specific tensile strength of a bonded fibrous network. *Compos. Sci. Technol.*, 67(7):1650–1658, 2007.

[14] S.V. Suknyov. Estimation of the tensile strength reduction of a composite laminate with a hole. *Mech. Compos. Mater.*, 36(6):439–444, 2000.

[15] M.J. Korteoja, A. Lukkarinen, K. Kaski, D.E. Gunderson, J.L. Dahlke, and K.J. Niskanen. Local strain fields in paper. *Tappi J.*, 79:217–224, 1996.

[16] M.J. Korteoja, A. Lukkarinen, K. Kaski, and K.J. Niskanen. Computational study of formation effects on paper strength. *J. Pulp Pap. Sci.*, 23(1):J18–J22, 1997.

[17] D. Choi, J.L. Thorpe, and R.B. Hanna. Image analysis to measure strain in wood and paper. *Wood Sci. Technol.*, 25(4):251–262, 1991.

[18] G.J. Um and R.W. Perkins. Stress and strain for perforated tensile specimens, Part 1: experimental measurements. *Tappi J.*, 6(3):3–7, 2007.

[19] L. Wong, M.T. Kortschot, and C.T.J. Dodson. Effect of formation on local strain fields and fracture of paper. *J. Pulp Paper. Sci.*, 22(6):J213–J219, 1996.

[20] J.M. Considine, C.T. Scott, R. Gleisner, and JY Zhu. Use of digital image correlation to study the local deformation field of paper and paperboard. *Advances in Paper Science and Technology, Transactions of the XIIIth Fundamental Research Symposium*, pages 613–630, 2005.

[21] D.T. Hristopulos and T. Uesaka. Structural disorder effects on the tensile strength distribution of heterogeneous brittle materials with emphasis on fiber networks. *Phys. Rev. B: Condens. Matter*, 70(6):064108, 2004.

[22] M. Ostoja-Starzewski and J. Castro. Random formation, inelastic response and scale effects in paper. *Philos. Trans. R. Soc. London, Ser. A*, 361(1806):965–985, 2003.

[23] M. Korteoja, L.I. Salminen, K.J. Niskanen, and M. Alava. Statistical variation of paper strength. *J. Pulp Pap. Sci.*, 24(1):1–7, 1998.

[24] J. Rhee, H.K. Cho, D.J. Marr, and R.E. Rowlands. On reducing stress concentrations in composites by controlling local structural stiffness. In *Proceedings of Conference Experimental and Applied Mechanics*, pages 193–199, 2005.

[25] R.W. Perkins and G.J. Um. Stress and strain for perforated tensile specimens, Part 2: FEA simulations. *Tappi J.*, 6(4):22–27, 2007.

[26] M.T. Kortschot and K. Trakas. Predicting the strength of paper containing holes or cracks with the point stress criterion. *Tappi J.*, 81(1):254–259, 1998.

[27] J. Awerbuch and M.S. Madhukar. Notched strength of composite laminates: predictions and experiments - A review. *J. Reinf. Plast. Compos.*, 4(1):3–159, 1985.

[28] J.M. Whitney and R.J. Nuismer. Stress fracture criteria for laminated composites containing stress concentrations. *J. Compos. Mater.*, 8(3):253–265, 1974.

[29] S.G. Lekhnitskii. *Theory of elasticity of an anisotropic elastic body.* San Francisco, CA: Holden-Day, 1963.

[30] W.H. Beyer and Chemical Rubber Compancy. *CRC standard mathematical tables.* CRC Press Inc., Boca Raton, FL, 1987.

[31] U.A. Khashaba. Fracture behavior of woven composites containing various cracks geometry. *J. Compos. Mater.*, 37(1):5–20, 2003.

[32] S.C. Tan. Finite-width correction factors for anisotropic plate containing a central opening. *J. Compos. Mater.*, 22(11):1080–1097, 1988.

[33] J.C. McNulty, F.W. Zok, G.M. Genin, and A.G. Evans. Notch-sensitivity of fiber-reinforced ceramic-matrix composites: Effects of inelastic straining and volume-dependent strength. *J. Am. Ceram. Soc.*, 82(5):1217–1228, 1999.

[34] B.C. Donner. An heuristic model of paper rupture. *Fundamentals of Papermaking Materials, Transactions of the XIth Fundamental Research Symposium*, pages 1215–1247, 1997.

[35] J. Considine, D. Vahey, W. Skye, W. Chen, K. Turner, and R. Rowlands. Shielding: new insight to the relationship between formation and strength, 2005. Poster presented PaperCon '09 TAPPI/PIMA paper conference and trade show, May 31 - June 3, 2009, St Louis, MO, USA.

[36] G.W. Snedecor and W.G. Cochran. Statistical methods. 1980.

[37] I. Diddens, B. Murphy, M. Krisch, and M . Müller. Anisotropic elastic properties of cellulose measured using inelastic X-ray scattering. *Macromolecules*, 41(24): 9755–9759, 2008.

[38] G.A. Baum. Elastic properties, paper quality, and process control. *Appita*, 40(4): 289–294, 1987.

[39] R. Allan. The cost of paper property variation is high. *Appita*, 65(4):308–312, 2012.

[40] K. Schulgasser. Fibre orientation in machine-made paper. *J. Mater. Sci.*, 20(3): 859–866, 1985.

[41] M. Htun, H. Andersson, and M. Rigdahl. The influence of drying strategies on the anisotropy of paper in terms of network mechanics. *Fibre Sci. Tech.*, 20(3): 165–175, 1984.

[42] G.L. Batten and A.H. Nissan. Invariants in paper physics. *Tappi J.*, 69(10): 130–131, 1986.

[43] M. Titus. Ultrasonic technology - measurements of paper orientation and elastic properties. *Tappi J.*, 77(1):127–130, 1994.

[44] M.W. Johnson Jr and T.J. Urbanik. Buckling of axially loaded, long rectangular paperboard plates. *Wood Fiber Sci.*, 19(2):135–146, 1987.

[45] T.D. Gerhardt. External pressure loading of spiral paper tubes: theory and experiment. *J. Eng. Mater. Technol.*, 112(2):144–150, 1990.

[46] T. Garbowski, G. Maier, and G. Novati. On calibration of orthotropic elastic-plastic constitutive models for paper foils by biaxial tests and inverse analyses. *Struct. Multidiscip. Optim.*, pages 1–18, 2012.

[47] M.V. Anurov, S.M. Titkova, and A.P. Oettinger. Biomechanical compatibility of surgical mesh and fascia being reinforced: dependence of experimental hernia defect repair results on anisotropic surgical mesh positioning. *Hernia*, 16(2):199–210, 2012.

[48] S.I. Ranganathan, M. Ostoja-Starzewski, and M. Ferrari. Quantifying the anisotropy in biological materials. *J. Appl. Mech.*, 78(6):64501, 2011.

[49] A.K. Sengupta, D. De, and B.P. Sarkar. Anisotropy in some mechanical properties of woven fabrics. *Text. Res. J.*, 42(5):268–271, 1972.

[50] T. Guélon, E. Toussaint, J.-B. Le Cam, N. Promma, and M. Grédiac. A new characterisation method for rubber. *Polym. Test.*, 28(7):715–723, 2009.

[51] I.M. Daniel and J.-M. Cho. Characterization of anisotropic polymeric foam under static and dynamic loading. *Exp. Mech.*, 51(8):1395–1403, 2011.

[52] J. Molimard, R. Le Riche, A. Vautrin, and J.R. Lee. Identification of the four orthotropic plate stiffnesses using a single open-hole tensile test. *Exp. Mech.*, 45 (5):404–411, 2005.

[53] J.P. Boehler, S. Demmerle, and S. Koss. A new direct biaxial testing machine for anisotropic materials. *Exp. Mech.*, 34(1):1–9, 1994.

[54] R.L. Edwards, G. Coles, and W.N. Sharpe. Comparison of tensile and bulge tests for thin-film silicon nitride. *Exp. Mech.*, 44(1):49–54, 2004.

[55] V.C. Setterholm, R. Benson, and E.W. Kuenzi. Method for measuring edgewise shear properties of paper. *Tappi J.*, 51(5):196, 1968.

[56] M.A. Sutton, J.-J. Orteu, and H. Schreier. *Image correlation for shape, motion and deformation measurements: basic concepts, theory and applications*. Springer, 2009.

[57] M.B. Lyne and R. Hazell. Formation testing as a means of monitoring strength uniformity. *The Fundamental Properties of Paper Related to its Uses, Transactions of the Vth Fundamental Research Symposium, Cambridge, UK*, pages 74–100, 1973.

[58] L. Bruno, F.M. Furgiuele, L. Pagnotta, and A. Poggialini. A full-field approach for the elastic characterization of anisotropic materials. *Opt. Lasers Eng.*, 37(4): 417–431, 2002.

[59] M. Grédiac, F. Pierron, and Y. Surrel. Novel procedure for complete in-plane composite characterization using a single T-shaped specimen. *Exp. Mech.*, 39(2): 142–149, 1999.

[60] E.R. Saberski, S.B. Orenstein, and Y.W. Novitsky. Anisotropic evaluation of synthetic surgical meshes. *Hernia*, 15(1):47–52, 2011.

[61] R. Chaves de Oliveira, R.E. Mark, and R.W. Perkins. Evaluation of the effects of heterogeneous structure on strain distribution in low density papers. In R.W. Perkins, editor, *Mechanics of Wood and Paper Materials, AMD Vol. 112, MD Vol. 23*, pages 37–61. ASME, 1990.

[62] L. Le Magorou, F. Bos, and F. Rouger. Identification of constitutive laws for wood-based panels by means of an inverse method. *Compos. Sci. Technol.*, 62(4): 591–596, 2002.

[63] D. Lecompte, A. Smits, H. Sol, J. Vantomme, and D. Van Hemelrijck. Mixed numerical–experimental technique for orthotropic parameter identification using biaxial tensile tests on cruciform specimens. *Int. J. Solids Struct.*, 44(5):1643–1656, 2007.

[64] T. Furukawa and J.W. Pan. Stochastic identification of elastic constants for anisotropic materials. *Int. J. Numer. Meth. Eng.*, 81(4):429–452, 2010.

[65] D. Claire, F. Hild, and S. Roux. A finite element formulation to identify damage fields: the equilibrium gap method. *Int. J. Numer. Meth. Eng.*, 61(2):189–208, 2004.

[66] A. Bonnin, R. Huchon, and M. Deschamps. Ultrasonic waves propagation in absorbing thin plates: Application to paper characterization. *Ultrasonics*, 37(8): 555–563, 2000.

[67] C.C. Habeger. An ultrasonic technique for testing the orthotropic symmetry of polymeric sheets by measuring their elastic shear coupling-coefficients. *J. Eng. Mater. Technol.*, 112(3):366–371, 1990.

[68] D. Chamberlain. Industry statistics 2011. *Paper Tech.*, 53(6):20–22, 2012.

[69] S. Avril, M. Grédiac, and F. Pierron. Sensitivity of the virtual fields method to noisy data. *Comput. Mech.*, 34(6):439–452, 2004.

[70] M.J.P. Musgrave. On the propagation of elastic waves in aeolotropic media. i. general principles. *Proc. R. Soc. London, Ser. A*, 226(1166):339–355, 1954.

[71] M.J.P. Musgrave. On the propagation of elastic waves in aeolotropic media. ii. media of hexagonal symmetry. *Proc. R. Soc. London, Ser. A*, 226(1166):356–366, 1954.

[72] R.M. Jones. *Mechanics of Composite Materials.* Taylor & Francis London, 1975.

[73] T.C.T. Ting. Anisotropic elastic constants that are structurally invariant. *Q. J. Mech. Appl. Math.*, 53(4):511–523, 2000.

[74] M. Ostoja-Starzewski and D. C. Stahl. Random fiber networks and special elastic orthotropy of paper. *J. Elast.*, 60(2):131–149, 2000.

[75] P. Vannucci. On special orthotropy of paper. *J. Elast.*, 99(1):75–83, 2010.

[76] F. Pierron, G. Vert, R. Burguete, S. Avril, R. Rotinat, and M.R. Wisnom. Identification of the orthotropic elastic stiffnesses of composites with the virtual fields method: sensitivity study and experimental validation. *Strain*, 43(3):250–259, 2007.

[77] M. Rossi and F. Pierron. On the use of simulated experiments in designing tests for material characterization from full-field measurements. *Int. J. Solids Struct.*, 49(3-4):420–435, 2012.

[78] C. Devivier, F. Pierron, and M.R. Wisnom. Impact damage detection in composite plates using deflectometry and the virtual fields method. *Composites Part A*, 48: 201–218, 2013.

[79] J.A. Bristow and P. Kolseth. *Paper Structure and Properties.* Marcel Dekker, 1986.

[80] M. Deng and C.T.J. Dodson. *Paper: An engineered stochastic structure.* Tappi Press, 1994.

[81] A.-L. Erikkilä, P. Pakarinen, and M. Odell. Sheet forming studies using layered orientation analysis: Can lead to a better understanding of the drainage process. *Pulp & Paper Canada*, 99(1):81–85, 1998.

[82] T. Enomae, Y.-H. Han, and A. Isogai. Nondestructive determination of fiber orientation distribution of paper surface by image analysis. *Nord. Pulp Pap. Res. J.*, 21(2):253–259, 2006.

[83] P. Ladeveze and D. Leguillon. Error estimate procedure in the finite element method and applications. *SIAM J Num Anal*, 20(3):485–509, 1983.

[84] S. Nemat-Nasser and M. Hori. *Micromechanics: overall properties of heterogeneous materials.* Elsevier, 2$^{\text{nd}}$ edition, 1999.

[85] A. Reuss. Berechnung der fließgrenze von mischkristallen auf grund der plastizitätsbedingung für einkristalle. *J. Appl. Math. Mech.*, 9(1):49–58, 1929.

[86] W. Voigt. Über die beziehung zwischen den beiden elasticitätsconstanten isotroper körper. *Ann. Phys.*, 274(12):573–587, 1889.

[87] X. Zhao, R. Duddu, S.P.A. Bordas, and J. Qu. Effects of elastic strain energy and interfacial stress on the equilibrium morphology of misfit particles in heterogeneous solids. *J. Mech. Phys. Solids*, 61(6):1433–1445, 2013.

[88] R. Dingreville, J. Qu, and M. Cherkaoui. Surface free energy and its effect on the elastic behavior of nano-sized particles, wires and films. *J. Mech. Phys. Solids*, 53 (8):1827–1854, 2005.

[89] D.R. Axelrad, K. Rezai, and D. Atack. Probabilistic mechanics of fibrous structures. *J. Appl. Math. Phys. (ZAMP)*, 35(4):497–513, 1984.

[90] A. Hanada and F. Onabe. Analysis of physical properties of paper by interference holography (I) construction of measuring system for local strain distribution of paper sheets. *Japan Tappi J.*, 47(5):645–652, 1993.

[91] A. Hanada and F. Onabe. Analysis of physical properties of paper by interference holography (II) visualization of local strain distribution of paper sheets through tensile testing process. *Japan Tappi J.*, 47(6):761–766, 1993.

[92] M.J. Korteoja, K.J. Niskanen, M.T. Kortschot, and K.K. Kaski. Progressive damage in paper. *Paperi ja puu*, 80(5):364–372, 1998.

[93] T. Yamauchi and K. Murakami. Structural changes of paper under tensile deformation. *Japan Tappi J.*, 47(9):1131–1135, 1993.

[94] T. Yamauchi and K. Murakami. Observation of deforming and fracturing processes of paper by use of thermography. *Products of Papermaking, Transactions of the Xth Fundamental Research Symposium, Oxford, UK*, 10:825–847, 1993.

[95] M.H. Odell and P. Pakarinen. The complete fibre orientation control and effects on diverse paper properties. TAPPI Papermakers Conference, pages 317–341. TAPPI Press.

[96] S. Osaki. Microwaves quickly determine the fiber orientation of paper. *Tappi J.*, 70(2):105–108, 1987.

[97] T. Leppänen. *Effect of fiber orientation on cockling of paper.* University of Kuopio, 2007.

[98] S.J. I'Anson, W.W. Sampson, and S. Savani. Density dependent influence of grammage on tensile properties of handsheets. *J. Pulp Pap. Sci.*, 34(3):182–189, 2008.

[99] T. Enomae and S. Kuga. Methodology to use flatbed image scanner for formation analysis of paper. *Japan Tappi J.*, 56(4):97–104, 2002.

[100] J.P. Bernie and W.J.M. Douglas. Local grammage distribution and formation of paper by light transmission image analysis. *Tappi J.*, 79(1):193–202, 1996.

[101] D.S. Keller, J.J. Pawlak, M. Kellomaki, J.E. Haglund, and N. Johansson. Three storage phosphor systems for beta-radiographic imaging of paper. *Nord. Pulp Pap. Res. J.*, 19(2):170–175, 2004.

[102] S. Rolland du Roscoat, M. Decain, X. Thibault, C. Geindreau, and J.-F. Bloch. Estimation of microstructural properties from synchrotron x-ray microtomography and determination of the rev in paper materials. *Acta Mater.*, 55(8):2841–2850, 2007.

[103] U.P. Agarwal and N. Kawai. Self-absorption phenomenon in near-infrared Fourier transform Raman spectroscopy of cellulosic and lignocellulosic materials. *Appl. Spectrosc.*, 24:385–388, 2005.

[104] E.J. Horrigan, C.W. Smith, F.L. Scarpa, N. Gaspar, A.A. Javadi, M.A. Berger, and K.E. Evans. Simulated optimisation of disordered structures with negative Poisson's ratios. *Mech. Mater.*, 41(8):919–927, 2009.

[105] G.A. Baum, D.C. Brennan, and C.C. Habeger. Orthotropic elastic constants of paper. *Tappi J.*, 64(8):97–101, 1981.